School of Molecular and Life Sciences

Developing Multimodal Spectroscopic Imaging Techniques to Study Metal Dyshomeostasis and Altered Brain Biochemistry During Ageing

Ashley Louise Hollings
0000-0001-7829-4932

This thesis is presented for the Degree of
Doctor of Philosophy
of
Curtin University

July 2022

Declaration

To the best of my knowledge and belief this thesis contains no material previously published by any other person except where due acknowledgement has been made.

This thesis contains no material which has been accepted for the award of any other degree or diploma in any university.

Animal Ethics

The animal tissue used in this thesis was excess tissue from previous studies that received animal ethics approval from the Curtin University Animal Ethics Committee, Approval Number AEC_2014_27. This research was conducted in compliance with the National Health and Medical Research Council Australian code for the care and use of animals for scientific purposes 8th edition (2013).

Signature:

Date: 28/06/2022

Abstract

Mild cognitive decline and memory loss are processes associated with natural ageing, however, ageing can also increase the risk of more serious cognitive loss, such as neurodegenerative diseases including Alzheimer's Disease. Alzheimer's disease is the most common form of dementia, and with ageing as the biggest risk factor for onset, it poses significant health and economic concerns for the ageing population. Despite extensive research into the key pathological markers of the disease and potential pathways of onset, currently there is no cure. While a common focus for understanding disease mechanisms is to study models of disease, further investigating biochemical changes that occur during natural ageing could be vital for elucidating the switch between natural ageing and disease, and in turn highlight potential avenues for prevention and risk minimisation.

Transition metal ions such as copper, iron, and zinc have gained attention as targets for investigation during brain ageing, given their importance to healthy brain and memory function. Further, altered brain metal homeostasis is observed during ageing and neurodegenerative disease. While it is widely accepted that these metals are altered during ageing and likely play a role in disease onset (as either a cause or consequence), the exact chemical pathways through which they influence memory function during health, natural ageing, or neurodegenerative disease are yet to be elucidated. The gap in the literature may in part be due to the difficulty to simultaneously image, and therefore, study the different chemical forms of metals within the brain (or biological samples in general).

The main aim of this thesis was to develop and apply spectroscopic imaging methods to study metal dyshomeostasis and altered brain biochemistry during ageing using the senescence accelerated mouse (SAM) model. The key outcomes of this thesis have been the development of a zinc X-ray absorption near edge structure spectroscopic imaging protocol to study zinc speciation in brain tissue sections with an emphasis on the importance of careful sample preparation considerations. Additionally, spectroscopic methods were applied to investigate the potential impact of age-related copper accumulation in the subventricular zone, surprisingly revealing that the redox active metal was not likely causing an elevation in markers of oxidative stress. Finally, a multi-modal protocol coupling spectroscopic imaging techniques such as Raman microscopy and X-ray fluorescence microscopy with immunohistochemistry on the same tissue section was developed, demonstrating the

possibility of attributing metal or biochemical alterations detected using spectroscopy, to specific cell types or subcellular locations as indicated by subsequent immunohistochemistry. Overall, the development of suitable methods to study brain biochemistry during ageing, and the application of these methods to understand the consequences of specific biochemical alterations, may help to reveal pathways or mechanisms of disease onset, in turn providing potential targets for therapeutic or preventative intervention.

Publications

I, **Ashley Hollings**, contributed conceptualisation, investigation, methodology, visualisation, writing-original draft, writing-review & editing to the following paper:

Revealing differences in the chemical form of zinc in brain tissue using K-edge X-ray absorption near-edge structure spectroscopy. Metallomics, **2020**, *12*, 2134-2144.

Ashley L. Hollings, Virginie Lam, Ryu Takechi, John C. L. Mamo, Juliane Reinhardt, Martin D. de Jonge, Peter Kappen, Mark J. Hackett

I as a Co-Author, endorse that this level of contribution by the candidate indicated above is appropriate.

Ashley L. Hollings	
Virginie Lam	
Ryu Takechi	
John C. L. Mamo	
Martin D. de Jonge	
Mark J. Hackett	
Juliane Reinhardt	Minor author. Did not reply.
Peter Kappen	Minor author. Did not reply.

Contribution of Others

Dr Mark Hackett, Dr Thomas Becker, Dr Jitraporn Vongsvivut, and Professor John Mamo assisted with the editing of this thesis.

Dr Mark Tobin, Dr Jitraporn Vongsvivut, Dr Annaleise Klein, Dr Valerie Mitchell, Dr Peter Kappen, and Dr Daryl Howard assisted with training on the synchrotron beamlines that were used to collect data for this thesis.

Dr Mark Hackett and Peter Chapman assisted with training on benchtop IR and Raman instruments, Dr Thomas Becker assisted with confocal Raman microscopy training, Michael Nesbit assisted with confocal and fluorescence microscopy training, and Dr Gae Ellison assisted with immunohistochemistry training.

Presentations

Some of the work presented in this thesis has been presented in various formats that are outlined below.

- RACI Twitter Conference (2019, 2020)
- Symposium for WA Neuroscience
    - 3 minute thesis presentation (2018)
    - Oral presentation (2020)
- Australian Synchrotron User Meeting
    - Poster slam and poster presentation (2018)
        - 3rd place poster slam
    - Oral presentation (2018, 2020)
- Australian Society for Molecular Imaging Conference
    - Oral presentation (2018)
        - 2nd place presentation
    - -Poster presentation (2021)
        - Poster award
- Australian X-Ray Analytical Association WA Student Seminars
    - Oral presentation (2019)
        - 3rd place presentation
- RACI Analytical and Environmental Chemistry Division Conference
    - Oral presentation (2019)
- Curtin University Molecular and Life Sciences HDR Symposium
    - Oral presentation (2019, 2020, 2021)
    - Poster presentation (2019, 2020, 2021)
        - Poster award (2019, 2021)
- Curtin University Three Minute Thesis Competition
    - 3 minute thesis presentation video (2020)
        - 2nd place video
- X-Ray Absorption Fine Structure Virtual 2021
    - Oral presentation video
- eBiological Inorganic Chemistry
    - 3 minute presentation video (2021)
- ANSTO Seminar Series
    - AINSE PGRA student presentation (2021)
- ANSTO User meeting
    - Oral presentation (2021)

Acknowledgements

Funding and Facilities

I would first like to acknowledge the support provided by an Australian government research training program (RTP) scholarship, and an Australian Institute of Nuclear Science and Engineering Post Graduate Research Award (AINSE-PGRA). Additionally, I would like to gratefully acknowledge the institutions and organisations that helped to make this research possible through funding and/or the use of state-of-the-art facilities. Specifically, I would like to thank Dementia Australia and the Australian Research Council (ARC) for funding, in addition to Curtin University (School of Molecular and Life Science), the Curtin Health and Innovation Research Institute (CHIRI), and the Australian Nuclear Science and Technology Organisation (ANSTO) for access to laboratory facilities (Curtin and CHIRI) and the Australian Synchrotron (ANSTO).

Personal

I'm so incredibly grateful to a number of people for their assistance and support to help me complete this PhD. Firstly, I would like to say a huge thank you to Mark for answering my endless emails, and for all of the guidance, advice, and support that you've provided over the last 5 years. I've felt extremely lucky to have such a helpful and supportive supervisor and could not have done this without your help. I'd also like to say a big thank you to my co-supervisors Tom, John, and Pimm for their continued support, with an extra thank you to Tom for your help with the Raman analysis, and to Pimm for always ensuring we enjoy our synchrotron trips with donuts and dancing. To the many beamline scientists who have helped to make data collection possible including Pimm, Mark and Annaliese at IRM, Daryl at XFM, and Peter and Valerie at XAS-thank you so much! To John, Ryu, Virginie and their research groups at CHIRI, thank you for all your assistance in the lab, and thank you to Michael for all your help with the microscopes and immunos. I'd also like to say a big thank you to Ching for helping me source chemicals I needed for experiments, and to Chappy for always being happy to have a chat and for all your help with the instruments! I'm also incredibly grateful to all of the chemistry staff and academics for helping to provide such a pleasant and supportive working environment.

To the ABACUSS team-thank you for all the fun we had on our sleep deprived synchrotron trips, from drawing pigs to eating hungry jacks at almost midnight! Special thanks to David for

managing the XAS sample changes that I was too short for, and to Gae for helping me with immunos and almost anything based at CHIRI!

To Rhiannon and Karina who I could not have made it through the last few years without-you guys are amazing! Thank you for being so supportive and making the experience so enjoyable. I'm so grateful for the dances, brunches, lunches, and of course, for you guys putting up with me even when I get a little hangry at the synchrotron.

A big thank you to the black belts at karate for brightening my Saturday mornings and supporting me when I sometimes worked on the thesis at the dojo, and of course to the Baldivis Districts Divas for always putting a smile on my face and giving me something to look forward to during long days of writing.

To my wonderful family and friends who support me in everything I do, thank you for once again cheering me on. For listening to my presentations and on occasion reading my work even if you don't quite understand the content. Special thanks to Dad, Kerry, and Eric for being so supportive and encouraging.

To Mum and Stace, thank you guys for everything. I couldn't have done this without you and am so grateful for your unwavering support in all that I do.

And finally, a massive thank you to Ryan who has encouraged and supported me every step of the way. From giving hugs when I'm stressed to bringing me food while I work, and even proof-reading my work. I'm so grateful for you.

Table of Contents

List of Figures

List of Tables

List of Abbreviations

AAS	Atomic Absorption Spectroscopy
AD	Alzheimer's Disease
ATR	Attenuated Total Reflectance
BBB	Blood Brain Barrier
CSF	Cerebrospinal Fluid
DAPI	4',6-diamidino-2-phenylindole
DMT1	Divalent Metal Transporter 1
FTIR	Fourier Transform Infrared
GC	Gas Chromatography
GFAP	Glial Fibral Acidic Protein
GSH	Glutathione
GSSG	Disulfide
HOMO	Highest Occupied Molecular Orbital
HPLC	High Performance Liquid Chromatography
IAUC	Integrated Area Under the Curve
IR	Infrared
IRM	Infrared Microscopy
LA-ICP-MS	Laser Ablation-Inductively Coupled Plasma-Mass Spectrometry
LUMO	Lowest Unoccupied Molecular Orbital
MAP2	Microtubule-Associated Protein 2
MS	Mass Spectrometry
PBS	Phosphate Buffered Saline
SAM(P)	Senescence Accelerated Mouse (Prone)
SAM(R)	Senescence Accelerated Mouse (Resistant)
SEM	Scanning Electron Microscopy
SIMS	Secondary Ion Mass Spectrometry
SOD	Superoxide Dismutase
SVZ	Subventricular Zone

XANES	X-ray Absorption Near Edge Structure
XAS	X-ray Absorption Spectroscopy
XFM	X-ray Fluorescence Microscopy
XRF	X-ray Fluorescence
ZnTs	Zinc transporter proteins

Chapter 1: Introduction

ABSTRACT

This chapter will discuss brain ageing and its association with the development of neurodegenerative diseases such as Alzheimer's disease. Additionally, the proposed role that metal ions play in brain ageing and disease will be summarised and the biochemical importance of ions such as copper and zinc will be addressed. Specifically, their role in several neurochemical pathways as cofactors or structural components of vital enzymes and proteins will be outlined along with the traditional methods used to study them. Although these traditional methods are extremely valuable, they have limitations, many of which can be overcome by using X-ray techniques. The theory behind X-ray absorption spectroscopy and X-ray fluorescence microscopy will be discussed, and examples of their previous applications to biological samples provided. Additional techniques such as vibrational spectroscopy and immunohistochemistry that can provide insights into other biochemical features will also be outlined with a specific focus on coupling these methods with X-ray spectroscopy. Furthermore, a brief background on the senescence accelerated mouse (SAM) model of ageing, which was used in this thesis, will be provided. Finally, the key aims of this thesis will be discussed as briefly outlined below.

Aim 1) Develop spectroscopic methods to image Zn speciation in brain tissue.

Aim 2) Apply spectroscopic techniques to probe markers of oxidative stress in Cu enriched regions of the lateral ventricles (SVZ).

Aim 3) Develop a protocol for coupling spectroscopic techniques with immunohistochemistry on the same tissue section.

1.1 Research Motivation – Developing New Tools to Study Brain Chemistry, to Help Fight Dementia

Mild cognitive impairment is associated with natural ageing, however, the ageing brain is also at greater risk of developing neurodegenerative diseases, such as Alzheimer's Disease (AD). AD makes up 60-70% of all dementia cases [1] and has significant social, economic and health impacts. In addition to memory loss, the disease causes an overall loss of cognitive ability, which affects functions such as speech and vision [2]. With ageing as the biggest risk factor for onset, it is expected that up to 139 million people will be affected by dementia by 2050 [3].

The specific role of several key pathological features of AD, namely amyloid-β plaques and neurofibrillary tangles [2, 4, 5], have been extensively studied as potential targets for therapeutic intervention. Despite substantial research into the mechanisms involved, unfortunately, there is currently no cure. When one considers that ageing is the biggest risk factor for the onset of AD [2, 6], it is possible that emphasising focus towards understanding mechanisms associated with natural ageing may help to reveal strategies for prevention. If the pathways underpinning ageing, and the switch between natural ageing/cognitive decline and AD can be understood, then potential targets for prevention may be revealed [7]. Stated simply, if the risk factor can be addressed, perhaps disease onset can be minimised. Developing research tools that can be used to further enhance understanding of the chemistry of brain ageing, and how this may place the brain at increased risk of developing neurodegenerative disease, is the primary research motivation of this thesis.

1.2 Changes in Metal Ion Homeostasis in the Ageing Brain

There is a plethora of biochemical changes that occur in the brain during natural ageing including oxidative stress, mitochondrial dysfunction, inflammation, and altered glucose metabolism to provide some examples [7, 8]. In addition, altered metal homeostasis is observed during ageing and has gained interest as a line of inquiry for understanding ageing processes. It is well established that transition metals such as iron (Fe), copper (Cu) and zinc (Zn), hold significant roles in processes required for healthy brain function (discussed further for Zn and Cu in sections 1.3 and 1.4) [9-12]. It is also well established that metal ion dyshomeostasis can result in deficits in cellular function, cognitive decline and potentially the development of neurodegenerative disorders [9, 13-16]. Numerous studies have reported overall increases in the content of these metals with ageing [17, 18], however, there is evidence that conversely suggests

localised metal deficiencies of these metals in the hippocampus [19, 20], a central region for memory function [21], directly relates to memory loss and dementia [22].

Dis-regulation of metal ions can induce oxidative stress, either directly through Fenton and Fenton-like chemical pathways in the case of Fe and Cu, or indirectly in the case of Zn. During Fenton chemistry the reduced form of Fe and Cu ions (Fe^{2+}, Cu^{+}) catalyses the decomposition of hydrogen peroxide to yield hydroxyl radicals (equation 1) [23-26].

Equation 1: $Fe^{2+} + H_2O_2 \rightarrow Fe^{3+} + OH^- + OH\cdot$

If unregulated, these hydroxyl radicals can then abstract weakly bound hydrogen atoms from polyunsaturated fatty acids, triggering lipid peroxidation processes [27]. While the formation of radicals occurs naturally in the brain during metabolic processes, excessive levels of these redox active metals and an inability to maintain sufficient antioxidant defences has the potential to cause significant oxidative damage [5, 28, 29]. In addition to lipid oxidation, oxidative damage to nucleic acids and proteins can be another consequence of unregulated free radical production [29]. Altered Zn homeostasis can also indirectly induce or exacerbate oxidative stress through a number of proposed mechanisms. Zn plays a vital role in a variety of antioxidant mechanisms through its function as a cofactor or structural component for proteins and enzymes that scavenge oxidants (e.g., superoxide dismutase (SOD) and metallothionein), through binding to protein cysteine residues to prevent disulfide bridge formation, and also through competitive lipid membrane binding with Fe and Cu leading to associated downstream effects on Fenton chemistry [30-33]. While the extent of oxidative stress caused by inhibition of some of these proteins could be minor (e.g., for SOD[30]), it is evident that Zn homeostasis is important for antioxidant defences, and hence indirectly linked to oxidative stress. It has also been proposed that altered Zn concentration can disrupt the electron transport chain in mitochondria, leading to mitochondrial dysfunction and the production of reactive oxygen species (ROS) which in turn cause oxidative damage [30]. Interestingly, the ROS can trigger further release of Zn from proteins such as metallothionein, which can cause further disruption to mitochondria and other enzymes, leading to a dangerous cycle [34]. While all possible mechanisms for Zn mediated oxidative stress have not been described, it is clear that Zn dyshomeostasis can play a pivotal role in its onset and escalation.

Cu, Fe, and Zn ions are also thought to promote protein mis-folding which is a characteristic feature of many neurodegenerative diseases including AD, Parkinson's disease, and Huntington's disease [35]. Protein aggregation is generally triggered by a change in protein conformation which alters the intermolecular forces and induces a change in secondary protein structure from α-helices to β-sheets which can then further aggregate [36, 37]. Factors such as pH, post-translational modifications (e.g., phosphorylation), and protein mutation can all have an influence on protein aggregation [36], but of specific relevance is the proposed direct and indirect pathways through which metal ions can induce aggregation. One proposed mechanism is that metal ions can coordinate through specific amino acid residues, which instigates a conformational change that enables increased hydrophobic or dispersion forces between non-polar (hydrophobic) side chains of amino acid residues, in turn leading to mis-folding and aggregation [36, 37]. This mechanism is partly dependent on the nature of the amino acid residues and their positioning, so mutations to proteins (i.e. slight differences in the amino acid sequence) may increase susceptibility to aggregation after metal binding [36]. Another proposed mechanism is that metal ion induced oxidative stress could cause oxidation of amino acid side chains, which would lead to conformational changes, altered intermolecular forces, and subsequent aggregation [36]. For example, thiol groups from cysteine residues could oxidise to form disulfide bridges, which disrupts the hydrogen bonding network, and promotes formation of β-sheets which can further aggregate [38]. Protein mis-folding and aggregation can be detrimental to healthy brain function because many enzymatic reactions are dependent on 3D protein structure [36]. The potential role of Cu, Fe, and Zn in protein mis-folding and aggregation provides another example of why strict regulation of these ions is vital for healthy brain function.

While metal ion dyshomeostasis is frequently associated with cognitive decline and brain pathologies during ageing and neurodegenerative disease, direct evidence of pathways that cause metal dyshomeostasis remains lacking. Therefore, further characterisation of metal ion changes, in addition to the cellular biochemical alterations that occur both prior to and after metal dyshomeostasis, may indicate potential mechanistic links between disturbed metal homeostasis and memory loss during ageing. In turn, this may reveal potential pathways for preventative methods and therapeutic interventions to minimise, delay, or prevent the onset of AD. In order to appreciate the role that metal ion dyshomeostasis may play in ageing and

neurodegenerative disease, necessary context is needed with respect to the role of metal ions in healthy brain function.

While Fe, Cu, and Zn are all vital for healthy brain function, each with specific and important roles in various enzymatic processes, a significant portion of this PhD thesis focussed on developing methods to better understand the role of Zn during ageing (Chapter 3), with the intention of the developed method becoming applicable to the study of other transition metals. Additionally, localised increases in Cu, which will be discussed in section 1.4.3, were further investigated to identify whether elevated Cu levels induced oxidative stress, as would be expected through classic Fenton-like chemical pathways (studied in Chapter 4). Given that Zn and Cu were the primary metals of focus in this thesis, these are the two that will be discussed in further detail below.

1.3 Bioinorganic chemistry of Zinc

1.3.1 Concentration of Zinc in Brain Tissue, and Common Zinc Metalloproteins

Zn is the second most abundant trace metal in the body after Fe [39-41], and the brain contains the highest concentration compared to any other organ [10]. The estimated total brain Zn concentration is 150 µM [42] and although most Zn is bound to proteins as a structural, co-catalytic or catalytic component, an estimated 10-15% of it exists as labile Zn[40]. In most brain regions, the labile Zn is approximated to be at sub-nanomolar levels intracellularly, and around 500 nM in extracellular fluid [42]. Conversely, the synaptic vesicles of a subset of glutamatergic neurons within the forebrain, particularly the hippocampus, are proposed to contain a much higher Zn concentration, several hundred µM up to 1 mM [42, 43]. Within the Zn-rich glutamatergic neurons (sometimes termed “gluzinergic neurons”), Zn plays an important role as a neuromodulator for regulating glutamate receptor activities [44, 45]. In addition to its role in neuromodulation, Zn is involved in several enzymatic and metabolic processes and is a vital cofactor in over 300 enzymes [11, 13, 41, 46]. Furthermore, it enhances the performance of more than 2000 transcription factors [11]. Specific examples of Zn metalloproteins include Cu-Zn SOD, metallothioneins, Zn transporter proteins (ZnTs) and Zn-regulated and Fe-regulated proteins (ZIPs) [10, 13]. The latter three play key roles in maintaining Zn homeostasis within the brain [13]. Zn is also present in DNA-Zn finger proteins, which indicates a potential contribution to DNA recognition, apoptosis regulation, protein folding and lipid binding [47]; and Zn associates with myelin basic protein which contributes to axon myelin sheath stabilisation,

most likely through coordination with histidine residues [48, 49]. A prominent Zn containing enzyme is carbonic anhydrase which has the function of catalysing the hydration of carbon dioxide (CO_2) to form hydrogen carbonate (bicarbonate, HCO_3^-), which is an important equilibrium system for carbon dioxide transport and regulation of pH [50-52]. Zn plays an active role in this catalytic process through the Zn-hydroxide mechanism (a characteristic Zn enzyme mechanism) in which the exchangeable H_2O ligand bound to Zn is deprotonated to become a nucleophilic OH^- that attacks a carbonyl carbon (figure 1.1) [51]. For carbonic anhydrase, the nucleophilic OH^- attacks the carbon of a CO_2 molecule, resulting in a Zn-bound HCO_3^- ligand which is then released after displacement by another H_2O molecule [51, 52].

Figure 1.1: *General Zn-hydroxide mechanism that aids in the catalytic activity of some Zn*

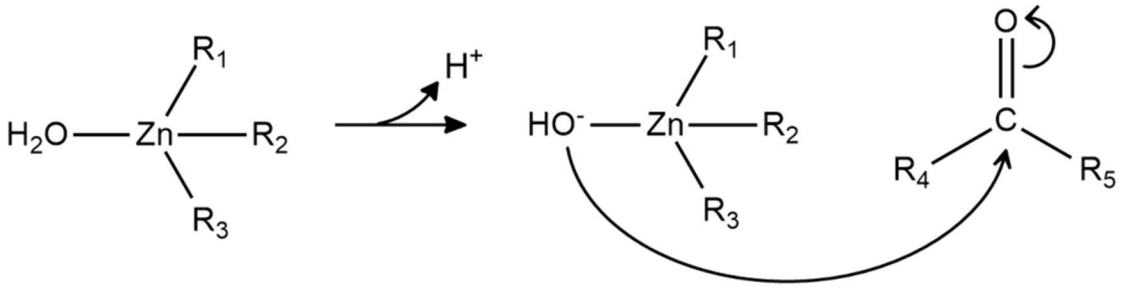

proteins. The first step involves hydrogen extraction from the exchangeable H_2O ligand to form a OH^- ligand that can then attack a carbonyl carbon [51, 52]. The carbonyl containing compound and complexes formed following the nucleophilic attack are dependent on the specific protein and catalytic process. It should be noted that the stereochemistry and geometry around the central atoms are not accurately depicted.

1.3.2 The Labile Zinc Pool

Of considerable interest with respect to memory function, is the concentrated pool of labile Zn in the synaptic vesicles of the glutamatergic neurons in the hippocampus [42, 45, 53]. The co-localisation of Zn with glutamate suggests that it may play a role in neurotransmission, and because Zn impacts signal transduction it is thought that Zn may also modulate synaptic growth and regeneration (synaptic plasticity) [10, 13, 54, 55]. In addition to this, depletion or redistribution of Zn within the hippocampus can contribute to cognitive decline or memory loss, suggesting that Zn directly impacts healthy memory function [22]. Previous studies have demonstrated that both AD and accelerated ageing models are associated with a decrease in this labile hippocampal Zn [20]. Despite extensive research into mechanisms associated with this labile pool and its proposed importance for healthy brain and memory function, its coordination chemistry and how this may change after release from the synaptic vesicles has not been fully elucidated [45, 55]. It is widely accepted that after release, the Zn diffuses across the synaptic cleft where it has an impact on the post synaptic neuron [10, 13, 54, 56]. Some propose that the Zn is in an ionic form, while others have suggested Zn-glutathione or Zn bound to metallothionein type proteins [55]. Zn-glutamate complexes have also been suggested as a result of the high concentration of both components [57]. Thiol based ligands such as cysteine which are binding sites for Zn in several proteins have also been proposed [55]. Interestingly, an externalisation mechanism in which Zn remains bound to the membrane when it moves to the extracellular space where it can be easily re-internalised, has also come to light [10]. In general, while there are several speculated vital functions that this labile Zn is required for, little is known about its chemical environment which inspired the focus of this part of the investigation.

1.3.3 Zinc Uptake and Transport

Zn's functional importance in the body requires strict regulation of uptake and transport. For Zn to be sufficiently transported, favourable binding to proteins and ligands is vital so an understanding of Zn coordination chemistry is of great importance. Zn exists exclusively in biology as Zn^{2+}, which has an electron configuration of [Ar] $4s^0\,3d^{10}$, meaning its coordination geometry preference is not impacted by ligand field stabilisation aspects [39, 41]. In serum, which plays a vital role in transporting Zn to the brain before uptake across the blood brain barrier (BBB), Zn exists in three main forms; 1) protein bound, 2) as low molecular weight complexes

and, 3) exchangeable or labile forms [46]. The protein bound fraction is the most abundant and accounts for 98 % of serum Zn [40, 46]. Of the Zn in this fraction, most is bound to albumin and represents the majority of exchangeable Zn in serum [40, 46]. Previous studies have revealed that the Zn binding site in albumin is 5 coordinate and occurs through two histidine residues, an aspartic acid residue, an asparagine residue, and a non-protein ligand which is likely to be water [58, 59]. The other main binding protein in serum which binds Zn in a much lower concentration is α_2-macroglobulin [59]. The low molecular weight complex form of Zn accounts for 1-2% of serum Zn and most of this is bound to amino acids such as cysteine and histidine [40, 46]. The labile pool of Zn represents an even lower percentage of serum Zn and is not well understood. The transport of Zn into the brain after circulation is facilitated by the BBB and cerebrospinal fluid (CSF) barrier [60]. In general, transport across the BBB can occur via passive diffusion across the cell membrane, or via active transport through specific receptor mechanisms, channels, or transporters [60]. The specific mechanism through which metals transport across this barrier is heavily dependent on the metal itself [60]. A proposed mechanism of Zn transfer involves histidine bound Zn being delivered to plasma membrane proteins or transporter proteins on the brain choroidal epithelial and capillary endothelial cells [60]. It has also been postulated that histidine bound Zn may be able to directly cross the plasma membrane [60]. Once Zn has crossed the BBB, it must then be able to transfer in and out of cells to fulfil its various roles in supporting healthy brain function. ZIPs are responsible for transporting Zn into cytoplasm, either from organelles or from the extracellular space, while ZnTs have the role of transporting Zn out of the cytoplasm and into sub-cellular organelles or vesicles [10, 11]. Of significant interest is ZnT3 which transports Zn from the cytoplasm into synaptic vesicles, some of which are concentrated with labile Zn [10, 11]. Divalent metal transporter 1 (DMT1) is also thought play a role in Zn uptake into neurons [40]. Finally, metallothioneins are vital for mediating Zn concentration in the intracellular space [10, 11, 61]. They have the capacity to bind up to seven Zn atoms at a time to account for excessive amounts in the cytoplasm and can release these atoms when the cell is Zn deficient [10, 11, 61]. In general, adequate transport of Zn to the brain, followed by efficient movement in and out of cells is required for healthy Zn homeostasis in the brain.

1.3.4 Commonly Encountered Bioinorganic Zinc Coordination Sites

To further probe and understand the possible chemical environment of labile Zn, it helps to further consider known Zn coordination sites in proteins, as this may provide insights into the likely ligand environment for labile Zn. Zn is most commonly bound to histidine, cysteine, glutamate, and aspartate amino acid residues in proteins, with the specific coordination environment dependent on whether its role is catalytic, structural, or co-catalytic [39, 62]. Catalytic sites typically contain an exchangeable H_2O ligand along with three other protein ligands; structural sites contain four protein ligands typically binding through cysteine; and co-catalytic sites, which require two metals for catalytic activity, generally have binding through aspartate and histidine residues, with the metals sometimes bridged by a H_2O molecule[62]. Some specific, simplified examples are provided in Figure 1.2, along with structures of the common amino acid ligands for Zn [63].

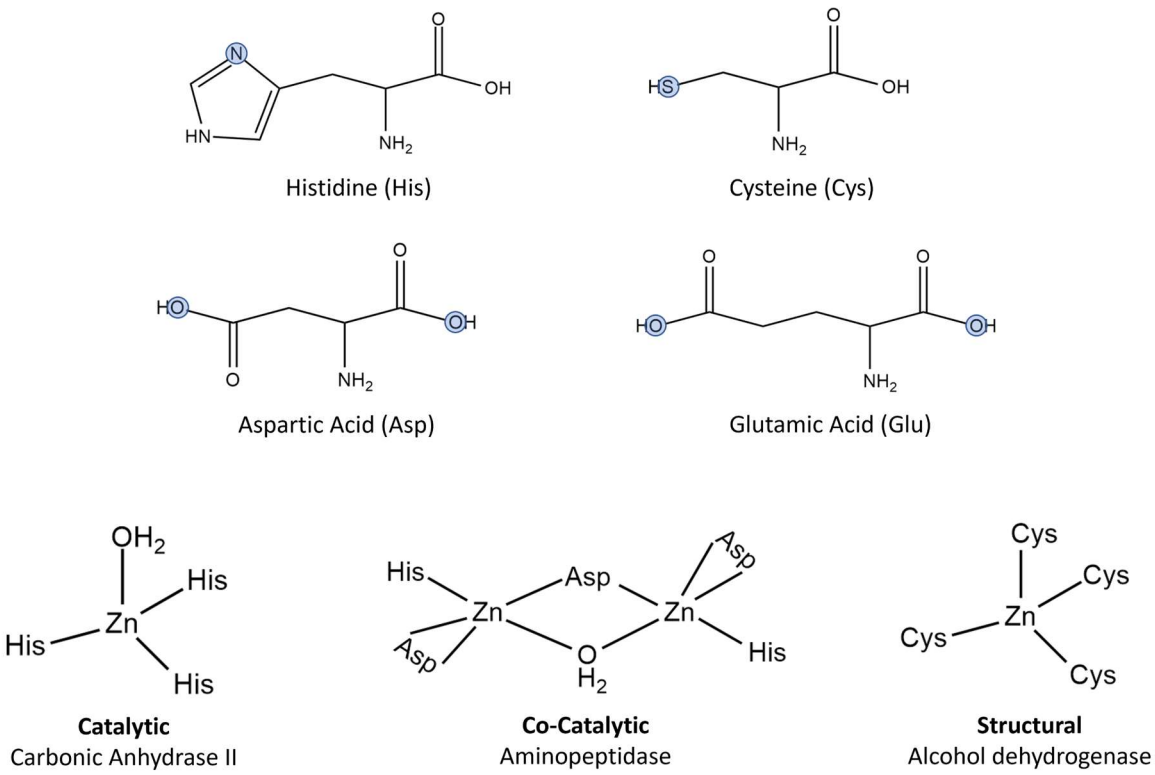

Figure 1.2: *Chemical structures of common amino acid ligands that bind to Zn in proteins. The blue circles indicate the atoms through which binding typically occurs. Examples of structural, catalytic, and co-catalytic Zn binding sites are also shown for specific proteins [62, 63]. For simplicity, the abbreviated names of the amino acids have been used, rather than the full structures, and the stereochemistry and geometry around the atoms are not accurately depicted.*

1.4 Bioinorganic Chemistry of Copper

1.4.1 Common Copper Metalloproteins and Coordination Sites

Cu is another essential metal required for healthy brain function and is the 3rd most abundant metal in the brain behind Fe and Zn [64]. It is a vital cofactor and structural component for several enzymes, with its redox activity central to the adequate functioning of many processes [9, 65-67]. Specifically, its presence in enzymes such as dopamine-β-monoxygenase, cytochrome C oxygenase, Cu-Zn SOD, and ceruloplasmin mean that Cu is vital for neurotransmitter synthesis, energy metabolism, antioxidant defences, and Fe metabolism, respectively [9, 65-67].

The predominant forms of Cu in biological systems include Cu (I) and Cu (II), with the former classified as a soft acid with preferential binding to soft ligands through atoms such as sulfur (S), and the latter classified as an intermediate or hard acid with preferential binding to intermediate ligands through atoms such oxygen and nitrogen (specific preference to N in imidazole rings) [41, 68]. Considering this, it is unsurprising that Cu is predominantly bound to histidine, cysteine, and methionine residues in proteins [69]. The specific coordination geometry of these Cu binding sites can influence its redox activity and stability within proteins [68]. Cu(I) adopts a d^{10} electron configuration so has flexible geometry, but often exists in 2, 3 and 4 coordinate complexes [68]. Cu(II) adopts a d^9 coordination geometry so preferentially exists as 4, 5 and 6 coordinate complexes with square planar, square pyramidal, and Jahn Teller distorted octahedral geometry, respectively [68]. The specific coordination geometry of Cu in proteins/enzymes can vary depending on the specific function of the enzyme and whether the role of Cu is structural or for redox activity [68]. The main Cu binding sites in biological systems have been classified into three types based on spectroscopic properties [41, 68]. These properties will not be specifically discussed, however, the coordination of Cu for each category is summarised in Table 1.1. Evidently, while the coordination geometries vary, most Cu containing enzymes likely bind Cu through the imidazole of histidine and the S of cysteine or methionine residues [9, 68, 69].

Table 1.1: *Summary of the Cu coordination for the main types of binding site in Cu proteins* [41, 51, 68]

	Ligands	**Coordination geometry**	**Other details**
Type I	• Cysteine and histidine (x2) • Possibly methionine and/or other amino acid residues	• Trigonal pyramidal • Loosely bound axial ligands can form distorted tetrahedral geometry or a distorted trigonal bipyramidal geometry	• Coordination geometry remains consistent regardless of the oxidation state of Cu so there is efficient electron transfer due to a smaller reorganisation energy • Enzymes involved in electron transfer processes often have type I binding sites
Type II	• Multiple histidine residues • Oxygen containing residues	• Distorted square planar geometry	• e.g., Cu-Zn SOD
Type III	• Two Cu atoms, each bound to three histidine residues and often bridged by two oxygen containing groups	• Trigonal bipyramidal geometry	

1.4.2 Copper Transport in the Brain

For Cu to bind in these enzymes and carry out subsequent functions, it must be transported appropriately. Transport into the brain and regulation of its homeostasis is not completely understood, but as with most species, including Zn, entry into the brain is likely facilitated by the BBB and possibly the blood CSF barrier [9, 70]. A major pathway for Cu to then enter cells is via Cu transporter 1 (Ctr1) which is predominantly expressed in the choroid plexus; the main cellular structure in the ventricular system [9, 65, 67]. Cu chaperones can then transport Cu to the target proteins for their required functions, which is important for prevention of non-specific Cu binding [9, 69, 71]. Upon entry into the cells, it is also possible for Cu to be bound by low molecular weight proteins and ligands such as metallothionein and glutathione [9]. Cu(I) forms a stable complex with glutathione and is thought to account for a significant portion of the labile or exchangeable Cu pool [9, 72]. Interestingly, while formation of this complex is thought to protect cells by minimising the possibility of ROS production from Cu(I) oxidation and preventing non-specific Cu binding, the complex itself is redox active, so has potential to induce oxidative stress by reacting with oxygen to form superoxide, or reacting with Fe(III) to produce Fe(II) which can then undergo Fenton chemistry to produce ROS [9]. Metallothioneins are thought to play a role in maintaining Cu homeostasis as was mentioned for Zn [9]. They have two metal binding domains and can reversibly bind up to 7 divalent metals, or up to 12 monovalent metals [9]. As for Zn, Cu can potentially be released from metallothioneins if cells become deficient, and bound by metallothioneins if the Cu content increases [9]. Interestingly, metallothionein expression increases with increasing Cu concentration, again supporting their potential role in maintaining Cu homeostasis [9].

1.4.3 Age-Related Changes to Brain Copper

Maintenance of Cu homeostasis is vital for healthy brain function and disturbed regulation has been implicated in various neurodegenerative diseases [15, 65, 67]. Depletion of Cu can impede the function of enzymes which will disrupt numerous important biological pathways, including but not limited to those listed previously [9]. Excessive Cu, however, can also have detrimental effects. As stated in section 1.2, in its reduced form (Cu(I)), Cu can react to form ROS that can trigger oxidative stress leading to protein and DNA damage, lipid peroxidation, and neuronal death, if not regulated appropriately [24, 28]. This process has been implicated in ageing and AD, and elevated levels of Cu have been observed during ageing.

One such example is the accumulation of Cu in the subventricular zone (SVZ) [65]. Pushkar et al discovered this phenomenon and localised the punctate increases of Cu to glial fibral acidic protein (GFAP) positive cells, which generally equates to astrocytes; the most abundant cell type in the brain [65]. Astrocytes are glial cells that are thought to metabolically support neurons, maintain extracellular ion homeostasis, and modulate synaptic plasticity and transmission [9]. Additionally, they may play an important role in metal metabolism, are a key source of some metallothioneins, and express metal transport proteins such as DMT1 [9, 65]. Significantly, it has been proposed that astrocytes are the cell type with the largest influence on Cu homeostasis [65]. Therefore, the Cu accumulation in these cells during ageing is particularly interesting and could be critical in understanding some underlying mechanisms vital for the ageing process. One possibility is that this increase in Cu is inducing oxidative stress, therefore, an aspect of this thesis was to investigate whether markers of oxidative stress increased concomitantly with age-related subventricular Cu increases.

1.5 Analytical Methods for Studying Zinc and Copper

Zn and Cu can be studied using bulk methods such as atomic absorption spectrometry (AAS) [73, 74] and inductively coupled plasma mass spectrometry (ICP-MS), which may be used with separation methods such as high-performance liquid chromatography (HPLC) and Gas Chromatography (GC). A number of techniques also exist to image Zn and Cu distribution in brain tissue, including laser ablation inductively coupled plasma mass spectrometry (LA-ICP-MS) [75-78], scanning electron microscopy (SEM), secondary ion mass spectrometry (SIMS) [79] and X-ray fluorescence microscopy (XRF or XFM) [20, 80-82]. In addition, a range of fluorescence probes and histochemical methods are available to stain certain chemical forms of Zn and Cu. For example, Zn sensitive fluorescence probes exist for studying labile extra-cellular Zn [56, 83-87], which complement the traditional Timm's and Danscher histochemical labile Zn stains [88-90]. Furthermore, there are radiolabelling methods such as positron emission tomography (PET) available which can demonstrate Zn uptake or Cu trafficking in the brain [91, 92]. All the above techniques have proven valuable to study the role of Zn and Cu in brain function, but there are limitations. For example, fluorescence probes and histochemical methods are well known to suffer potential issues with selectivity, particularly to other divalent metals such as calcium, and can be limited in their ability to enable accurate quantification [56]. Additionally, development of Cu(I) fluorescent sensors has been challenging given that it is a strong

fluorescence quencher [65]. Direct elemental mapping techniques (e.g., LA-ICP-MS, XFM) although specific to the metal, do not reveal information on the chemical form. A limitation to studying the chemical forms of Zn and Cu in brain tissue through combining separation methods (HPLC, GC) with either atomic or mass detection, are the potential changes in speciation that could occur during sample preparation (tissue homogenisation, fractionation, and extraction). Evidently, a technique that has the capacity to not only image the distribution of endogenous Zn and Cu in the brain, but also provide insights into its specific chemical form and relative concentration would be indispensable. X-Ray spectroscopic techniques have the capacity to fill these requirements and were hence a critical aspect of this thesis. Specifically, techniques were developed to image the chemical form of Zn in the brain, and while the use of X-ray techniques to image the chemical form of Cu was not the primary focus of this study, the methods developed for Zn will hopefully be applied to Cu (and other metals) in future studies. The relevance of Cu in this study was to identify whether its accumulation in the SVZ induces oxidative stress. This meant that methods appropriate for studying the markers of oxidative stress were required. This included X-ray spectroscopies, Fourier transform infrared microscopy, and immunoassays which will be further discussed in sections 1.6, 1.7.1, and 1.7.2.

1.6 X-Ray Fluorescence Microscopy (XFM) and X-Ray Absorption Spectroscopy (XAS)

1.6.1 General Introduction to Spectroscopy to Study Coordination Chemistry

As described in section 1.5, while a suite of analytical methods exist to study Cu and Zn content in tissues, most are bulk methods that do not provide information on the spatial distribution of metal ions, or are not well suited to study the chemical form of the metal. For these reasons, this thesis has focussed on development and application of X-ray spectroscopic methods to study metal speciation in brain tissue.

Broadly, spectroscopy is the study of the interaction between electromagnetic radiation (light) and matter, and it can provide a wealth of chemical information about a sample [93, 94]. Classical interactions between electromagnetic radiation and matter include absorption, excitation, emission, and scattering processes. Electromagnetic radiation has both wave-like and particle-like properties [93, 95]. When describing the particle-like properties of electromagnetic radiation, one typically uses the term “photons” [93-95]. Photons have specific energies (E) that are proportional to the frequency (v), and inversely proportional to the

wavelength of light (λ) based on equations $E = hv$ and $E = \frac{hc}{\lambda}$, where c is the speed of light and h is Planck's constant [95]. When photons interact with a sample, if the photon energy exactly matches that of an electronic transition, the energy of the photon may be absorbed and in turn promote an electron to a higher energy state (electronic excitation) [93-95]. From an excited state, an electron may then return to a more stable, lower energy state (often the ground state), and in doing so release energy in the form of a photon, during relaxation [93, 95]. The energy (and therefore wavelength) of light that is absorbed to generate electron excitation, and also emitted during relaxation of an excited electron, is inherently linked to the electronic structure of an atom or molecule. The use of spectroscopy to measure electronic transitions in molecules is thus an excellent analytical tool to study molecular structure.

Electronic transitions within molecules occur between molecular orbitals which are formed from a combination of atomic orbitals [51]. For coordination complexes, which are specifically relevant to this thesis, this includes orbitals from the ligands and the metal centre. The nature of the ligands and their geometry around the metal centre directly impacts the energy and degeneracy of the molecular orbitals, meaning energy of the electronic transitions are directly influenced by the chemical structure [41, 51]. A prominent example of this is the splitting of the metal d orbitals that is observed in the presence of bonding ligands [41, 51]. The splitting varies depending on the proximity of the binding ligands to the orbitals, with close proximity resulting in greater repulsion and higher energy molecular orbitals [41, 51]. This means that complexes with varied coordination geometries exhibit differences in orbital degeneracy and splitting [41, 51]. A typical molecular orbital diagram for an octahedral metal coordination complex is shown in figure 1.3 [41]. The energy and splitting of molecular orbitals can also be further influenced by the ligand type, and it is worth noting that the impact of altered ligand type and coordination geometry on molecular orbital energy is not necessarily limited to the d orbitals.

Often, the orbitals of particular interest are the highest occupied molecular orbital (HOMO) (which includes the d orbitals for transition metal complexes) and the lowest unoccupied molecular orbital (LUMO) which are influenced by ligands and geometry as described above [51]. The fact that each ligand type and coordination geometry will have a slightly different

effect on the molecular orbital energies, and hence the energy of electronic transitions, further emphasises the benefit of using spectroscopic techniques to probe chemical structure.

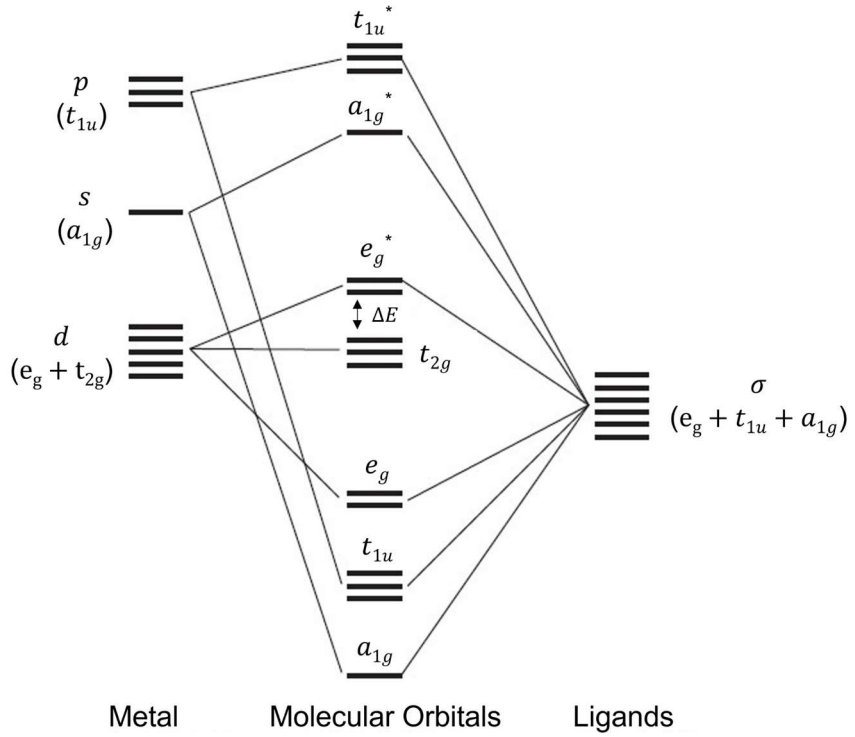

Figure 1.3: *A simplified molecular orbital diagram for an octahedral transition metal complex (adapted from [41])*

1.6.2 Theory Behind X-Ray Techniques

For purified coordination compounds, spectroscopic analysis of HOMO to LUMO transitions using light in the UV – Vis range is most common for studying electronic structure. This is, however, not a practical analytical tool in complex biological samples, where there is substantial overlap of the valence electronic transitions of different metal ion complexes, in addition to those of organic molecules. Fortunately, X-ray spectroscopy provides a unique analytical tool to probe valence electronic structure, with elemental specificity. The elemental specificity of X-ray spectroscopy is because the excitation process is from a core (1s) or inner-shell electron to an unoccupied molecular orbital (usually the LUMO), and different elements inherently have substantially different binding energies of core and/or inner-shell electrons.

1.6.3 X-Ray Absorption Spectroscopy (XAS)

In an XAS spectrum, the X-ray absorption or excitation of the core electron is signified by a sharp, intense increase in absorption, known as the absorption edge, or "white line" feature [96]. Labelling of the absorption edge is based on the shell and subshell from which the electron is excited, with the K-edge referring to a 1s electron excitation, L edge for a 2s (L_I) or 2p (L_{II}, L_{III}) electron excitation, and M edge for 3s (M_I), 3p (M_{II}, M_{III}), and 3d (M_{IV}, M_V) excitations [97-99]. The region of the spectrum within +10 eV of the absorption edge is usually referred to as X-Ray Absorption Near Edge Structure (XANES), while the energies just below the absorption edge is referred to as the "pre-edge" [51]. The post edge region can be split into two sections; the near edge X-ray absorption fine structure (NEXAFS) which lies between +10 eV and +50 eV of the absorption edge, and the extended X-ray absorption fine structure (EXAFS) which lies at energies beyond +50 eV from the absorption edge [51]. Often, the latter two are collectively referred to as the EXAFS region which will be the case for this thesis. Each of these spectral regions can provide slightly different information and are outlined in figure 1.4.

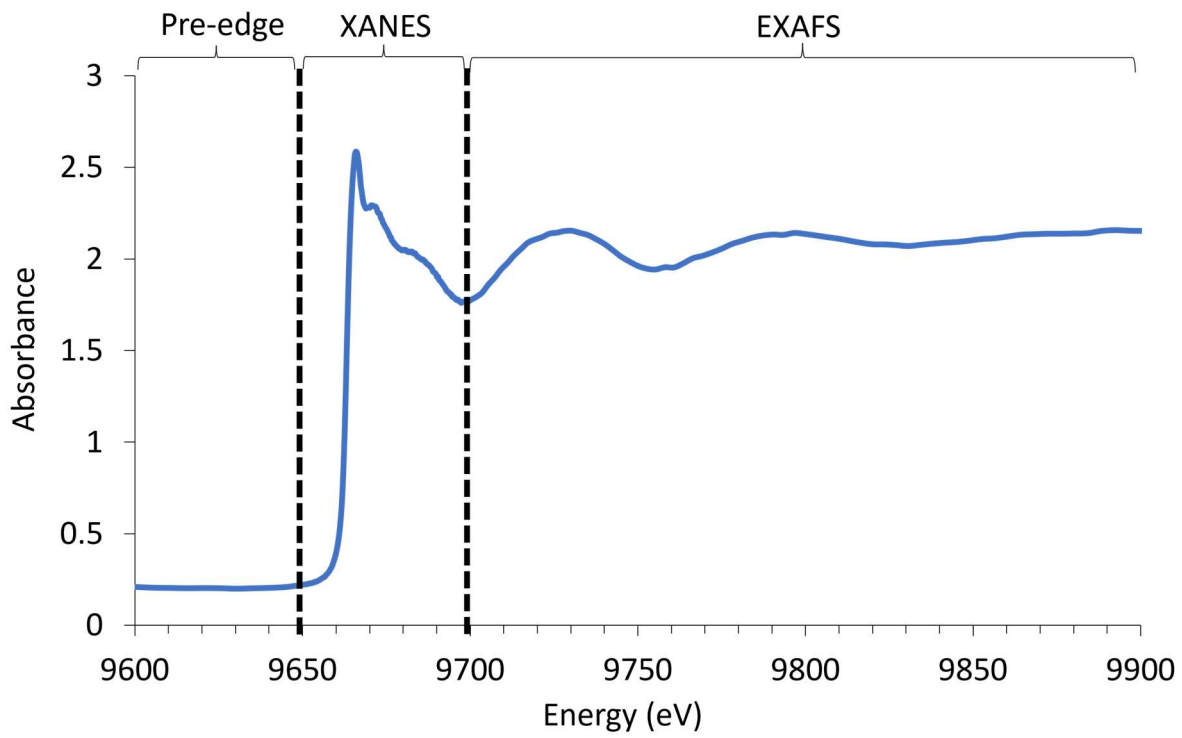

Figure 1.4: *A Zn K-edge XANES spectrum with the general pre-edge, XANES, and EXAFS regions outlined. Typically, the pre-edge region is the energies just below the absorption edge (white line feature), the XANES region includes the absorption edge and energies +10 eV above the edge, and the EXAFS region (sometimes split into NEXAFS and EXAFS but outlined collectively in this figure) is all energies above the XANES region* [51].

To better understand the chemical information these spectral regions can provide, one must further consider the fundamental processes occurring. Prior to ejection of the core electron to the continuum, the electron may be excited in resonance to unoccupied orbitals. The electronic transitions are governed by selection rules, so the most intense features in an XAS spectrum arise from dipole allowed transitions where Δl=±1 [97]. For a K-edge which involves the excitation of a 1s electron [100], the transition is to an unoccupied p orbital (ie. 1s → np where n is the energy of the orbital assigned by the quantum number n) [99]. When the change in l=±2 (e.g., 1s → nd), the transition is dipole forbidden but quadrupole allowed and gives rise to much lower intensity peaks [99]. The intense dipole allowed transitions are responsible for the sharp absorption edge in the XANES region of the spectrum, while the quadrupole allowed transitions are one source of the low intensity features seen in the pre-edge region. For K-edge spectroscopy of transition metals with incomplete 3d orbitals, the pre-edge peak can also be attributed to 3d-4p orbital mixing [99], thus permitting dipole allowed transitions

into the d-manifold. As 3d-4p mixing is highly dependent on coordination structure and ligand bonding, analysis of pre-edge features can provide valuable information on the local symmetry of the atom and energy of the excited states [99].

Given that the K absorption edge of the XANES region is based on a 1s → np transition, the position, intensity, and shape of the XANES spectrum is impacted by factors that influence both the binding energy of the core electron and the energy level of the unoccupied p orbitals [99]. Consequently, XANES spectroscopy displays remarkable sensitivity not only to the element, but also its oxidation state, ligand type, coordination geometry, and the degeneracy of molecular orbitals [98-100]. Further details regarding how each of these factors can affect the XANES region of the spectrum are detailed in table 1.2.

While *ab initio* interpretation of the XANES spectrum is still developing, the use of XANES to "fingerprint" the metal ion coordination environment is well established and examples will be further discussed in section 1.6.6. Through the construction of spectral libraries that model different forms of metal ion coordination, it is possible to elucidate coordination chemistry *in situ* within complex chemical environments, and this forms a key foundation of the experimental framework for this thesis.

Table 1.2: *The effect of various aspects of coordination chemistry on the white line feature of the XANES spectrum* [100]

Property	**Trend in XANES spectrum**	**Justification**
Atomic Number	Energy of the white line feature increases with increasing atomic number.	Increasing atomic number means an increasing number of protons which results in stronger electrostatic attractions between the core electrons and the nucleus meaning they will be more tightly bound (higher binding energy).
Oxidation State	Energy of the white line feature increases with increasing oxidation number.	Increasing oxidation number means an increased ratio of protons/electrons which results in stronger electrostatic attractions between the core electrons and the nucleus meaning they will be more tightly bound (higher binding energy).
Ligand Type	Energy of the white line feature increases with increasingly electronegative or electron withdrawing ligands.	An electron withdrawing ligand or ligand binding through an electronegative atom will draw electrons away from the nucleus. This causes the nucleus to become relatively more positive, meaning there will be stronger electrostatic attractions between the core electrons and the nucleus. Consequently, core electrons will be more tightly bound (higher binding energy).
Coordination Geometry	White line intensity increases with increasing symmetry. Multiple features or "peaks" expected with less symmetry.	A complex with more symmetrical geometry (e.g., Octahedral) will have a narrow, intense white line feature because of the degeneracy of the orbitals that the core electrons are excited to (LUMO). Additionally, the degeneracy will mean there is a single peak. When the LUMOs are not degenerate, usually due to a lack of symmetry, there are often multiple features (i.e. peaks) in the absorption edge and the white line intensity is reduced.

The EXAFS region of the spectrum arises from the constructive and deconstructive interference pattern caused when the emitted X-Ray of the atom of interest is backscattered by the electrons of adjacent atoms [96, 98, 100]. It can provide valuable information on the identity and quantity of bound atoms (based on the electron density), in addition to the average bond lengths [98, 100]. While it is evidently an extremely advantageous tool, the interference patterns of an impure sample can cause the signal to cancel out, and an average bond length is less meaningful for a complex sample [98, 100]. Consequently, EXAFS is mainly suitable for pure samples and was not applied in this thesis.

A key requirement for XAS analysis of metal ions at µM detection limits in biological samples is a bright (high photon density) and tuneable X-ray source [97]. For this reason, most XAS experiments are conducted at synchrotron radiation facilities [99]. A full description of the operation of a synchrotron is beyond the scope of this thesis, but in brief; a synchrotron facility is a type of particle accelerator, accelerating electrons up to relativistic velocities (99.9% the speed of light) [101]. When the acceleration of the relativistic electrons is changed, induced by exposure to a magnetic field, the electrons release a brilliant, broad band light source (synchrotron light) [101]. Synchrotron light is a key requirement for not only XAS measurements, but also XFM and chemically specific XFM measurements (described in sections 1.6.4 and 1.6.5 below).

1.6.4 X-Ray Fluorescence (XRF) and X-ray Fluorescence Microscopy (XFM)

Following the creation of a core hole during X-ray absorption and electron excitation, a higher energy electron (relative to the core hole) can fill the vacancy, and in doing so loses energy in the form of photo-emission [97]. The X-ray emission process (referred to as X-ray fluorescence from here in) also follows the selection rules and thus, the 2p → 1s electron transition is the most intense and most commonly measured X-ray fluorescence (and termed a K_α emission) [97]. The emitted X-ray fluorescence is characteristic to each element, meaning X-ray fluorescence is well suited to measure multiple elements simultaneously in samples of interest (provided the incident excitation X-ray energy is above the binding energy) [97]. The use of specialised mirrors and focussing optics enables the incident X-ray beam to be micro-focussed to small spot sizes and then raster scanned across the sample to produce elemental maps [97, 102]. The specific data collection and instrumental parameters are dependent on the sample, but typically, a lower resolution map to provide an overview of the sample is

collected, which is used to further refine regions of interest for higher resolution maps [102]. The dwell time of the X-ray per pixel is dependent on the concentration of the element of interest, so by adjusting the raster scan step size and the dwell time, high spatial resolution maps showing the distribution of trace elements within various samples can be collected.

1.6.5 Chemically Specific XFM

The capabilities of XFM can also be expanded to mapping multiple chemical species of a single element, through a hybrid of XAS and XFM experimental configurations. As described in section 1.6.3, the absorption edge for an element is highly sensitive to factors such as oxidation state, ligand type, and coordination geometry [98-100]. Therefore, while a traditional XFM elemental mapping experiment is performed at a single excitation energy that is set well above the binding energies of multiple elements of interest, in chemically specific XFM, several elemental maps of the same element are collected using a series of subtly different incident energies [97, 102]. The subtly different incident energies are specifically chosen to correspond to the white line positions of specific oxidation states of the elements of interest, or pronounced features in the near edge [97]. The most common examples of chemically specific XFM found in the literature include imaging elements that commonly exist in numerous oxidation states, e.g., elements such as S, Se, and As [103-105].

Ideally, rather than performing chemically specific XFM, one would perform XANES imaging, in which each pixel in the image contains a full XANES spectrum. This has been difficult to achieve in the past, particularly for biological samples, largely due to limitations in instrument capabilities that have prevented imaging larger areas with adequate sensitivity in practical time frames. Further development and advancements in beamline components such as detectors and focussing optics has significantly increased the practicality and applicability of XANES imaging to biological samples, enabling reduced analysis times and improved detection limits for full spectrum per pixel imaging [106].

One approach to XANES imaging involves collecting multiple images (e.g., over 100) with incident energies scanning across the entire XANES spectrum at specified energy step sizes [102]. To accurately distinguish between chemical species using this mode and to build a spectrum of similar resolution to those collected using XAS, the energy step sizes across the K-absorption edge should be small. To identify the most suitable step sizes for full spectrum per pixel imaging, ideally, a bulk XAS experiment should be completed prior to chemically

specific imaging to identify the expected chemical species [97]. A schematic depicting the XANES imaging mode of collection is shown in figure 1.5.

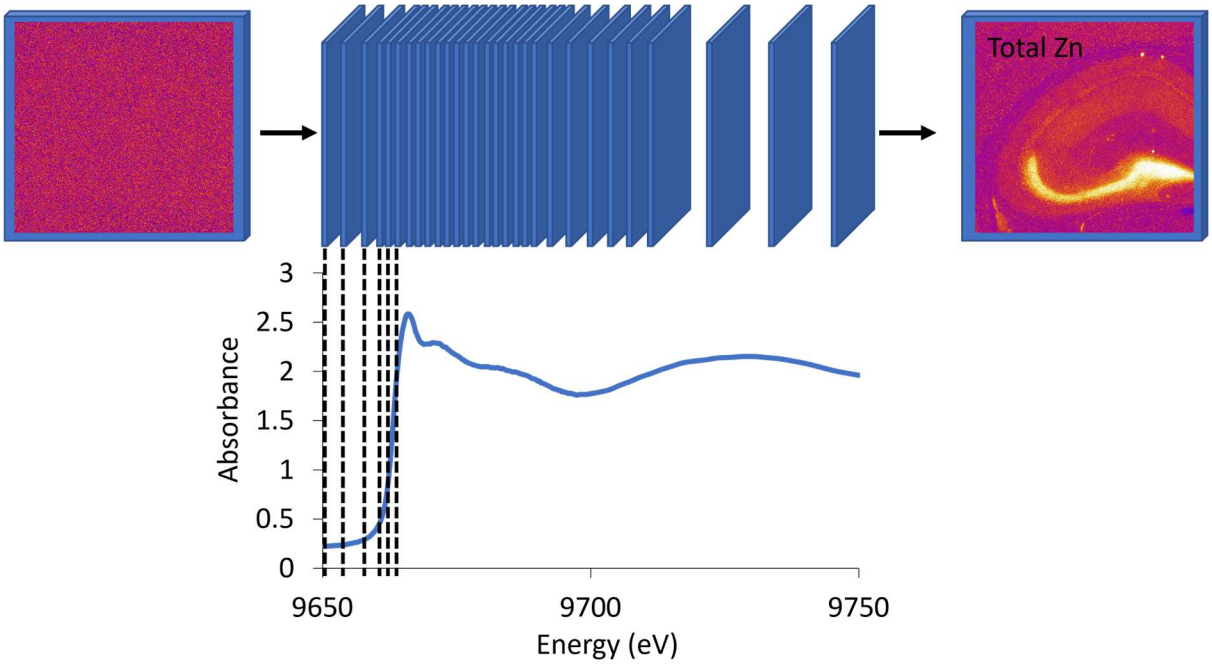

Figure 1.5: *The process of collecting full spectrum per pixel XANES images. Several images are collected at multiple incident energies across the XANES spectrum, with smaller energy step sizes used across the absorption edge to ensure adequate spectral resolution is achieved and that various coordination species can be distinguished. The number of images collected can vary depending on the experiment, and a stack of the images creates the XANES spectrum. It should be noted that this diagram does not accurately depict the exact step-sizes, but rather demonstrates the general process and highlights the use of smaller step sizes in the XANES region.*

Another approach that enables spatially resolved XANES analysis is to use micro-XAS (μ-XAS) which involves collecting a fluorescence image of the element of interest to enable selection of key regions of interest from which a full XAS spectrum can be collected (i.e. XANES spectrum collected for selected single points on sample) [97]. As with all techniques, both modes have their advantages and disadvantages which are summarised in table 1.3. The XANES imaging mode that is applied not only depends on the sample and experiment requirements, but also on the available instrumentation. Both modes were applied in this study at two separate synchrotron facilities.

Table 1.3: *The advantages and disadvantages associated with the methods for obtaining spatially resolved XANES spectra* [97]

	Advantages	**Disadvantages**
μ-XAS	• Can collect full XAS spectrum ○ High energy resolution spectrum	• Full spectrum can only be collected for a limited number of small regions • Extended exposure to potentially damaging X-rays
Chemically specific imaging	• Can image the distribution of various chemical species • Capability for full spectrum per pixel imaging	• Requires prior knowledge of chemical species in sample • Full spectrum per pixel imaging involves extended exposure to potentially damaging X-rays

1.6.6 Past Applications of XAS and XFM to Brain Tissue

XAS, XFM, and chemically specific XFM have been applied in multiple studies of brain tissue, which are described below.

The importance of transition metals such as Fe, Cu and Zn to healthy brain function (see section 1.2) mean that they have been a popular target for elemental analysis of brain tissue using XFM. These metals, in addition to several other elements, have been studied in relation to neurodegenerative diseases such as AD and Parkinson's disease [107-109], and have also been studied after different types of stroke [110-112]. For example, multiple elements have been mapped in the hippocampus of a mouse model of accelerated ageing, and the Fe, Cu, and Zn distribution has been studied in protein aggregates associated with AD [20, 81]. Additionally, elemental analysis of dopaminergic neurons and Lewy bodies in Parkinson's disease brains has been completed [107], and the elemental distribution in regions surrounding tissue damaged by stroke has also been investigated [110]. Several other studies have also applied XFM elemental analysis to brain tissue, including but not limited to investigations relating to epilepsy, schizophrenia, and cerebral malaria [113-115]. While all the previous XFM applications to brain tissue have not been discussed in detail, it is evident that it is a well-established and indispensable technique for the analysis of elemental and metal homeostasis in the brain.

While XFM has been widely used to study metal distributions in brain tissue, applications of XANES to brain tissue is less common, with only several examples present in the literature including studies of Fe anomalies in avian brain tissue [116], Cu accumulations in brain lateral ventricles of rat tissue [65], and S speciation in the rat cerebellum and brain stem to provide some examples [103, 117]. Numerous examples of application of XANES to investigate biological tissues other than brain tissue can be found in the literature, and include studies of the chemical form of metals such as Fe [118-122], manganese (Mn) [123], and Cu [122, 124-126], and of other elements, namely, S [103, 117, 127], arsenic (As) [128], and selenium (Se) [129-132]. These studies have been carried out in biological tissues including the liver, hair, kidneys, cancer cells, and tumours. In addition to XANES analysis, chemically specific imaging has been also been achieved for elements such as S [103] and Fe [118, 119, 133], but has not yet been applied to study Zn speciation in brain tissue. To further develop this capability, a key focus of this thesis was to first develop a XANES spectral library to identify the most abundant Zn species in brain tissue. While the application of this specific approach to study Zn in brain tissue is novel, the use of Zn XANES spectral libraries has been applied to bacteria [134], cancerous tissue [135], plant tissues [136-138], and metalloproteins [139, 140]. An expansive library of Zn^{2+} model compounds of biological relevance, characterised by XANES and X-ray emission spectroscopy, has also been reported [141].

1.7 Correlating Zinc and Copper Changes with other Biochemical Alterations

Identifying biochemical changes that occur concomitantly with metal dyshomeostasis, may help to enhance understanding of the mechanisms contributing to cognitive decline during ageing. More specifically, if particular cell types or biochemical components (e.g., proteins, lipids. etc) appear susceptible to change with ageing, this might reveal certain pathways that play a direct role in the ageing process. One such approach is to use a combination of vibrational spectroscopy and immunohistochemistry, in a "multi-modal" workflow. Vibrational spectroscopy is particularly useful for biochemical applications given its ability to detect a wide variety of functional groups [95]. Immunohistochemistry relies on antibody recognition of specific proteins/antigens [142] so can be used to identify and study cells and their health by targeting various cell-specific proteins. Specific details on vibrational spectroscopy and immunohistochemistry are described in sections 1.7.1 and 1.7.2 below.

1.7.1 Theory Behind Vibrational Spectroscopy

Infrared (IR) and Raman spectroscopy are specific examples of vibrational spectroscopy and are dependent on molecular vibrations. A molecule with n atoms can have 3n-6 vibrational modes if non-linear, and 3n-5 vibrational modes if linear [93, 95]. 3n arises from the 3 directions in which a molecule can move in 3-dimensional space, while -6 accounts for non-vibrational movement including the 3 translational modes where the whole molecule moves, and the 3 rotational modes around a molecules centre [51, 93, 95]. The two main categories for vibrations include stretching and bending, with each of these containing sub-classifications that are further depicted in figure 1.6 [93, 95].

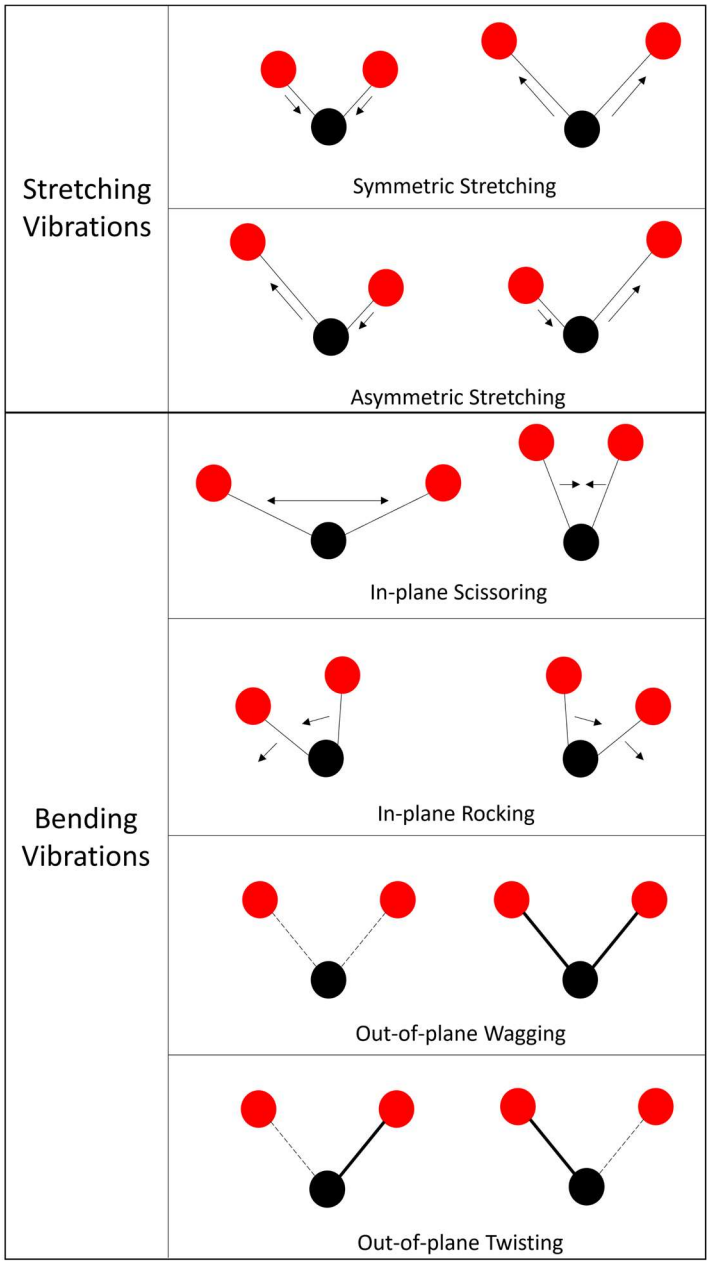

Figure 1.6: *Types of stretching and bending molecular vibrations. While the provided examples depict H_2O or a similar molecule, they are applicable to a range of molecules. For the wagging and twisting vibrations, the dotted lines represent movement into the page and the thick solid lines represent movement out of the page. Adapted from [93, 95].*

Importantly, these vibrations occur at specific and predictable frequencies that depend on the atoms in the bond, the bond strength, and the bond length. For a molecular vibration to be considered IR active and appear in an IR spectrum, it must cause a change in dipole (change in charge distribution) of the molecule [93, 95]. IR spectroscopy involves first irradiating the sample with light in the IR frequency range. If the incident photon frequency matches that of the molecular vibration, then the photon can be absorbed and the amplitude of the bond oscillations or vibrations will increase [93, 95]. The incident energy is not sufficient to excite electrons to a higher electronic state, however, they will be excited to a higher vibrational level in the ground electronic state. As stated previously, bonds vibrate at specific frequencies and therefore, the frequencies that are absorbed can reveal information about the types of bonds or functional groups present in a molecule [93, 95]. Additionally, the IR absorption follows the Beer-Lambert law ($A = \epsilon bc$, where A is absorbance, ϵ is molar absorptivity, b is path length, and c is concentration) meaning that the absorbance is proportional to the concentration, so the IR absorbance can also provide information on relative concentrations of these bonds or functional groups [95].

Raman spectroscopy is a scattering technique that is complementary to IR spectroscopy and requires the molecular vibrations to cause a change in polarisability (distortion of the electron cloud) of the molecule [93, 95, 143]. When the sample is irradiated with a monochromatic beam, the incident photons cause electrons to be excited from the ground state to a virtual vibrational state as the electron cloud distorts and energy is absorbed [93, 95, 143]. It is called a "virtual" vibrational state because the transition is not quantised and electrons do not resonate with a specific energy level [93, 95]. When the electron cloud returns to its natural state and electrons transition back to the ground state, the energy of the photons scattered can either be equal to the energy absorbed (elastic scattering), or different (inelastic scattering) [93, 95, 143]. The former is termed "Rayleigh scattering" and is the most probable outcome, while the latter is termed "Raman scattering" and is much less intense based on the reduced probability of occurrence [93, 95, 143]. Raman scattering forms the basis of Raman spectroscopy and can be further categorised depending on whether the energy of the scattered photon is less than or greater than the energy that was absorbed. Stokes scattering describes the former where the scattered photon energy is less than the absorbed photon energy, and results from the electron relaxing to a vibrational level higher than the ground state [93, 95, 143].

Anti-stokes scattering refers to when the scattered photon energy is greater than the absorbed photon energy and requires the electrons to already be in a higher vibrational level prior to absorption [93, 95]. Given that most electrons will be in the ground state unless at a higher temperature, anti-stokes scattering is much less probable than stokes scattering [93]. The difference between the incident energy and the emitted energy is termed the "Raman shift" and is dependent on the bonds and functional groups present in the molecule (i.e. the molecular vibrations present). It should be noted that the Raman shift is independent of the excitation wavelength (i.e. difference in energy between absorbed photon and scattered photon remains consistent) and falls in the IR absorbance frequency range, resulting in similarities between IR and Raman spectra [93, 143]. A process that often competes with Raman and can interfere in a Raman spectrum is fluorescence [93, 95]. Fluorescence also involves the absorption of a photon resulting in excitation of electrons to a higher electronic state. Specifically, when the sample is illuminated with a wavelength of light within the molecular absorption band, electrons are excited to vibrational levels in a higher electronic state, then relax to the lowest vibrational level of the excited state prior to radiative emission (fluorescence) when electrons return to the ground state [93]. The non-radiative emission that occurs prior to fluorescence, means the fluorescence wavelength is generally always lower than the excitation wavelength [93]. Since radiative emission always occurs from the lowest vibrational level of the excited state, the fluorescence wavelength is independent of the excitation wavelength. While they can be considered competing processes, the fundamental differences between fluorescence emission and Raman scattering is that fluorescence is a true absorption/emission process while Raman scattering is a scattering process [93]. Essentially, fluorescence occurs on a longer time scale and involves transitions between specific quantised electronic states. Therefore, the fluorescence signal involves specific wavelengths unique to the molecule that is being studied, and consequently the fluorescence signal does not remain consistent across all wavelengths. Conversely, Raman scattering is a much faster process, and because the Raman shift remains consistent regardless of excitation wavelength, various excitation wavelengths can be utilised [93, 95]. Given that fluorescence emission is typically a much stronger signal than Raman scattering, it can be problematic for Raman experiments [95]. Therefore, to minimise any potential fluorescence signal swamping the Raman spectrum, generally, excitation wavelengths away from the absorption band of

the analyte are selected. A diagram summarising the absorption processes underpinning IR, Raman, and fluorescence are detailed in figure 1.7.

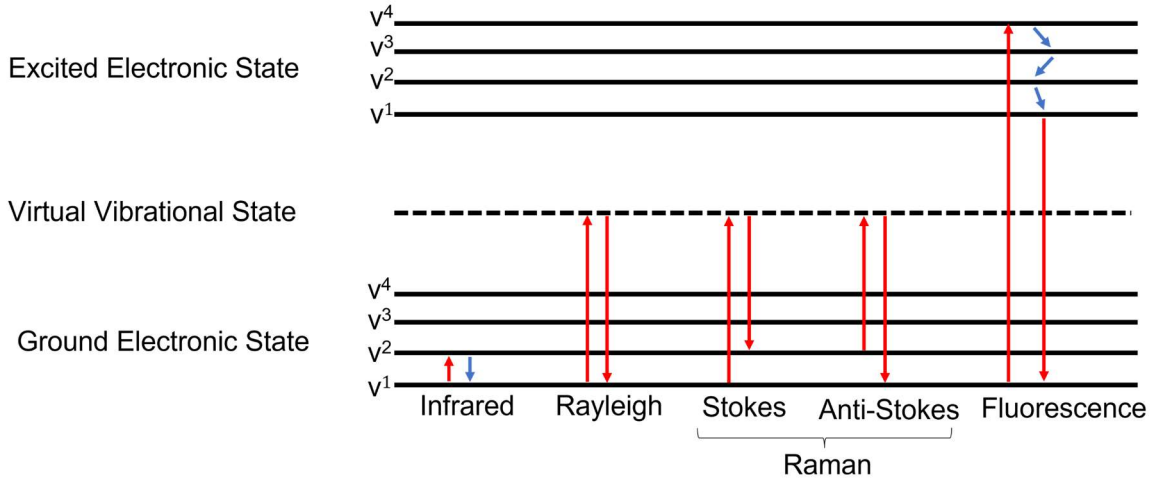

Figure 1.7: *Simplified depiction of the electronic and vibrational transitions associated with various spectroscopic techniques. The arrows pointing up indicate absorption/excitation, while the blue and red arrows pointing down indicate vibrational relaxation and radiative emission, respectively. The dotted line indicates a virtual vibrational state that does not have a consistent energy-it varies depending on the incident wavelength and is not resonant with a specific vibrational state. Adapted from* [93, 95].

These vibrational spectroscopic techniques can be coupled with conventional microscopy to enable chemical mapping of a wide variety of samples. Raman microscopy and infrared microscopy have been used in biological applications to study brain micro-haemorrhages [144, 145], protein aggregation in amyloid β plaques [146-149], cholesterol in brain tumours [150], and lipids and proteins in tissue damaged after stroke or traumatic brain injury to provide some examples [110, 144, 151, 152]. As stated previously, the techniques are complementary with some molecular vibrations exclusively Raman active, some exclusively IR active, and others detectable across both techniques. Additionally, benchtop IR microscopy tends to have a lower spatial resolution compared to Raman microscopy because the spatial resolution is proportional to the wavelength according to the Rayleigh criterion (spatial resolution = $\frac{0.61\lambda}{nsin\theta}$ [153]). Since Raman spectroscopy tends to utilise shorter excitation wavelengths in the visible region, it has improved diffraction limited spatial resolution compared to IR. This means that benchtop IR microscopy can provide information on the chemical changes occurring in a broad region, and Raman microscopy can be used to localise these changes more accurately.

For example, benchtop IR microscopy can be used to identify whether there are chemical changes occurring in a certain brain region, and Raman microscopy can then be used to identify whether these changes can be attributed to cellular alterations.

While IR microscopy is typically associated with poorer spatial resolution, it is still possible to achieve cellular and subcellular resolution using a synchrotron source [154, 155]. The synchrotron source itself does not provide the improved resolution, but rather the high photon density of synchrotron light enables the best possible diffraction limited resolution (≈3-8 μm for the ANSTO-Australian Synchrotron) with acceptable signal to noise levels, to be achieved in a reasonable experimental time frame [154, 156].

1.7.2 Theory Behind Immunohistochemistry

Immunohistochemistry is an important tool in the biomedical sciences that uses antibodies to detect antigens of interest. It can be used to identify specific cell types or subcellular organelles if antigens are specific to those regions, and it can show how the antigens are distributed throughout the tissue. The technique can be applied to multiple tissue types and has been used in disease diagnostics. Immunohistochemistry is a broad term that encompasses immunoassays and immunofluorescence staining. For immunofluorescence staining, a primary antibody specific for the antigen of interest will selectively bind to the antigen [157]. A secondary antibody with a conjugated fluorophore then selectively binds to the primary antibody [157]. When the sample is irradiated with a wavelength of light within the absorption band of the fluorophore, fluorescence emission occurs and fluorescence images showing the distribution of the antigen of interest can be collected. It is also possible to have conjugated primary and secondary antibodies which essentially minimises the number of steps required for staining. Immunoassays follow the same basic principle but are generally carried out in well plates rather than on tissue sections [158]. A diagram demonstrating the process is shown in Figure 1.8. Prior to the addition of primary antibodies, tissue is generally immersion fixed and a blocking step is completed. The purpose of the blocking step is to minimise any non-specific binding when the antibodies are added.

There are a significant number of antigens that can be stained for, but the antigens of interest for this study included GFAP, 4',6-diamidino-2-phenylindole (DAPI), and microtubule-associated protein (MAP2). These localise to astrocytes, cell nuclei, and cell cytoplasm, respectively.

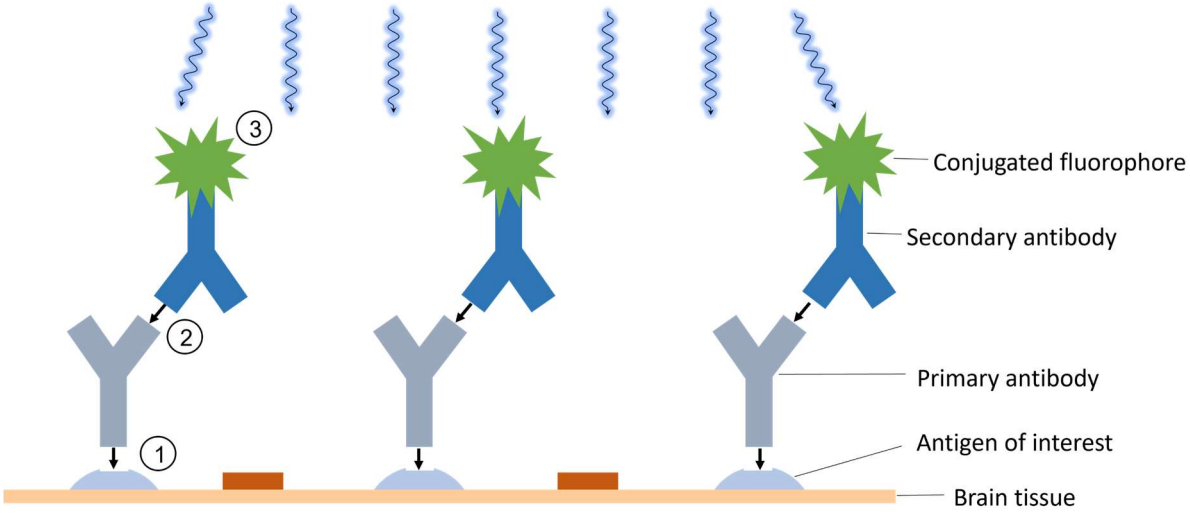

Figure 1.8: *Representation of the process that enables immunofluorescence staining. In this example, a primary antibody specific for the antigen of interest will selectively bind to the antigen on the tissue (1). A secondary antibody with a conjugated fluorophore will then selectively bind to the primary antibody (2). When the sample is irradiated with light in the excitation band of the fluorophore, fluorescence will occur enabling the distribution of the antigen to be detected (3). By using fluorophores with different excitation and emission properties, it is possible to stain for multiple antigens simultaneously. It is also possible to use conjugated antibodies which minimises the number of steps required. Despite differences in specific experimental design, immunohistochemistry and immunoassays rely on selective antigen-antibody binding as indicated in the figure.*

1.8 Animal Models

A common method for studying biological processes and diseases is to use pre-clinical animal models. There are a wide variety of models available for studying health and disease, and rodent models such as mice and rats are common due to the biological similarities they share with humans, and the ability to generate strains with mutations that represent particular disease states [159]. Genetically modified or transgenic mouse models are routinely used for studying neurodegenerative diseases such as AD [160]. Often these models are designed to study particular hallmarks or features characteristic to the diseases, such as the APP23 model that over expresses human amyloid precursor protein leading to significant formation of plaques [161, 162]. While these models are instrumental in expanding understanding of these biomarkers and what their specific role might be in disease onset, they are limited in their ability to provide insights into biochemical changes that occur during natural ageing in the absence of these hallmarks. Considering that this study was focussed towards developing methods to better understand the role of metals during natural ageing, these more commonly used transgenic models for studying neurodegeneration were not suitable.

The senescence accelerated mouse is a model that originated from accidental outbreeding of the AKR/J mouse strain and an unidentified second strain [163, 164]. Takeda et al observed that certain litters of AKR/J strain were exhibiting unexpected features, including but not limited to, hair loss, skin coarseness, exhaustion, and early death, with these phenotypes also observable in subsequent generations [163]. A senescence prone series was developed from litters with the most severe exhaustion, while a senescence resistant series was developed from litters that exhibited normal ageing [163]. These series are now referred to as senescence accelerated mouse prone (SAMP) and senescence accelerated mouse resistant (SAMR), respectively [163]. The former has 9 main sub-strains and acts as the disease model, while the latter has 3 main sub-strains and is generally utilised as the control [163]. Each sub-strain has slightly varied phenotypic traits meaning they can be applied in slightly different studies.

The SAMP8 sub-strain displays accelerated ageing and age-dependent deficits in learning and memory and has become accepted as a model to study cognitive decline during ageing and AD [165, 166]. The accelerated senescence can allow for more practical analysis time frames and was particularly suitable for this study given that phenotypic ageing changes do not appear to coincide with the cognitive deficits. They do still exhibit some characteristic features of AD,

including reports of age-dependent formation of amyloid β deposits [164], however, unlike many other models, this does not occur due to deliberate overexpression of genes meaning it might be a more suitable model for studying the more prevalent late-onset sporadic AD cases [166]. In addition to memory deficits and amyloid β deposits, these mice also appear to have a more permeable BBB [167, 168], an impaired immune system [164], and heightened anxiety [164]. While these additional features cannot be ignored when interpreting results and care should be taken if attributing observations specifically to ageing processes, the model has been widely accepted in the field and was well suited for this study that focussed primarily on method development and preliminary investigations into metal homeostasis during the ageing process.

1.9 Formal Statement of Aims and Chapters

The overall aim of this thesis was to develop and apply methods to image metal dyshomeostasis and altered brain biochemistry during ageing. This included the development of methods to image Zn speciation in brain tissue (Aim 1), application of spectroscopic techniques to probe markers of oxidative stress in Cu enriched regions of the lateral ventricles (SVZ) (Aim 2), and the coupling of spectroscopic techniques with immunohistochemistry on the same tissue section (Aim 3). The content of each of the results chapters is outlined briefly below.

Chapter 3 (Aim 1): This chapter will discuss the development of the Zn XANES reference library and its use in identifying the most abundant chemical forms of Zn in bulk frozen tissue from the hippocampus and cerebellum. The method development required careful consideration of sample preparation protocols to ensure the *in vivo* Zn environment was maintained. Therefore, this chapter will also address factors that may influence speciation including the use of glassing agents for XAS experiments, and the tissue section environment (air dried compared to frozen sections) which is particularly important for chemically specific XFM (XANES imaging). A protocol for Zn XANES imaging will be described along with its application to the SAMP8 model where XANES images were collected from young and old mice. It will discuss changes in speciation between sub-regions of the hippocampus and between the two age groups, with future improvements to the experiment also suggested.

Chapter 4 (Aim 2): This chapter will describe the application of spectroscopic methods to identify whether age-related Cu accumulation in the SVZ induces an elevation in oxidative stress markers. Specifically, it will address the XANES analysis of disulfides, and the FTIR analysis of protein aggregates and lipid peroxidation markers in SAMP8 tissue sections of two age groups. These results will also be compared with analysis of the same oxidative stress markers for brain homogenates with and without addition of a Cu solution, to further probe the underlying biochemistry.

Chapter 5 (Aim 3): This chapter will describe the capability of coupling spectroscopic imaging with immunohistochemistry on the same tissue section. The ability to combine Raman microscopy, and X-ray fluorescence microscopy, with immunohistochemical staining will be demonstrated, along with the impact of X-ray beam damage on immunofluorescence. The

development of these protocols also included an investigation into the tissue autofluorescence over time post-sectioning, the results of which will also be addressed.

Overall, development and application of the multi-modal methods and protocols described in this thesis to study altered metal homeostasis and concomitant biochemical alterations will hopefully help to reveal underlying mechanisms contributing to cognitive decline during ageing. This in turn may reveal pathways for slowing cognitive decline, or preventing and treating neurodegenerative diseases such as AD.

Chapter 2: Methods

ABSTRACT

This chapter will outline experimental procedures relevant to each of the following results and discussion chapters (Chapter 3, 4, and 5). These details include sample preparation, data collection, data processing and analysis, and statistical analysis. Each section of this chapter (2.1, 2.2, 2.3) will address the methods utilised for a certain results chapter. Specifically, section 2.1 outlines the methods used for chapter 3, section 2.2 outlines the methods used for chapter 4, and section 2.3 outlines the methods used for chapter 5.

2.1 Methods-Chapter 3

2.1.1 Brain Sample Preparation

2.1.1.1 Animal Models

To minimise the number of animal deaths, this research has used excess archived tissue from previous studies, which were conducted in accordance with Curtin University Animal Ethics Guidelines. Rat tissue (n = 4) from 6 month old male Sprague Dawley rats was used for bulk XANES analysis to compare Zn speciation in the cerebellum and hippocampus. Murine tissue from male 5 (5m) and 12 (12m) month old senescence accelerated mouse prone strain 8 (SAMP8) mice (n = 3 in each age group) was used for micro-XANES analysis, to investigate Zn speciation within the hippocampus. All animals were housed in standard cages in a temperature controlled (21 °C) colony room with 12 hr light/dark cycle, with access to food and water *ad libitum* (standard rodent maintenance chow) [20, 169, 170]. Due to species variation there may be subtle differences in the chemical form of Zn between the bulk XANES and micro-XANES experiments. The major outcomes of the study should not have been affected however, as the labile Zn pool in the hippocampus is highly conserved across mice and rats [83, 89].

2.1.1.2 Tissue Preparation

To preserve the *in vivo* Zn speciation as close as possible to the *in vivo* condition, animals were anaesthetized with pentobarbital (45 mg/kg) (mice) or isoflurane (rats), humanely sacrificed, and the brain tissue rapidly dissected into sagittal hemispheres and plunge frozen in liquid nitrogen cooled isopentane [170-172].

2.1.1.2.1 Bulk XANES Analysis (XAS)

For rat tissue, 1 mm cubes of hippocampus and cerebellum tissue were dissected on dry ice. Samples were obtained 6 months prior to XANES measurements and stored at – 80 °C until required for analysis (for both mouse and rat brain tissue).

2.1.1.2.2 Micro-XANES of Air Dried Tissue (XFM)

For mouse brain tissue sections, one week before XANES analysis, 10-µm-thick coronal brain sections were cut from the frozen tissue blocks with a cryo-microtome at -16 to - 18 °C and melted onto a silicon nitride substrate (Melbourne Centre for Nanofabrication, 10 × 10 mm^2 200 µm thick silicon frame, and a 5 × 5 mm^2 1000 nm thick silicon nitride membrane). Tissue sections were air dried and stored in the dark with desiccant until micro-XANES analysis. All micro-XANES analyses were performed within 7 days of tissue sectioning.

2.1.1.2.3 Cryo-Micro-XANES of Frozen Tissue (XFM)

Similarly to the air dried sections, one week before XANES analysis, 14-µm-thick coronal mouse brain sections were cut from the frozen tissue blocks with a cryo-microtome at -16 to - 18 °C and melted onto a silicon nitride substrate (Melbourne Centre for Nanofabrication, 10 × 10 mm^2 200 µm thick silicon frame, and a 5 × 5 mm^2 1000 nm thick silicon nitride membrane). Samples were stored at -80°C until transport to the ANSTO-Australian synchrotron facility on dry ice.

2.1.2 XANES Analysis

2.1.2.1 Standard Solutions

A stock solution of zinc nitrate (1 mM) was prepared by dissolving zinc nitrate hexahydrate ($Zn(NO_3)_2.6H_2O$, 0.018 g) in reverse osmosis water (50 mL). This stock solution served to model the Zn^{2+} hexaaqua complex and was also used as the source of Zn^{2+} for the preparation of additional standard solutions. The additional standard solutions were prepared such that the ligands had a concentration of approximately 10 mM. To test what effect the presence of chloride ligands had on the coordination of the Zn atom, excess NaCl (0.018 g, 100 mM) was dissolved in each standard solution (3 mL). Standard solutions of Zn^{2+} in H_2O at pH 2 and pH 13 were also prepared, through the addition of HNO_3 and NaOH, respectively. The basic solution appeared cloudy upon initial addition of NaOH due to formation of $Zn(OH)_{2(s)}$, however the solution returned to colourless upon addition of excess OH^- (i.e. at pH 13). This is expected as $Zn(OH)_2$ is highly soluble at high pH, owing to the formation of the $Zn(OH)_4^{2-}$ complex. Dynamic light scattering was performed, using a *Malvern Zetasizer Nano ZS,* to confirm the absence of particulates in the final standard solution at pH 13 (Figure 2.1).

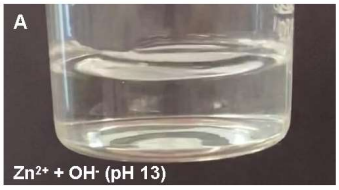

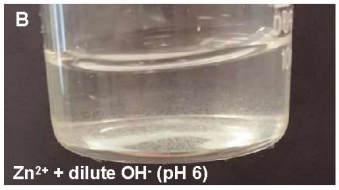

C

Results from Dynamic Light Scattering

	Derived Count Rate (kilo counts per second or kcps)	
	Zinc nitrate hexahydrate (1mM)	Zinc nitrate hexahydrate (1mM) + 1 pellet NaOH
Replicate 1	88	40
Replicate 2	75	39
Average	81.5	39.5

Figure 2.1*: Visible appearance of Zn^{2+} standard solutions after (A) the addition of concentrated OH^- as undertaken for the synchrotron experiment, or (B) dilute OH^-. The latter shows the appearance of a white precipitate attributed to $Zn(OH_2)_{(s)}$, which is known to have low solubility at a neutral pH. Dynamic light scattering, DLS (C) did not indicate increased presence of particles in standard solution A, relative to the Zn^{2+} (zinc nitrate hexahydrate) solution. DLS measurements were recorded on a Malvern Zetasizer Nano ZS.*

In addition to the standard solutions described in Table 2.1, a solution that was a mixture of histidine and cysteine was prepared by combining equal amounts (750 μL) of each solution. To test the effect of glassing agents, glycerol was combined with the cysteine and histidine solutions (separately) in a 1:2 ratio (i.e. 1 mL glycerol and 2 mL of standard solution). Further sample details are shown in Table 2.1.

Table 2.1 *Details for preparation of Zn^{2+} Standard Solutions for XANES Analysis. Concentrations (Conc) are rounded to the nearest mM and will be lower than indicated for samples containing glassing agents.*

Ligand	**Ligand Compound**	**Mass (g)**	**Final Volume (mL)**	**Ligand Conc (mM)**	**$Zn^{2+}_{(aq)}$ Conc (mM)**	**Glassing Agent (Y/N)**
Cysteine	L-cysteine	0.006	5	10	1	N
Cysteine	L-cysteine	0.006	5	10	1	Y
Histidine	L-histidine	0.020	10	13	1	N
Histidine	L-histidine	0.020	10	13	1	Y
Glutamate	L-glutamic acid monosodium salt monohydrate	0.011	5	12	1	N
Citrate	Tri-sodium citrate dihydrate	0.015	5	10	1	N
EDTA	Ethylenediamine tetra acetic acid di-sodium salt dihydrate	0.018	5	10	1	N
PO_4^{3-}	Di-sodium hydrogen phosphate	0.008	5	11	1	N
Cl^-	Sodium Chloride	0.018	3	103	1	N
Cysteine + Cl^-	Sodium chloride (dissolved in 10 mM cysteine solution)	0.018	3	103	1	N
Histidine + Cl^-	Sodium chloride (dissolved in 13 mM histidine solution)	0.018	3	103	1	N

Aqueous standard solutions were injected into liquid sample holders (Kapton window) and rapidly frozen by submerging in liquid nitrogen cooled isopentane. Tissue samples were mounted in the same holders. Tissue samples were not observed to thaw during sample mounting (sample mounting times were < 1 minute).

2.1.2.2 Collection of Bulk XANES Spectra – Data Acquisition.

All Zn K-edge XAS data was collected at the ANSTO-Australian Synchrotron, using the X-ray Absorption Spectroscopy beamline equipped with a 1.9T wiggler and Si(111) double crystal monochromator (DCM). The DCM was operated at the top of the rocking curve ("fully tuned") and harmonics were rejected using mirrors (Si, Rh), which were also used to focus the beam. The beam spot size at the sample was of approximately 1 x 0.5 mm^2, and the incoming beam intensity was measured using an ion chamber ("I0"; N_2 flow at 0.3 L/min; U=2.1kV). All samples (model compounds and micro-dissected tissues) were mounted with the detector facing surface at 45° to the incident X-ray beam, in a liquid Helium cooled cryostat (measurements were recorded at ~12-15 K). The XANES spectra were recorded through collection of K_α fluorescence emission, recorded using a Canberra liquid nitrogen cooled 100-pixel monolithic solid state Ge detector. X-ray absorption spectra were calibrated against the absorption spectrum of Zn metallic foil, calibrated to first inflection peak at 9660.7 eV. The calibration spectra were recorded simultaneously with sample spectra, in transmission geometry with ion chambers ("I1" and "I2"; N_2 flow at 0.3 L/min; U=2.1kV). The XANES spectra were recorded across the K-edge white line features 9650 – 9700 eV at 0.3 eV steps, with a dwell time of 500 ms per data point. Additional data points were collected above and below the edge such that the full spectral range was 9600 – 9900 eV, to assist background subtraction (also 500 ms dwell). Specific step sizes for each spectral region are outlined in table 2.2.

Table 2.2: *Parameters for XANES scans using the XAS beamline at the ANSTO-Australian Synchrotron*

Spectral Region	Start Energy (keV)	End Energy (keV)	Energy Step Size (keV)	Dwell Time (s)	Number of Points
1	9.6	9.65	0.005	0.5	11
2	9.65	9.7	0.0003	0.5	167
3	9.7	8k	0.07k (linear)	1	68

EXAFS region of spectrum is described using "k-space" which is what k refers to in 3rd row

Initial data pre-processing was performed using in-house developed Sakura software v2.7[173], to exclude data from detector pixels containing contributions from ice diffractions. Data was then exported in ASCI format and further analysed using EXAFSPAK [174]. Normalised white line intensities are reported to 3 significant figures (2 decimal places), on the basis that 3σ of the noise level = 0.005 absorbance units (calculated from the baseline-corrected pre-edge, in normalised spectra).

2.1.2.3 Collection of Micro-XANES Spectra – Synchrotron X-ray Fluorescence Microscopy

Micro-XANES spectra were collected at the X-ray Fluorescence Microscopy beamline at the ANSTO-Australian Synchrotron [175]. A "XANES-stack" of X-ray fluorescence elemental maps, similar to previously described [118, 119, 126], were collected for 125 incident energies (air dried tissue) or 98 incident energies (frozen tissue) that correspond to the energies indicated in table 2.3.

Table 2.3: *Incident energies for the collection of micro-XANES images in air dried and frozen tissue sections*

	Air dried tissue	Frozen tissue
Pre-edge region (5 eV steps)	9630-9650 eV	9630-9650 eV
White line region (0.5 eV steps)	9650-9699 eV	9650-9685 eV
Post-edge (2 eV steps)	9699-9723 eV	9685-9713 eV
Post-edge (10 eV steps)	9723-9803 eV	9713-9803 eV

Images were collected starting at the highest energy (9803 eV) and then collected at successively lower incident energies due to details of the operation of the in-vacuum undulator. Most elemental maps were collected from regions of the hippocampus that contained the mossy fibres, however, some larger maps containing the whole hippocampus were also collected (the location was identified using an optical microscope mounted at the

beamline). Similar to the bulk XANES measurements, energy calibration was performed with a metallic Zn foil mounted downstream of the sample. The absorbance spectrum of the calibration foil was collected in transmission geometry with N_2 gas-filled ion chambers. A comparison of the XANES spectra collected from the calibration Zn metal foil on both the XAS and XFM beamline, are presented in Figure 2.2.

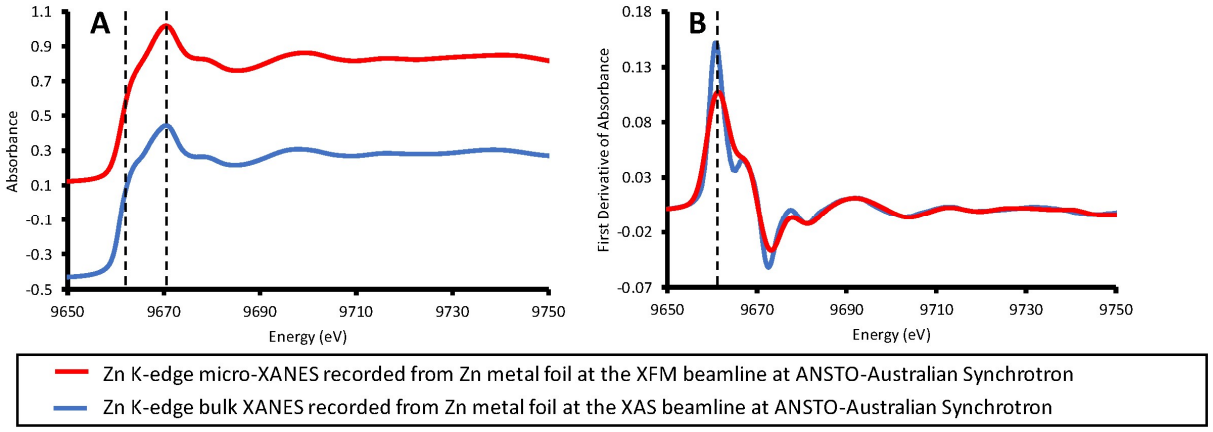

***Figure 2.2**: Zn K-edge XANES recorded from Zn metal energy calibration foils at the XFM and XAS beamlines at the ANSTO-Australian Synchrotron. Panel A shows the raw spectra while panel B shows the first derivative spectra.*

With the exception of the successively decreasing incident energy, the process of collecting elemental maps from air dried tissue was similar to methods that have been previously described [20, 176, 177], in brief: The X-ray beam was focused to a ~1 µm (1-sigma) spot with a Kirkpatrick–Baez mirror pair and X-ray emissions from the sample were collected in event-mode using the low-latency, 384-pixel Maia detector [178]. Data were collected with the sample oriented normal to the incident beam and with the detector positioned in backscatter geometry. The sample was raster scanned through the beam with an effective dwell time of 1 ms per effective step size (image pixel) of 1 μm (1.5 ms dwell time and 3 μM step size for whole hippocampus map).

To minimise dehydration (air drying) induced alterations to Zn^{2+} speciation, frozen tissue sections were imaged under a cryostream of nitrogen vapour at -40 $°C$ (measured with thermocouple). Similarly to the air dried tissue analysis the X-ray beam was focused to a ~1 µm (1-sigma) spot with a Kirkpatrick–Baez mirror pair and X-ray emissions from the sample were collected using an FX5 vortex detector. The tissue was scanned once at 9803eV, with a 4 μm step size and 2 or 4 millisecond dwell time to locate the regions of interest. The sample

was then raster scanned through the beam at each energy with an effective dwell time between 1 and 4 ms per effective step size (image pixel) of 2 μm.

Air dried and frozen tissue elemental maps were reconstructed from the full emission spectra with GeoPIXE v6.6j (CSIRO, Australia), using a linear transformation matrix for spectral deconvolution. Elemental maps of Zn fluorescence intensity were extracted as TIFF files which were then imported into ImageJ where regions of interest were drawn around the CA3 mossy fibres (Zn rich) and the CA3 pyramidal cells (moderate Zn, and Fe rich cells). The average Zn fluorescence was determined for each of the two regions of interest, for each of the Zn maps collected at the energies across the Zn edge. A plot of Zn fluorescence intensity as a function of the incident energy used to collect the elemental map revealed the average micro-XANES spectrum for the region of interest (this is achieved in ImageJ using a "plot Z profile" function). The micro-XANES spectra were exported from ImageJ as ASCI files for further analysis in EXAFSPAK.

2.1.2.4 Bulk and Micro-XANES Data Analysis

EXAFSPAK was used for XANES data analysis. Spectra were background corrected (polynomial background subtraction, calculated from pre-edge region (9600-9650 for bulk XANES, or 9630-9650 for micro-XANES)) and normalised to a post-edge jump of 1 absorbance unit at 9750 eV. DATFIT, within EXAFSPAK, was used to fit XANES spectra of brain tissue (both bulk and micro-XANES) to linear combinations of the bulk spectra of standard solutions. Standard solution spectra were excluded from the refinements algorithm if they contributed to less than 0.5% of the total spectra.

Micro-XANES maps were generated using MANTiS (Multivariate ANalysis Tool for Spectromicroscopy) software, using inbuilt single value decomposition and standard solution spectra to generate chemically specific images of Zn^{2+} speciation.

2.1.3 Statistical Analysis

Statistical analyses were performed using Graphpad Prism, and all data is presented as scatter plots. Testing for differences in Zn speciation between the cerebellum and hippocampus in rat tissue (n = 4 replicates) was performed using a Student's t-test and 95 % confidence interval (cerebellum and hippocampus tissue was not paired from the same animal). Testing for differences in Zn speciation between the mossy fibres and pyramidal cells of 12m murine hippocampus (n = 3 replicates) was undertaken using a two-way ANOVA with multiple

comparison testing. Similarly, comparison of Zn speciation between 5m and 12m mossy fibres was undertaken using a two-way ANOVA with multiple comparison testing.

2.2 Methods-Chapter 4

2.2.1 Animal Model and Sample Preparation

2.2.1.1 Animal Models

To minimise the number of animal deaths, this study used excess archived tissue from previous studies, which were conducted in accordance with Curtin University Animal Ethics Guidelines. Specifically, senescence accelerated mouse prone 8 (SAMP8) samples were used for this study, with mice aged 5 months (5m, n = 6) and 12 months (12m, n = 6). Mice were housed in standard cages in a temperature controlled (21 °C) colony room with 12 hr light/dark cycle, with access to food and water *ad libitum* (standard rodent maintenance chow) [20, 169, 170]. Mice were humanely sacrificed under anaesthesia with pentobarbital (45 mg/kg), then tissue was rapidly frozen in liquid nitrogen cooled isopentane and stored at -80 °C. Additional brain tissue was sourced from excess wildtype mouse brains (C57Bl/6) for preparation of brain homogenates, described in section 2.2.1.2.

2.2.1.1 Tissue Sections

Tissue was embedded in optimal cutting temperature medium and sections (10 µm thick) were cut at -16 °C using a cryo-microtome and air dried onto calcium fluoride (CaF_2) discs for FTIR analysis, and metal free plastic thermanox coverslips for XANES analysis.

2.2.1.2 Brain Homogenates

Brain homogenates from ≈40 mg pieces of tissue were collected from wild-type mouse brains (n=5) and then homogenised. Specifically, 800 μL of mammalian lysis buffer was added to each sample and they were homogenised using a Kimble Dounce tissue grinder (2 mL) with 10 passes using pestle A (0.003-0.005 inch clearance) and 5 passes using pestle B (0.0005-0.0025 inch clearance). Samples were centrifuged at 4°C for 15 minutes at 14 000 rounds per minute (rpm), then the supernatant was collected into three separate aliquots (207 μL each) for each sample. Each aliquot had either phosphate buffered saline (PBS), or varying amounts of a copper sulfate solution ($CuSO_4 \cdot 5H_2O$, 10 mM, dissolved in PBS) added to obtain a total volume of 250 μL. The specific details of each aliquot is outlined in table 2.4. This process was repeated for all 5 samples. A 50 μL aliquot was then collected from each 250 μL aliquot and frozen at -80 °C until ATR-FTIR analysis (section 2.2.3.2). The remaining 200 μL was deproteinised for analysis using a glutathione detection assay (section 2.2.4).

Table 2.4: *Details of the preparation of each aliquot from the supernatant of a brain homogenate sample. This was repeated for all 5 samples resulting in 15 total aliquots: one without additional Cu, and two with Cu at varying concentrations for each sample.*

	Aliquot A	**Aliquot B**	**Aliquot C**
Solution added to supernatant	PBS	$CuSO_4$ Solution (10 mM) and PBS	$CuSO_4$ Solution (10 mM)
Volume	42.4 μL	7.5 μL ($CuSO_4$ solution) and 35 μL (PBS)	42.4 μL
Final Cu concentration	0 mM	3 mM	17 mM

2.2.2 Collection of Micro-XANES Spectra and XANES Images

All S K-edge XAS data were collected at the Stanford Synchrotron Radiation Lightsource, using the 14-3b (X-ray Absorption Spectroscopy) beamline equipped with a bending magnet and Si(111) double crystal monochromator. All samples were mounted at 45° to the incident X-ray beam, in an ambient temperature helium environment, and the beam spot size was micro-focussed to 7 μm (1-sigma) using a Kirkpatrick-Baez mirror system. The XANES spectra were recorded through collection of K_α fluorescence emission using a vortex 4-element silicon drift detector positioned 90° to the incident X-rays. X-ray absorption spectra were calibrated against the absorption spectrum of sodium thiosulfate ($Na_2S_2O_3 \cdot 5H_2O$) powder (calibrated to lowest energy peak at 2469.2 eV) [103, 117]. The micro-XANES spectra were recorded across the K-edge white line features 2460 – 2500 eV from regions of interest along the medial and lateral walls of the ventricles (subventricular zone), with a dwell time of 500 ms per data point and a 0.2 eV step size. Additional data points were collected above the edge at 2 eV steps, such that the full spectral range was 2460 – 2536 eV (also 500 ms dwell). Data collection of XANES spectra at the beamline was performed using in house software, while post-processing including pre-edge subtraction, normalising, and least squares fitting was completed using EXAFSPAK. S XANES spectra from the SAMP8 lateral ventricles were fitted to biologically relevant S XANES spectra that had been previously collected by Hackett et al [103, 117]. Statistical analysis was completed using Graphpad Prism and included two-way ANOVAs with multiple comparison testing to compare the relative concentration of the S compounds between the two time points for both the medial and lateral sides of the ventricle. Given that the results were consistent across the medial and lateral sides, only the medial data will be presented.

Comparisons were completed using either the results from a single spectrum (if only one was collected from the sample), or from the average of multiple (if multiple spectra were collected from one sample). For the medial walls of the ventricles, there was n=5 5m samples, and n=6 12m samples.

For the chemically specific XANES images, the X-ray beam was mapped across the samples with a step size of 10 μm and a dwell time of 500 ms. Incident energies of 2469.85 eV, 2470.55 eV, 2470.80 eV, 2473.50 eV, 2478.20 eV, and 2479.80 eV were used to represent disulfides, thiols, thioethers, sulfoxides, sulfonic acids, and O-linked sulfate esters, respectively [103]. Smak and ImageJ software was used for XANES image analysis and a Student's t-test with a 95% confidence interval in Graphpad Prism was used to compare the disulfide fluorescence intensity from regions of interest along the walls of the lateral ventricles (defined using ImageJ, example in Figure 2.3) between time points. There were n=3 images for each time point.

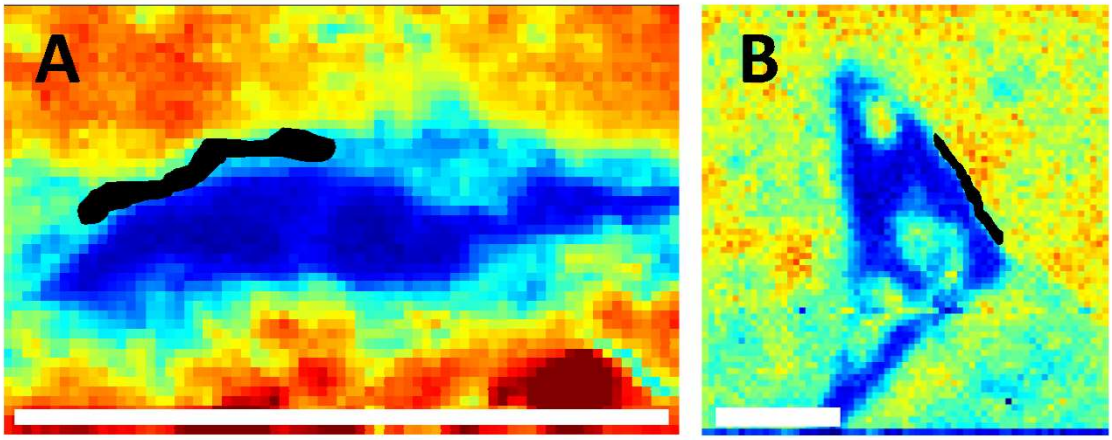

***Figure 2.3**: A) Representative region of interest drawn on a false colour FTIR image generated from the CH stretching region (2840-2865 cm^{-1}). B) Representative region of interest drawn on a false colour XANES image of disulfides. Regions of interest are indicated in black.*
Scale bars = 200 µm.

2.2.3 Fourier Transform Infrared Spectroscopy

2.2.3.1 Synchrotron FTIR Microscopy

All FTIR data collection was completed at the ANSTO-Australian Synchrotron using the infrared microspectroscopy beamline. Images of a small portion of the ventricles were collected in transmission mode using a Bruker Vertex 80v FTIR spectrometer. Specific details of the instrumental set up and scan parameters are detailed in table 2.5. The background spectra were collected with 4 cm^{-1} spectral resolution and 32 scans.

Table 2.5: *Instrument and scan parameters for synchrotron FTIR microspectoscopy of brain ventricles*

Aperture	5.6 µm
Objective	36x
Spectral Resolution	4 cm^{-1}
Number of Scans	8 scans
Step Size	3 µm
Condenser Offset	30
Detector	Liquid nitrogen cooled mercury cadmium telluride (MCT)

2.2.3.2 Benchtop ATR-FTIR

A Thermo Scientific Nicolet iS50 ATR instrument with a diamond crystal and a deuterated triglycine sulfate (DTGS) detector was utilised for FTIR analysis of the brain homogenates. 256 scans with 4 cm^{-1} resolution were collected for both sample and background spectra. To minimise the contribution of water to the sample spectra, samples were dropped onto the ATR crystal then left to dry prior to spectral collection.

2.2.3.3 FTIR Data Analysis

Regions of interest from the synchrotron FTIR images were generated using CytoSpec 2.00.03 with targeted regions localised to the walls of the ventricles as indicated in figure 2.3. OPUS 7.0 was used for spectral processing of both synchrotron and benchtop FTIR data. Spectra were vector normalised to the amide I band (1600-1700 cm^{-1}) and the integrated area under the curve (IAUC) was measured for key peaks of interest. Additionally, second derivatives of the normalised spectra were generated using a 13-smoothing point Savitzky−Golay function. The integration ranges for the normalised spectra and the wavenumbers of interest for the

second derivative spectra are indicated in table 2.6. Statistical analysis was completed using Graphpad Prism and included Student's t-tests with a 95% confidence interval to compare the integration and intensity values between the 5m and 12m samples. A one-way ANOVA with multiple comparison testing was used to statistically compare differences between the brain homogenates with varying Cu concentrations.

Table 2.6: *IR peak integration ranges and corresponding peak assignments*

Marker of Interest	**Integration Range**	**Second Derivative Intensity**
Unsaturated Lipids (Olefinic CH)	3000-3025 cm^{-1}	3012 cm^{-1}
Aldehydes (Carbonyl stretching)	1710-1755 cm^{-1}	1715 cm^{-1}
Proteins (Amide I band)	1600-1700 cm^{-1}	1655 cm^{-1} (α-helices) 1627 cm^{-1} (β-sheets)

2.2.4 Glutathione Detection Assay

The remaining 200 μL for each brain homogenate aliquot (A, B, and C for each sample) was deproteinised prior to assay detection (see section 2.2.1.2 for details on brain homogenate preparation). Trichloroacetic acid (TCA, 20 μL) was added to each aliquot and they were incubated on ice for 15 minutes. Samples were then centrifuged at 4°C for 5 minutes at 12 000 rpm, and the supernatant was collected. If samples appeared cloudy, the centrifugation step was repeated until the sample was mostly clear. The supernatant volume varied slightly with each sample but was ≈180 μL. Samples were frozen at -80°C overnight, prior to assay detection. After samples were defrosted, they were centrifuged at 4°C for 5 minutes at 12 000 rpm, then the neutralisation solution ($NaHCO_3$, 13 μL) was added to the supernatant.

An abcam glutathione/disulfide (GSH/GSSG) ratio detection assay kit II (ab205811) was used for the analysis of disulfides in the brain homogenates. A number of GSH and GSSG standards were prepared according to the protocol and were measured in duplicate. Samples were also measured in duplicate and were diluted by a factor of 10 prior to detection. Each well was prepared according to the protocol and contained 50 μL of sample or standard, and 50 μL of either the GSH assay mixture (GAM) or the total GSH assay mixture (TGAM) depending on the target analyte for each specific well. After addition of the assay mixture, they were incubated

in the dark at room temperature for ≈15 minutes. Fluorescence values for each well were recorded using an EnSight Multimode plate reader.

To determine the oxidised glutathione content, thiols were assayed before and after addition of Cu^{2+}, with the difference ($thiol_{after}$ – $thiol_{before}$) taken to represent the net amount of oxidised thiols. The net amount of oxidised thiols, divided by 2, was used as the oxidised glutathione value. The concentration of glutathione was calculated from the line of best fit of the standards ($\log(y) = mlog(x) + c$) where the concentration was x and the fluorescence intensity was y. The standard plot is shown in Figure 2.4. The % decrease in glutathione relative to the control was then calculated and divided by two to determine the % increase in disulfides (1:2 disulfide to glutathione ratio).

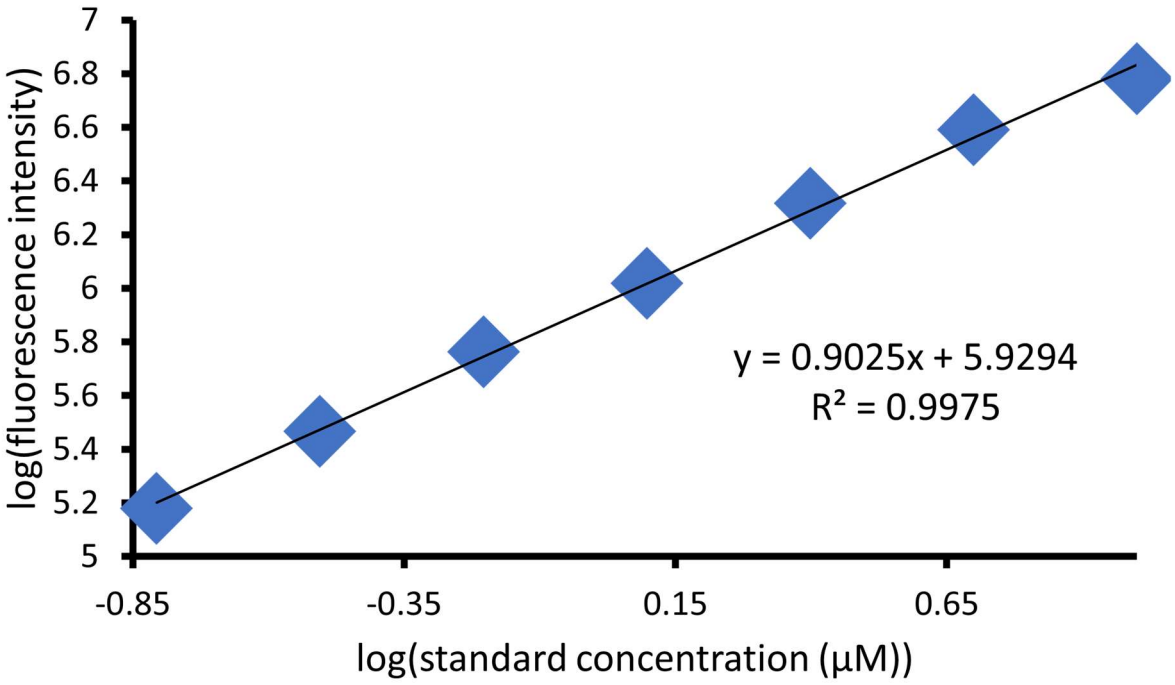

***Figure 2.4**: Plot of the log of concentration against the log of fluorescence of the glutathione standards measured by the glutathione detection assay. The equation for the line of best fit was used to calculate the concentration of glutathione in the brain homogenate samples, then the percentage decrease in glutathione relative to the control was determined. It was assumed that the decrease in glutathione is a result of conversion to disulfides, so half of the percentage decrease of glutathione was equated to the percentage increase in disulfides (2:1 glutathione to disulfide ratio).*

2.3 Methods-Chapter 5

2.3.1 Animal Model and Sample Preparation

All animal tissue used in this study was excess tissue from previous studies, in which the animal work was conducted with approval from Curtin University Animal Ethics. In the previous studies and as outlined in sections 2.1.1.1 and 2.2.1.1, the rats (Sprague Dawley) and mice (senescence accelerated mouse prone 8, SAMP8) were housed in standard cages in a temperature controlled (21 °C) colony room with 12 hr light/dark cycle, with access to food and water *ad libitum* (standard rodent maintenance chow), then humanely sacrificed under anaesthesia with isoflurane (rats) or pentobarbital (45 mg/kg) (mice) [170]. Tissue was rapidly frozen in liquid nitrogen cooled isopentane and stored at -80 $°C$ until sectioning. Tissue was embedded in optimal cutting temperature medium and sections (10 µm thick) were cut at -16 $°C$ using a cryo-microtome and air dried onto glass slides. For XFM, similarly prepared tissue sections were melted onto silicon nitride windows and immediately re-frozen and stored at – 80 $°C$ until required for analysis.

2.3.2 Fluorescence Microscopy

Images of tissue autofluorescence were collected over a time course using an Olympus BX-51 upright fluorescence microscope. Three different filter cubes were utilised and to ensure an accurate comparison, the exposure times were kept consistent for each cube and can be seen in table 2.7. The images were taken on day 1, day 2, day 3, day 5 and day 9, where day 1 was the day of sectioning. Images were imported into ImageJ, where the average fluorescence intensity was determined for regions of interest corresponding to the molecular layer, granular layer, and white matter (regions indicated in Figure 2.5). These regions were then compared across time points via a repeated measures one-way ANOVA with multiple comparison testing in GraphPad Prism.

Table 2.7: *Filters and exposure times utilised to collect the time course fluorescence images*

Bandpass Excitation Filter (nm)	**Farb Teiler Beam Splitter (nm)**	**Long Pass Emission Filter (nm)**	**Exposure Time (ms)**
375/28 (Ultraviolet)	415	435	68
465/15 (Blue)	500	515	218.7
530/40 (Green)	570	590	615.3

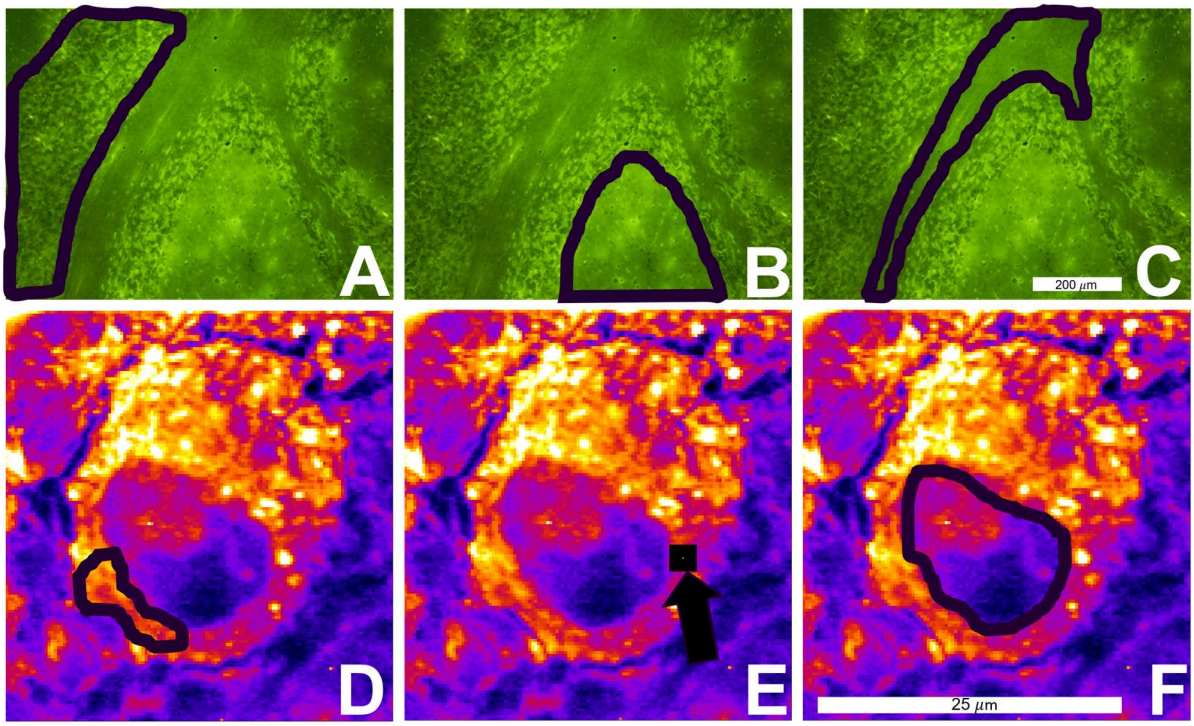

Figure 2.5: *Representative regions of interest drawn on fluorescence microscopy images (A-C) and Raman microscopy maps (D-F). Fluorescence microscopy images (blue excitation, green emission) show representative regions of interest for the: granular layer (A), molecular layer (B) and white matter (C). Raman microscopy maps show representative subcellular regions of interest for the: the cytoplasm (D), lipofuscin deposits (E) and nucleus (F).*

2.3.3 Dispersive Raman Spectroscopy

The dispersive Raman experiments were carried out using a Labram 1B dispersive Raman spectrometer fitted with a 50x objective, with 514 nm green light excitation. Six rat cerebellum sections were collected for analysis by dispersive Raman spectroscopy (treated as $n = 6$ for statistical analysis). Three spectra were collected from the molecular layer, granular layer, and white matter for every section (i.e. 9 spectra per section). This analysis was carried out the day of sectioning (day 1) and was repeated on the morning of day 2, day 3, day 5 and day 9. The three replicate spectra from each region were averaged together before spectral analysis so that there was one average spectrum from the granular layer, molecular layer, and white matter for every section at each time point. The IAUC of the autofluorescent baseline from 2000-2500 cm^{-1} was determined for the raw spectra before further statistical analysis. The IAUC was compared across time points via a repeated measures one-way ANOVA with multiple comparison testing in GraphPad Prism.

2.3.4 Confocal Raman Microscopy

2.3.4.1 Effect of Time on Tissue Autofluorescence Measured in Raman Spectra

The experiment carried out using the dispersive Raman spectrometer was repeated using a WITec Alpha 300 SAR using confocal modality and 532 nm green light excitation. Six rat cerebellum sections (n = 6) were collected for analysis and three spectra were collected from the molecular layer, granular layer and white matter for every section (i.e. 9 spectra per section). The high laser power of this instrument can cause bleaching of autofluorescence, so to prevent this from occurring prior to collection of the spectrum, a time series spectrum recording was started prior to the opening of laser shutter and finished 30 seconds later. The spectrum three pixels after the initial opening of the laser shutter was extracted and used for statistical analysis. The point at which the laser shutter opened was evident by the sudden increase in Raman signal. The analysis was carried out the day of sectioning (day 1) and repeated on the morning of day 2, 3, 5 and 9.

2.3.4.2 Confocal Raman Microscopy Imaging Parameters

Cerebellum tissue from rat brain embedded in optimal cutting temperature medium was sectioned to 10 μm thickness at -16°C and collected onto glass slides. Images of Purkinje neurons were collected at a high spatial resolution using the same WITec Alpha 300 SAR with confocal modality and 532 nm green light excitation. The pixel size was either 0.25 um or 0.5 μm depending on the image. The measurement parameters are shown in table 2.8.

Table 2.8: *Confocal Raman microscopy measurement parameters*

Integration Time	0.2 s
Pixel Size	0.25 um or 0.5 um
Slit Width	150 um
Objective	100x
Lines per mm Diffraction Grating	1800
Detector	Peltier-cooled CCD detector at -60°C
Laser Spot Size	0.3 um

2.3.4.3 Confocal Raman Microscopy Data Analysis

Raman spectra were analysed using Project FOUR WITec Suite 4.0 software and OPUS 7.0. The three replicate spectra from each region were averaged together before further spectral analysis so that there was one average spectrum from the granular layer, molecular layer, and white matter. The IAUC of the autofluorescent baseline from 2000-2500 cm^{-1} was determined for the raw spectra before further statistical analysis. The IAUC was compared across time points via a repeated measures one-way ANOVA with multiple comparison testing in GraphPad Prism.

The imaging data analysis was carried out using Project FOUR WITec Suite 4.0 software, ImageJ, and OPUS 7.0. Images were generated in Project FOUR where regions of interest were drawn, and the average spectrum of those regions extracted. It should be noted that due to the size of the lipofuscin deposits, rather than extracting an average spectrum from a drawn region, single spectra were collected from each deposit which were then averaged together after extraction. An example of the regions of interest is provided in Figure 2.5. Images for the final figures were imported into ImageJ where the false colour scale was set and adjusted. Further spectral analysis was completed in OPUS 7.0. The spectra were vector normalised from 2800-3100 cm^{-1} and smoothed with 17 smoothing points. The IAUC was compared across regions via a repeated measures one-way ANOVA with multiple comparison testing in GraphPad Prism. The integration ranges can be seen in table 2.9.

Table 2.9: *Raman peak integration ranges and corresponding peak assignments*

Wavenumber Range (cm^{-1})	**Corresponding Peak Assignment**
3035-3090	N-H Stretching (proteins)
2900-3000	CH (CH_3) stretching (Proteins/Lipids)
2830-2900	CH (CH_2) stretching (saturated lipids/protein)
1633-1692	C=C stretching (unsaturated lipids)
725-780	Pyrimidine ring breathing (DNA)

2.3.5 X-ray Fluorescence Microscopy and XANES Imaging

Frozen SAMP8 tissue was imaged using the ANSTO-Australian Synchrotron X-Ray Fluorescence Microscopy beamline as described in section 2.1.2.3. After imaging, the samples were thawed and air dried ahead of immunohistochemistry protocols.

2.3.6 Histology and Immunohistochemistry

2.3.6.1 Haematoxylin and Eosin Staining (Histology)

A routine protocol for staining with haematoxylin and eosin (H&E) was followed, as previously demonstrated [81].

2.3.6.2 Immunohistochemistry

Tissue was formalin fixed for approximately 10 minutes then rinsed and rehydrated in PBS three times for 5 minutes. The tissue was then blocked in 10% goat serum for approximately 30 minutes. The primary antibodies were added, and tissue was incubated in a moisture chamber in the fridge (≈4°C) overnight. The following day, the primary antibodies were rinsed off with PBS three times for 5 minutes. The secondary antibodies were added and incubated for 2 hours in the dark at room temperature. The secondary antibodies were rinsed off with PBS three times for 5 minutes. DAPI was applied either in the last wash, in the mounting medium, or added for 5 minutes then rinsed off with PBS before adding anti-fade mounting medium and coverslips. The diluent for the goat serum and antibodies was 0.1% bovine serum albumin in tris buffered saline (TBS) + 0.2% Tween20. The specific antibodies and concentrations can be seen in Table 2.10.

Table 2.10: *Concentration ratios of each immunofluorescent antibody and stain*

Antibody	**Concentration Ratio**
GFAP	1:200
MAP2	1:2000
Conjugated GFAP 555	1:500
DAPI	1:1000
AlexaFluor546 Goat Anti-Rabbit	1:1000
AlexaFluor488 Goat Anti-Chicken	1:1000
AlexaFluor488 Goat Anti-Rabbit	1:1000

It should be noted that the same protocol was applied to tissue on glass slides (Raman) and silicon nitride windows (XFM), however, there were some differences in how the tissue was immersed in solution to prevent damage to the silicon nitride windows. For the silicon nitride windows, the solutions were dropped onto glass slides containing a wax pen boundary to prevent dispersion, and the windows were placed face down onto the solution for the required time frames. The mounting medium and coverslips were then applied, and nail polish was added to the back of frame to enable it to stick to a glass slide. In the scenario where the membrane detached from the frame, the membrane was kept on a glass slide and the solutions were added drop wise.

Before staining, the sections were imaged using either confocal Raman microscopy or X-ray fluorescence microscopy. To enable co-localisation of stains to the Raman imaged regions, a small area of tissue was deliberately burnt with the Raman laser as a reference point for re-locating the imaged region after staining. For XFM, the imaged region is larger and photobleaching is evident which enabled easy relocation of the same region. The stained tissue was viewed under an Olympus BX-51 upright fluorescence microscope using CellSens software, an UltraView spinning disk confocal microscope utilising Volocity software, or a ZEISS Axio Scan.Z1 slide scanner using Zen software. Images were imported into ImageJ where the colour scale was adjusted, and tri-colour images were generated using the "merge channels" function.

2.3.6.3 Analysis of Beam Damage Following XANES and XFM Imaging and Subsequent Immunofluorescence Staining

Visual inspection of tissue (using fluorescence microscopy) following X-ray imaging and immunofluorescence staining revealed photobleaching and tissue damage in regions exposed to X-rays. To assess the extent of photobleaching and damage, fluorescence images (n=4) with UV and green excitation were opened in ImageJ and regions of interest of a consistent area were drawn in non-irradiated, XFM imaged, and XANES imaged regions. Regions were distinguished based on both the photobleaching/damage, and on the XFM and XANES images. The mean fluorescence value was extracted from the defined regions and a fluorescence value relative to the non-irradiated area was generated. Further statistical analysis was completed using GraphPad Prism in which a one-way ANOVA with multiple comparison testing comparing the X-ray exposed regions to the non-irradiated regions was completed for images with UV and green excitation.

Chapter 3: Characterisation of the Chemical Form of Zn^{2+} in Brain Tissue using K-edge XANES Spectroscopy, and Preliminary Development of a Zinc XANES Imaging Protocol for Brain Tissue

ABSTRACT

Zn is an abundant trace metal required for normal memory function. Memory loss and cognitive decline during natural ageing and neurodegenerative disease have been associated with altered brain-Zn homeostasis. Yet, the exact chemical pathways through which Zn influences memory function during health, natural ageing, or neurodegenerative disease remain unknown. The gap in the literature may in part be due to the difficulty to simultaneously image, and therefore, study the different chemical forms of Zn within the brain (or biological samples in general). This chapter will discuss the development and optimisation of protocols that incorporate XANES spectroscopic analysis of tissue at the Zn K-edge, as an analytical tool to study Zn speciation in the brain. XANES spectroscopy is ideally suited for this task as all chemical forms of Zn are detected, the technique requires minimal sample preparation that may otherwise redistribute or alter the chemical form of Zn, and the Zn K-edge has known sensitivity to coordination geometry and ligand type. In this study, K-edge spectra collected from micro-dissected flash-frozen brain tissue were fitted to a spectral library prepared from standard solutions, to demonstrate differences in the chemical form of Zn that exist between two brain regions, the hippocampus and cerebellum. Lastly, an X-ray microprobe was used to demonstrate differences in Zn speciation within sub-regions of thin air dried and frozen sections of the murine hippocampus, and also to highlight that the chemical form of Zn is easily perturbed by sample preparation such as tissue sectioning or air drying, which must be a critical consideration for future work.

3.1 INTRODUCTION

Zn is an essential component for multiple proteins and enzymes and plays a vital role in healthy brain function [11, 13, 41]. As described in section 1.3, the majority of Zn exists in a protein-bound form, however, 10-15% of it is labile (easily exchangeable) with a particularly concentrated pool of labile Zn present in the synaptic vesicles of a subset of glutamatergic neurons in the hippocampus [40, 42, 43]. Its co-localisation with glutamate suggests a potential role in neurotransmission, and the cognitive decline associated with depletion of this Zn pool suggests an important role in memory function [22, 179-181]. Despite its importance to healthy memory, the exact chemical form of the labile Zn pool, and how its coordination may change following release from the synaptic vesicles during neurotransmission has not been fully elucidated. In fact, imaging and differentiating between the multiple chemical forms of Zn that exist in brain tissue, has long been an unmet analytical challenge.

Several methods are currently available for studying Zn and are detailed in section 1.5. Briefly, atomic absorption spectroscopy (AAS), inductively coupled plasma-mass spectrometry (ICP-MS), and separation methods coupled with mass spectrometry (LC-MS, GC-MS) are useful for studying bulk Zn content, while techniques such as laser ablation inductively coupled plasma mass spectrometry (LA-ICP-MS) [75-78], scanning electron microscopy (SEM), secondary ion mass spectrometry (SIMS) [79] and X-ray fluorescence microscopy (XRF, or XFM) can show the distribution and relative concentration of Zn [20, 80-82]. Histochemical methods and fluorescent probes are also available for studying the distribution of specific chemical forms of Zn. Although these methods are useful, they have limitations associated with sample preparation requirements that can prevent spatially resolved studies and potentially alter Zn speciation (see section 1.5 for further detail). Considering this, a method capable of showing the concentration and distribution of a variety of chemical forms of Zn without the need for extensive sample preparation steps, would be indispensable.

X-Ray spectroscopic techniques have the capacity to fill these requirements and were hence a critical aspect of this study. X-ray absorption near edge structure (XANES) spectroscopy can differentiate between various chemical forms of Zn since the K-edge is sensitive to the ligand type and coordination geometry (see section 1.6 for further detail) [98-100]. It is possible to elucidate the coordination environment in complex chemical samples such as brain tissue, through comparison to spectral libraries that model different forms of metal ion coordination

[103, 133]. Coupling these XANES measurements with the imaging capabilities of X-ray fluorescence microscopy (XFM) enables spatially resolved analysis of Zn speciation at the micron level. Micron or sub-micron resolution XANES mapping/imaging could ultimately lead to the development of spectroscopic imaging protocols to visualise the cellular distributions of different chemical forms of Zn in the brain.

This chapter will discuss the development of a XANES Zn K-edge library of biologically relevant standard solutions and its subsequent application in identifying the most abundant chemical forms of Zn in the hippocampus and cerebellum. Preliminary results from XANES imaging studies will also be described, along with the importance of sample preparation considerations for both standard solutions and tissue sections. Specifically, the changes to Zn speciation in the presence of glassing agents for standard solutions, and for air dried tissue sections compared to frozen tissue sections will be described.

3.2 RESULTS AND DISCUSSION

3.2.1 Interrogation of a XANES Spectral Library Prepared from Standard Solutions

To facilitate interpretation of the spectral differences observed in Zn K-edge XANES spectra recorded from hydrated brain tissue, a spectral library from Zn^{2+} standard solutions was constructed. Building a spectral library from standard solutions, as opposed to model complexes, was chosen on the basis that spectra collected from model compounds measured in the solid state differ (sometimes substantially) from spectra collected in solution [100, 182]. As the ultimate objective was to develop the imaging protocols to investigate Zn speciation *in situ* within hydrated tissue sections, the XANES spectral library was constructed from standard solutions, using a similar approach as applied by the environmental science communities to study Zn speciation in plant tissues [136]. A limitation to the approach of using standard solutions is that the spectra are influenced by chemical equilibria and can not be assumed to reflect a single chemical species, which will be discussed in more detail below.

The XANES spectral library (Figure 3.1) was developed from $Zn^{2+}_{(aq)}$ in the presence of excess amino acids (histidine, cysteine, or glutamate) or excess biologically relevant ions (Cl^-, PO_4^{3-}). The amino acids and ions were chosen based on their known propensity to coordinate Zn^{2+}.

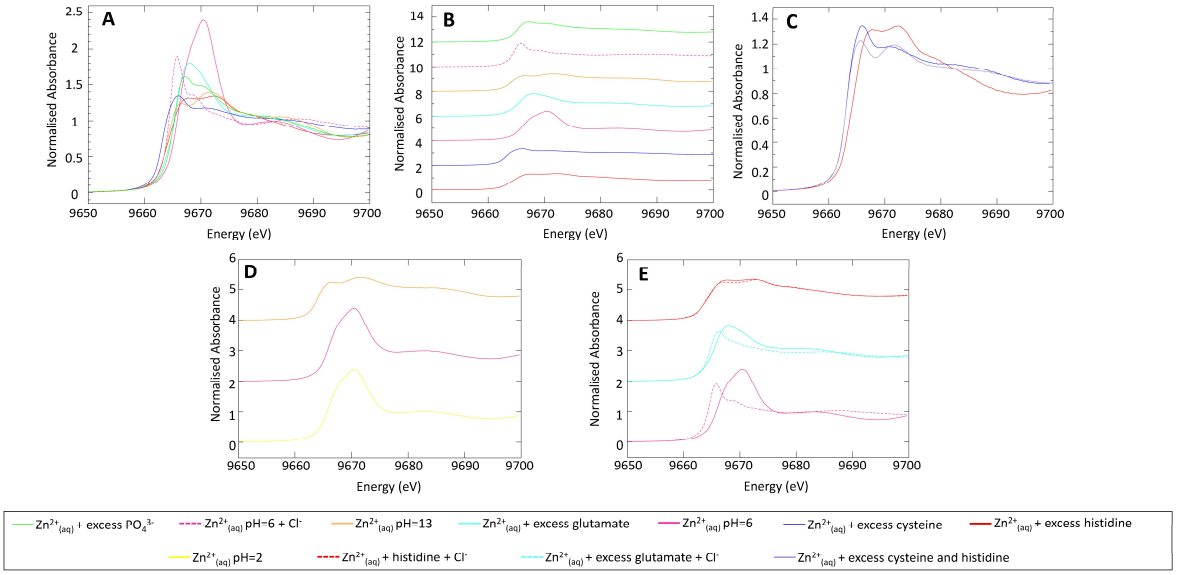

Figure 3.1: *Bulk Zn K-edge XANES spectra of standard solutions. Spectra were recorded from the addition of excess biological ligand to solutions of Zn^{2+}. The spectra are presented overlayed (A) and staggered (B). The spectral difference between solutions of $Zn^{2+}_{(aq)}$ in the presence of excess cysteine, histidine, or a mixture of the two is depicted in panel (C). The effect of pH or adding excess sodium chloride (i.e., excess Cl^- ligand) to the standard solutions is depicted in panels (D) and (E), respectively. In all standard solutions, the source of Zn^{2+} was zinc nitrate hexahydrate dissolved in H_2O.*

Remarkable variation in the position, intensity and shape of the K-edge white line are observed across the spectra of the standard solutions, which confirm the exquisite sensitivity of the Zn K-edge to coordination environment, as recently shown by others [134, 135, 137, 138, 141]. The white line position and normalised intensity for each standard solution are presented in Table 3.1, in addition to the position and intensity of any other main features, secondary "peaks" or shoulders in the absorption edge.

***Table 3.1**: White line position and normalised intensity of Zn K-edge XANES spectra collected from standards that model the coordination environment of Zn^{2+} in the presence of excess amino acids or biologically relevant ions*.*

Standard Solution	White Line		Secondary Peak	
	Position (eV)	Normalised Intensity	Position (eV)	Normalised Intensity
Zn^{2+} + Cysteine	9665.3	1.35	9670.7	1.17
Zn^{2+} + Cysteine + Histidine	9665.0	1.23	9671.1	1.19
Zn^{2+} + Histidine	9667.0	1.32	9671.8	1.35
Zn^{2+} + Glutamate	9667.3	1.80	-	-
Zn^{2+} + H_2O (pH=2)	9670.4	2.40	9667.8 (*sh*)	2.10
Zn^{2+} + H_2O	9670.4	2.39	9667.8 (*sh*)	2.10
Zn^{2+} + H_2O (pH=13)	9665.9	1.24	9670.9	1.40
Zn^{2+} + Cl^-	9665.0	1.90	9667.8	1.36
Zn^{2+} + PO_4^{3-}	9666.5	1.61	9679.4	1.49

*In all cases, $Zn^{2+}_{(aq)}$ was derived from dissolution of $Zn(NO_3)_2$ in H_2O.

(*sh* = shoulder)

As the primary objective of these experiments was to demonstrate the capability of XANES at the Zn K-edge to detect differences in Zn speciation within brain tissue, an exhaustive explanation of the K-edge spectral features of the standard solutions will not be provided. Indeed, elucidating the underlying electronic transitions that account for the spectroscopic variation evident in Figure 3.1 is not trivial, as recently highlighted for model compounds [141]. Further, in this case it is complicated by the likely presence of chemical equilibria between multiple Zn^{2+} coordination complexes that may be present in standard solutions (as opposed to model complexes). Nonetheless, at a relatively superficial level, Figure 3.1 and Table 3.1 reflect known facets of Zn^{2+} coordination chemistry, which at this stage do enable chemical information to be determined from Zn K-edge XANES spectra collected from brain tissue.

Spectroscopic features associated with $Zn^{2+}_{(aq)}$ in solution at pH 2, pH 6 and pH 13

In the standard solution of Zn^{2+} with H_2O at pH 6 it is reasonable to assume that H_2O will be the major ligand, and the octahedral hexaaqua $[Zn(H_2O)_6]^{2+}$ complex the major coordination complex formed. Some extent of chemical equilibria, at least between $[Zn(H_2O)_6]^{2+}$ and

$[Zn(OH)(H_2O)_5]^{1+}$ cannot be ruled out though. At pH 13 ^{-}OH is assumed to be the dominant ligand. It is well established in the literature that $Zn(OH)_{2(s)}$ is highly soluble at pH 13 (solubility 178 x 10^5 mol L^{-1}), due to the formation of the $[Zn(OH)_4]^{2-}$ coordination complex, however a minor contribution from equilibria between $[Zn(OH)_4]^{2-}$ and $[Zn(OH)_3H_2O]^{-}$ cannot be ruled out entirely. Despite the possibility of chemical equilibria, the standard solutions at or below pH 7, and at pH 13 can be viewed to reflect Zn^{2+} in an octahedral coordination through oxygen atoms (at or below pH 7) and Zn^{2+} in a tetrahedral coordination through oxygen atoms (pH 13). As can be seen from Figure 3.1D and table 3.1, there is a substantial increase in white line intensity for the standard solution of $Zn^{2+}_{(aq)}$ at pH 2 and pH 6 relative to pH 13, which can be attributed to the high degree of degeneracy of Zn 4p orbitals in the octahedral complex [99, 183]. Conversely, reduced white line intensity and the presence of two dominant features is observed in the spectra of Zn^{2+} at pH 13, in which the tetrahedral complex $Zn(OH)_4^{2-}$ is expected to be the dominant form [184]. In the tetrahedral ligand field, the Zn 4p orbitals are expected to split and lose degeneracy, which should result in reduced intensity of the white line feature [99, 183]. This reduced intensity could also be attributed to p and d orbital mixing, which may occur in this lower symmetry state. Further, due to the splitting of the Zn 4p orbitals in a tetrahedral field, multiple features or "peaks" in the white line might be expected, and indeed this is observed.

Spectroscopic features associated with standard solutions of $Zn^{2+}_{(aq)}$ in the presence of amino acids (cysteine, histidine, glutamate) or biologically relevant ions (Cl^-, PO_4^{3-})

It is well established that Zn^{2+} forms tetrahedral complexes through coordination with amino acids such cysteine or histidine [185-187]. Indeed, the XANES spectra of standard solutions of $Zn^{2+}_{(aq)}$ in the presence of excess cysteine, histidine, or a 50:50 cysteine/histidine mixture display reduced white line intensity (normalised absorbance < 1.5) with two distinct edge features ("peaks") (Figure 3.1C), which is consistent with a tetrahedral coordination geometry [141]. The K-edge spectrum of $Zn^{2+}_{(aq)}$ + excess glutamate shows a single, relatively intense white line feature, indicating a higher coordination number (possibly octahedral), which is consistent with the studies by others investigating Zn^{2+} coordination in the presence of excess COO^- groups [134, 188]. Again, it is important to emphasise that the XANES spectra recorded from the standard solutions likely reflect chemical equilibria and in the case of $Zn^{2+}_{(aq)}$ in the presence of excess glutamate, the number of coordinating glutamate molecules is not known.

In addition to the effects of coordination geometry, the position of the white line feature in XANES spectra is influenced by the electronegativity of the bonded atoms, and oxidation state, although the effect of oxidation state is not relevant for Zn, which exists exclusively as Zn^{2+} in biological systems. It is well established that the energy of the white line is inversely proportional to bond length [98]. Coordination of Zn^{2+} to small electronegative atoms like O and N is therefore, expected to shift the white line to higher energies, while coordination through larger electron donating atoms such as Cl and S is expected to shift the white line to lower energies [98, 100]. These characteristic features of the XANES K-edge are observed in Figure 3.1A and 3.1B, for the standard solutions, where the likely coordination through S or Cl results in white line features to lower energies relative to standard solutions that likely contain the dominant $Zn^{2+}_{(aq)}$ species coordinated through O or N (as summarised in Table 3.1).

The spectra presented in Figure 3.1 also highlight the importance of considering counter ions that are commonly present in many biological media, as competing coordination ligands. It can be seen in Figure 3.1A and Figure 3.1B, that Zn^{2+} in the presence of Cl^- or PO_4^{3-} produces distinctive XANES spectra, remarkably different from the $Zn^{2+}_{(aq)}$ in water alone. This is not unexpected as these ions are well established to participle in coordination with transition metals [41]. As these ions are commonly found in biological media and reagents (e.g., buffers, cell culture medium), their effect on Zn^{2+} coordination can not be ignored. The ability of counter ions, such as Cl^- to compete for Zn^{2+} is demonstrated in Figure 3.1E, where Cl^- was added to the standard solutions of $Zn^{2+}_{(aq)}$ pH 6, $Zn^{2+}_{(aq)}$ + glutamate, or $Zn^{2+}_{(aq)}$ + histidine. The addition of Cl^- produced dramatic spectral alterations in the first two cases, but no change in the latter case ($Zn^{2+}_{(aq)}$ + histidine). This could be attributable to the classification of Zn^{2+} as an intermediate acid-base (opposed to hard or soft) which means it will preferentially bind to the histidine imidazole ring (an intermediate ligand), compared to Cl^- (a hard base ligand)[41].

Zn^{2+} coordination is perturbed by the use of glassing agents

In light of the dramatic changes to the K-edge XANES spectrum that can result from ligand displacement in the presence of common ions (e.g., Cl^-), the possibility of other chemical additives competing with biological ligands for Zn^{2+} coordination was investigated. Specifically, the Zn K-edge XANES spectra following the addition of a common glassing agent, glycerol was tested. With multiple hydroxyl groups, glycerol could provide ample opportunity to competitively coordinate Zn^{2+}, and indeed Zn^{2+} - glycerol coordination complexes are known to exist [189]. Further, a recent study has highlighted that the use of glycerol as a glassing agent can exacerbate photodamage, which emphasises the potential limitations of its use[189]. The effect of glycerol on two standard solutions, $Zn^{2+}_{(aq)}$ in the presence of excess cysteine or histidine, was investigated. Substantial changes to the K-edge XANES following the addition of glycerol was observed (Figure 3.2).

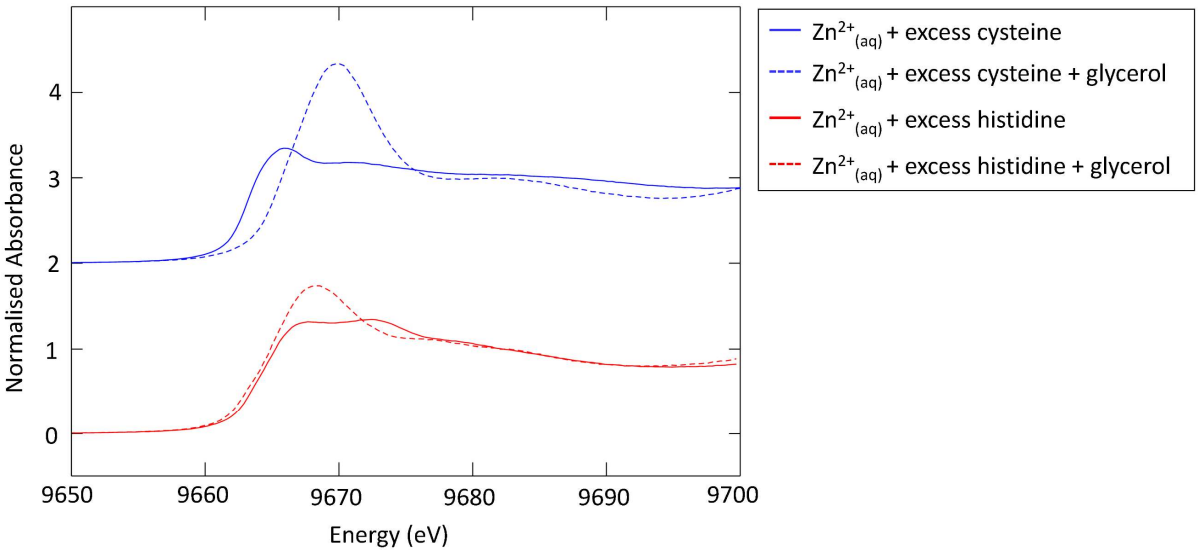

Figure 3.2: *Bulk Zn K-edge XANES spectra of select standard solutions, showing that the addition of glycerol glassing agents affects Zn^{2+} coordination. This can be seen in Zn K-edge XANES spectra recorded for $Zn^{2+}_{(aq)}$ in the presence of excess cysteine (10 mM), or $Zn^{2+}_{(aq)}$ in the presence of excess histidine (13 mM), both with and without the addition of the glycerol glassing agent.*

In both cases there was a shift of the white line feature to a higher energy, 9965.3 to 9669.2 eV associated with the displacement of cysteine, and 9667.0 to 9667.6 eV associated with the displacement of histidine. There was also the disappearance of the distinctive "doublet" feature in the absorption edge following addition of glycerol, concomitant with an increase in

white line intensity. These spectroscopic changes are consistent with conversion of Zn^{2+} from a tetrahedral coordination environment associated with cysteine or histidine ligands, and the formation higher coordination number Zn^{2+} complexes, possibly octahedral, and most likely through coordination with oxygen atoms of glycerol hydroxyl groups. These results further emphasise the importance of considering all stages of sample preparation when undertaking direct spectroscopic measurement and indicate that the use of glycerol glassing agents may not be suitable for recording spectra of standard solutions in an aqueous environment. This finding has important implications for collection of extended X-ray absorption fine structure (EXAFS) spectra as a tool to determine the exact bonding environment of Zn^{2+}. EXAFS spectroscopy is well suited to reveal coordination number and determine average bond lengths, and would have been an ideal tool to further characterise the standard solutions analysed in this thesis [98, 100]. The EXAFS signal however, is much weaker and requires data collection over a wider energy range relative to XANES. EXAFS is therefore, more prone to interferences from ice crystal diffraction, and thus the use of glassing agents common practice (often essential). Unfortunately, the results of this thesis have shown that glassing agents such as glycerol easily perturb the coordination environment of standard solutions of Zn^{2+}, and therefore, although the EXAFS spectrum could be easily recorded, it would reveal information on coordination complexes produced by mixing of the standard solution and glassing agent, and not purely the standard solution. Consequently, detailed EXAFS characterisation was not undertaken.

3.2.2 Application of XANES Spectroscopy at the Zinc K-edge to Reveal Differences in Zinc Speciation between Two Brain Regions, the Hippocampus and Cerebellum

The spectral library of standard solutions was applied to fit the Zn K-edge XANES spectra collected from flash frozen micro-dissected rat brain tissue, specifically the cerebellum and hippocampus. These two regions were chosen as they are both enriched in Zn, reported to contain 36 ± 8 µg/g Zn (dry weight, cerebellum) and 70 ± 10 µg/g Zn (dry weight, hippocampus)[18], but the cerebellum does not contain abundant labile Zn^{2+}, while the hippocampus does [45, 88]. A comparison of the Zn K-edge XANES spectra from both brain regions would therefore, be expected to reveal differences in Zn speciation, on the assumption that the labile Zn pool exists with different coordination environment relative to non-labile pools. It is important to emphasise however, that the fitting results of this study

reveal Zn coordination that resemble the coordination environment observed in standard solutions, which may contain chemical equilibria, and should not be interpreted to represent fittings of unique coordination compounds. The latter could only be obtained through using a library of spectra from model coordination compounds, which as discussed already, has not been undertaken due to the spectroscopic differences known to occur between the solid state and in solution [100, 190].

Representative examples of Zn K-edge XANES spectra that were fit to linear combinations from the library of standard solutions are presented in Figure 3.3A (hippocampus) and 3.3B (cerebellum). Multiple fitting combinations were trialled, but the best fits (lowest residuals) were obtained through fitting the tissue spectra to a linear combination of the spectra of standard solutions from: $Zn^{2+}_{(aq)}$ + histidine, $Zn^{2+}_{(aq)}$ + glutamate, and $Zn^{2+}_{(aq)}$ + co-added histidine and cysteine (Figure 3.1C). The inclusion of the latter likely supports the existence of Zn^{2+}, in numerous proteins, coordinated through both histidine and cysteine amino acid residues [39, 47, 58, 191]. The average fits values (as % of total Zn pool) for each tissue region are presented in Figure 3.3A (hippocampus) and Figure 3.3B (cerebellum) and the data suggest the majority of Zn^{2+} is in a coordination environment indicative of mixed cysteine and histidine coordination. This is not unexpected as Zn^{2+} is known to be coordinated through these amino acids in many metalloproteins such as metallothionein, and Zn-finger proteins [39, 47, 58, 191]. In addition, on average in the cerebellum, there was increased coordination of Zn^{2+} in an environment that resembled the standard solution of $Zn^{2+}_{(aq)}$ with excess histidine (trending towards significant, $p = 0.0929$). In the hippocampus there was increased coordination in an environment that resembled the standard solution of $Zn^{2+}_{(aq)}$ in the presence of excess glutamate (statistically significant $p = 0.0039$).

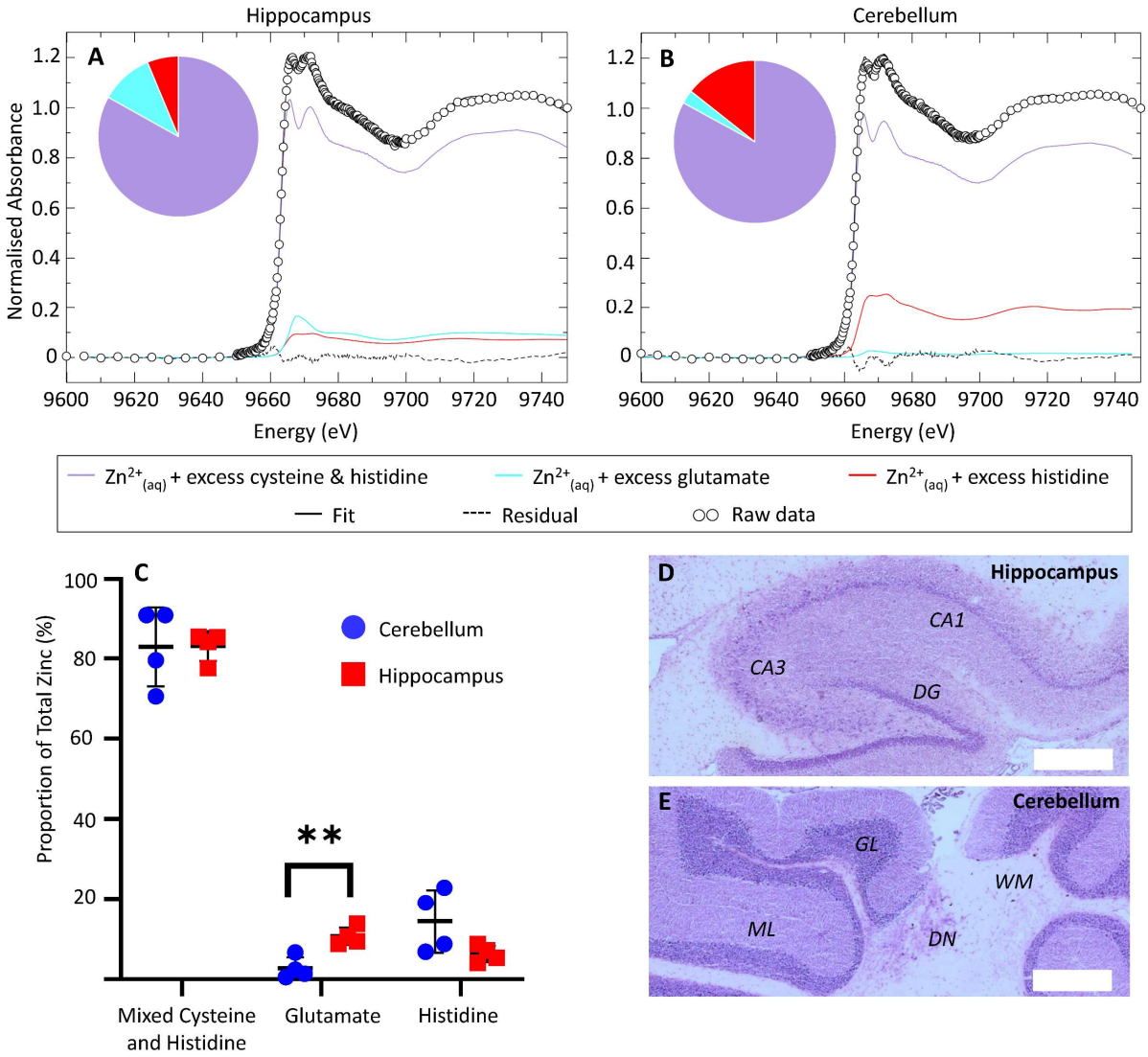

Figure 3.3: *Results of fitting bulk Zn K-edge XANES spectra collected from the hippocampus (A) and cerebellum (B), to a linear combination of standard solution spectra. Fitting results are depicted as a graph showing the percentage proportion of Zn chemical form in each brain region (C). p values were obtained using an unpaired Student's t-test with a 95% confidence interval. CA1 = cornus ammonis layer 1, CA3 = cornus ammonis layer 3, DG = dentate gyrus, DCN = dentate nucleus, GL = granular layer, WM = white matter, ML = molecular layer. Scale bars represent 500 µm.*

The results appear to indicate increased coordination of Zn^{2+} through histidine in the cerebellum, which is not unexpected, due to the abundant white matter in the cerebellum relative to the hippocampus (as shown in H&E images presented in Figure 3.3 D, E), which contains histidine rich myelin proteins [192]. The cerebellum however, is a heterogeneous structure and large variation is expected in the exact amounts of molecular layer, granular

layer, and white matter structures that were analysed in the bulk micro-dissected brain sample, which could account for the larger standard deviation in fitting results observed for the cerebellum.

The significant increase within the hippocampus of Zn^{2+} coordinated in an environment similar to that modelled by the standard solution of $Zn^{2+}_{(aq)}$ + excess glutamate, suggests that a high coordination number, possibly octahedral coordination of Zn^{2+} through carboxylate ligands (COO^-) contributes to the labile Zn^{2+} pool. Multiple authors have speculated on the exact chemical form of Zn^{2+} that exists within the labile pool, which is detected by histochemical stains such as the Timm's stain. Commonly suggested chemical forms include "free" Zn^{2+}, low molecular weight Zn^{2+} + amino acid complexes, a specific Zn^{2+} - glutamate complex, or Zn – glutathione complex. The first structure can be discounted, as Zn^{2+} will not exist as the free ion, and at the very least will exist as an octahedral aquo-complex with a first coordination shell containing six H_2O ligands [184]. However, given the abundance of biological ligands it would seem highly unlikely that Zn^{2+} exists as the octahedral hexaaqua complex to any appreciable extent in biological systems [184, 193]. Indeed, the standard solution spectra of Zn^{2+} in H_2O at pH 6 was not found to contribute to any linear combination of fitting applied to hippocampal or cerebellum tissue.

The results of this study could be taken to provide evidence that the labile Zn pool, or at least a component of the labile Zn pool exists in a high coordination number, possibly octahedral complex, coordinated through COO^- residues. The ability of the addition of Cl^- to drastically alter the K-edge XANES spectra of $Zn^{2+}_{(aq)}$ + excess glutamate (Figure 3.1 E), highlights that a component of glutamate coordination to Zn^{2+} can be labile. Indeed, some authors have argued for the existence of a specific Zn^{2+} – glutamate complex because Zn^{2+} and glutamate are concomitantly released during neuronal activity [10, 13, 44]. Others however, make convincing cases that other chemical forms of labile Zn^{2+} must exist in addition to any potential Zn^{2+} – glutamate complex, with the arguments based on the relative concentrations of Zn^{2+} and glutamate found within the synapses [43]. Although glutamate was used as the "model" ligand for the standard solution in this study, coordination through the COO^- group of other amino acids (e.g., aspartate) is certainly possible, and still likely to be well modelled by, and therefore potentially indistinguishable from glutamate in this study. Despite the existence of a chemical form of Zn^{2+} in the hippocampus that resembles the standard solution of $Zn^{2+}_{(aq)}$ + excess

glutamate, by far the dominant chemical form of Zn^{2+} in the hippocampus resembles the standard solution of $Zn^{2+}_{(aq)}$ + cysteine and histidine. It is entirely plausible that the hippocampus contains increased abundance of Zn^{2+} in an octahedral coordination, which is separate from the labile Zn^{2+} pool, which could also account for these results. Clearly, further studies at the cellular and subcellular level, with biological manipulations to increase or decrease the labile Zn^{2+} may help aid elucidation of the specific chemical forms of Zn^{2+} within the hippocampus.

Based on the fitting results, it may be viewed that only three distinct Zn^{2+} coordination environments exist in cerebellum and hippocampus, which is almost certainly not the case. It is clear from visual inspections of the residuals, that components of the white line are not correctly modelled by this fitting process with the spectral library at hand. It is likely that further expansion of the spectral library and refinement of the fitting process may identify additional chemical forms of Zn^{2+} contributing to the average spectrum. Therefore, the results of this study should be viewed with some caution and the knowledge that the fitting process has likely only demonstrated the presence of the 3 major coordination environments of Zn^{2+} that dominate the average spectrum of brain tissue. Nonetheless, it is hoped that these results provide the foundation for the field to further build from, opening new opportunities to study Zn^{2+} speciation in biological systems.

3.2.3 Micro-XANES Analysis of Zinc Speciation in Hippocampal Neurons and Mossy Fibres in Air Dried and Frozen Tissue Sections

To further investigate the chemical form of Zn^{2+}, specifically the chemical form of labile Zn^{2+} that exists within the hippocampus, micro-XANES measurements were made. The measurements were recorded through a XANES-imaging protocol at the XFM beamline of the ANSTO-Australian Synchrotron, with 98 to 125 fluorescence maps collected at successive incident energies scanned through the Zn K-edge (see Figure 1.5). This approach to data collection enabled accurate definition of the sub-regions within the hippocampus, such as the pyramidal cell layer (high Fe, low average Zn but localised Zn elevation in cell bodies) and the CA3 mossy fibre region (moderate Fe, and high Zn). The identification of these sub-regions is outlined in Figure 3.4.

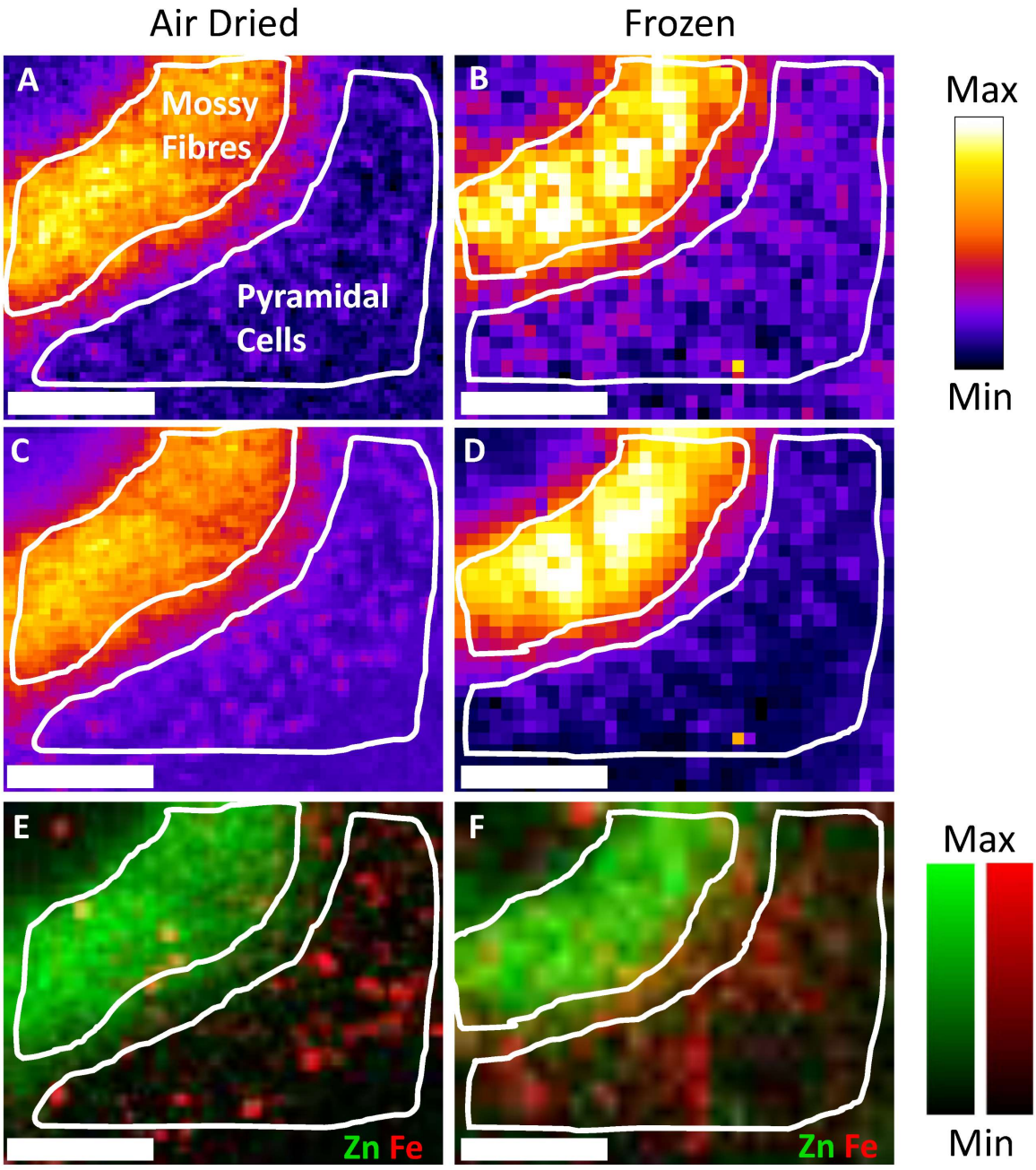

Figure 3.4: *False colour XFM elemental maps showing the distribution of Zn and Fe in the mossy fibres and pyramidal cells of air dried (10-µm thick) and frozen (14-µm thick) hippocampus tissue sections. Panels A and B are total Zn images generated from the Zn map collected at the highest incident energy (9803 eV). Panels C and D are total Zn images generated from the sum of images representing different Zn coordination environments ($Zn^{2+}_{(aq)}$ with excess cysteine, $Zn^{2+}_{(aq)}$ with excess histidine, $Zn^{2+}_{(aq)}$ with excess PO_4^{3-}). The Zn and Fe overlay images (E, F) were collected at the highest incident energy (9803 eV) and highlight the localisation of Zn to the mossy fibres and Fe to the pyramidal cells. All images have 4x4 pixel binning applied. Scale bars = 100 µm.*

Investigating Zn^{2+} speciation within the CA3 pyramidal cell layer and the CA3 mossy fibres was of specific interest as the former does not appear enriched in a labile Zn pool (based on histochemical studies [43, 45]), while the latter is the brain region most enriched in labile Zn. For simplicity and because successful elemental mapping had been completed in previous experiments, initial analysis was carried out on air dried tissue sections. The average XANES spectrum for both the mossy fibres and pyramidal cells (Figure 3.5), showed substantial differences compared to the bulk XAS spectra collected from frozen hippocampal tissue (Figure 3.3). These visual differences were supported by linear fitting to the spectral library of standard solutions. The "best" fits (lowest residuals) were obtained from a linear combination of 3 standard solutions: $Zn^{2+}_{(aq)}$ + excess cysteine, $Zn^{2+}_{(aq)}$ + excess histidine, and $Zn^{2+}_{(aq)}$ + excess PO_4^{3-}.

As with the bulk XAS study, close inspection of the residuals indicates that other chemical forms of Zn^{2+} are most likely contributing but are not completely modelled by the library of standard solutions. These results should therefore be interpreted with some caution as they likely only reflect the major chemical forms of Zn^{2+} present. Nonetheless, it is clear that Zn^{2+} coordinated in an environment modelled by the standard solutions of $Zn^{2+}_{(aq)}$ + excess PO_4^{3-}, and $Zn^{2+}_{(aq)}$ + excess cysteine, make major contributions to the spectra of air dried tissue sections, but not spectra of flash-frozen tissue. These changes are not likely attributed to species variation (i.e. rat vs mouse), as the labile Zn^{2+} pool is highly conserved across species [83, 89]. Rather, these drastic changes in speciation could have been introduced through sample preparation, specifically tissue sectioning and air drying. It is possible that as the tissue sections dry, local concentrations of Zn^{2+} ions and ligands increase far above that encountered *in vivo*, altering coordination equilibria and disturbing competitive ligand binding environments. It would appear that coordination to PO_4^{3-} is favoured during the air drying process. To further investigate this, XANES imaging was repeated using frozen tissue sections with analysis completed under a cryostream. It was apparent that there was still contribution from PO_4^{3-} with the best fit for both the mossy fibres and pyramidal cells still obtained from a linear combination of $Zn^{2+}_{(aq)}$ + excess cysteine, $Zn^{2+}_{(aq)}$ + excess histidine, and $Zn^{2+}_{(aq)}$ + excess PO_4^{3-} (Figure 3.5).

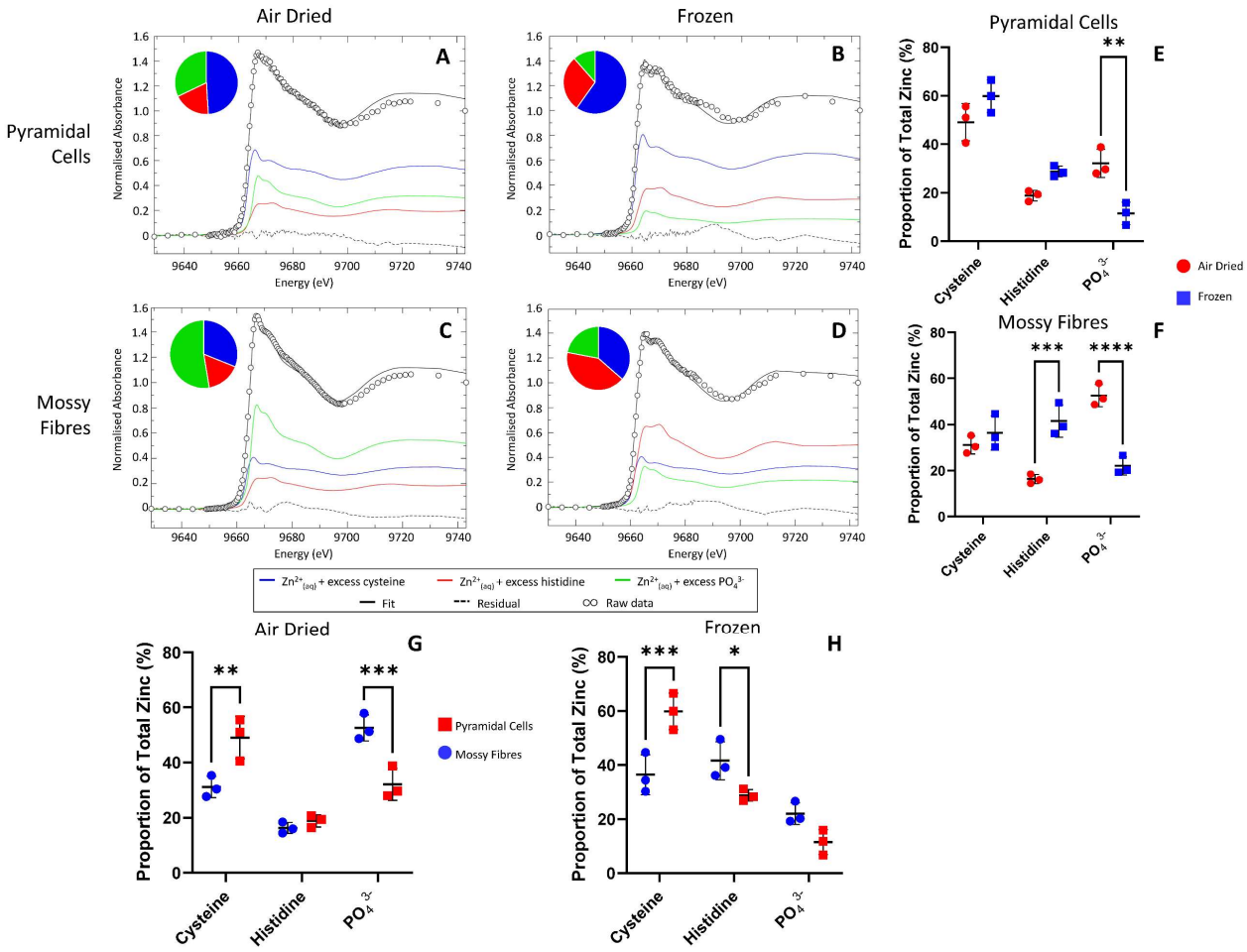

Figure 3.5: *Results of fitting Zn K-edge XANES spectra collected from the pyramidal cells (A, B) and mossy fibres (C, D) of air dried (A, C) and frozen (B, D) SAMP8 12m tissue sections to a linear combination of standard solution spectra. Fitting results are depicted as a graph showing the percentage proportion of Zn chemical form in each brain region. p values were obtained using a two-way ANOVA with multiple comparison testing with comparisons made between air dried and frozen tissue for both regions (E, F), in addition to a regional comparison for each tissue type (air dried and frozen) (G, H). *p≤0.05, **p≤0.01, ***p≤0.001.*

Interestingly, the percentage contribution of PO_4^{3-} to the fit was less in the frozen tissue compared to the air dried tissue with an average of 11% and 22% for frozen pyramidal cells and mossy fibres, respectively, and an average of 32% and 53% for air dried frozen pyramidal cells and mossy fibres, respectively. When considering that the air drying process is likely promoting the coordination of Zn to PO_4^{3-}, it suggests that the "frozen" tissue sections experience thawing and drying during the sectioning, mounting, and analysis process, albeit to a lesser extent than the completely air dried samples. Evidently, the "frozen" sections imaged using the XFM beamline do not reflect the same Zn environment that was observed

in the bulk flash frozen “blocks” of tissue measured using XAS, and rather reflect a partially frozen tissue state somewhere between completely frozen and completely air dried. This partial thawing can likely be attributed to the difficulty in maintaining low temperatures for the complete duration of the sample mounting and analysis process. For example, the mounting of silicon nitride onto the carbon fibre rods is a challenging process that must be completed over dry ice, and once mounted, the sample must be immediately moved into the cryostream. Any delays to these processes or removal of the samples from dry ice has the potential to cause thawing/drying and alter Zn coordination.

These findings make it clear that the *in vivo* Zn coordination environment can not be studied directly in air dried or partially frozen tissue sections. Interestingly however, although coordination of Zn^{2+} with PO_4^{3-} may be an artifact of sample preparation, a significant difference was observed with respect to the % of Zn^{2+} in a coordination environment modelled by the standard solution of $Zn^{2+}_{(aq)}$ + excess PO_4^{3-}, between the pyramidal cell layer (32 %) and the mossy fibre region (53 %), p = 0.0007 (Figure 3.5). A similar trend is also observed in the frozen (partially frozen) tissue sections, however, it is not statistically significant, likely due to variations in the extent of air drying across sections. Based on these results, it is possible that coordination of PO_4^{3-} to Zn^{2+} in tissue sections is influenced by the availability of labile Zn^{2+} *in vivo*. Therefore, the increased coordination of Zn^{2+} to PO_4^{3-} observed in the mossy fibres relative to pyramidal cells, likely reflects a greater *in vivo* abundance of labile Zn in the mossy fibre region (which is to be expected). Although Zn speciation is altered in air dried and partially frozen tissue sections, it may be possible to infer information about the abundance and distribution of labile Zn^{2+} or overall alterations to Zn homeostasis, based on XANES analysis of Zn speciation in these tissue sections. However, it is clearly preferable moving forwards to undertake Zn K-edge micro-XANES and XANES-imaging analysis in completely frozen tissues.

Differences were also observed in the % of Zn^{2+} in a coordination environment modelled by the standard solution of $Zn^{2+}_{(aq)}$ + excess cysteine, between the pyramidal cell layer and the mossy fibre region in both air dried and partially frozen tissue. Specifically, in both tissue types, the contribution from $Zn^{2+}_{(aq)}$ + excess cysteine was significantly greater in the pyramidal cell layer compared to the mossy fibres. This is unsurprising when considering the abundance of cysteine rich proteins in cell bodies (such as those found in the pyramidal cell

layer) that readily bind Zn, such as metallothioneins or Zn-finger proteins. There was also a significantly elevated contribution from $Zn^{2+}_{(aq)}$ + excess histidine in the mossy fibres compared to the pyramidal cell layer in partially frozen tissue. When this is considered along with the differences in speciation in the mossy fibres of air dried compared to frozen tissue (reduced contribution from PO_4^{3-} and increased contribution from histidine in frozen tissue) it could be inferred that the labile Zn that is proposed to coordinate with PO_4^{3-} during the air drying process, is coordinated (at least partially) to histidine when frozen. This requires further analysis of completely frozen tissue to confirm but would make sense given Zn's affinity for binding histidine residues in many proteins.

A comparison of Zn speciation in 5m and 12m SAMP8 mice was also carried out to gain preliminary insights into whether age appears to alter Zn speciation. Interestingly, there was no statistically significant differences in Zn speciation between time points in either the air dried or the frozen tissue sections (Figure 3.6). However, this experiment did have low statistical power (<50%), with only n = 3 biological replicates. It is interesting to note that although not statistically significant, the % of Zn^{2+} coordinated to PO_4^{3-} was greater in all 3 animal replicates of SAMP8 mice aged 12m, compared to all 3 animal replicates of mice aged 5m in air dried tissue. Further analysis with a greater number of animal replicates is required before any definitive statements can be made. Likewise, as stated previously, ideally this experiment should be repeated for completely frozen tissue sections to reflect the *in vivo* Zn environment more accurately. Additionally, if differences in the extent of tissue thawing and drying could be minimised (i.e. all tissue remains completely frozen), variation in data points could potentially be minimised and more accurately reveal whether there is an age dependent change in Zn speciation.

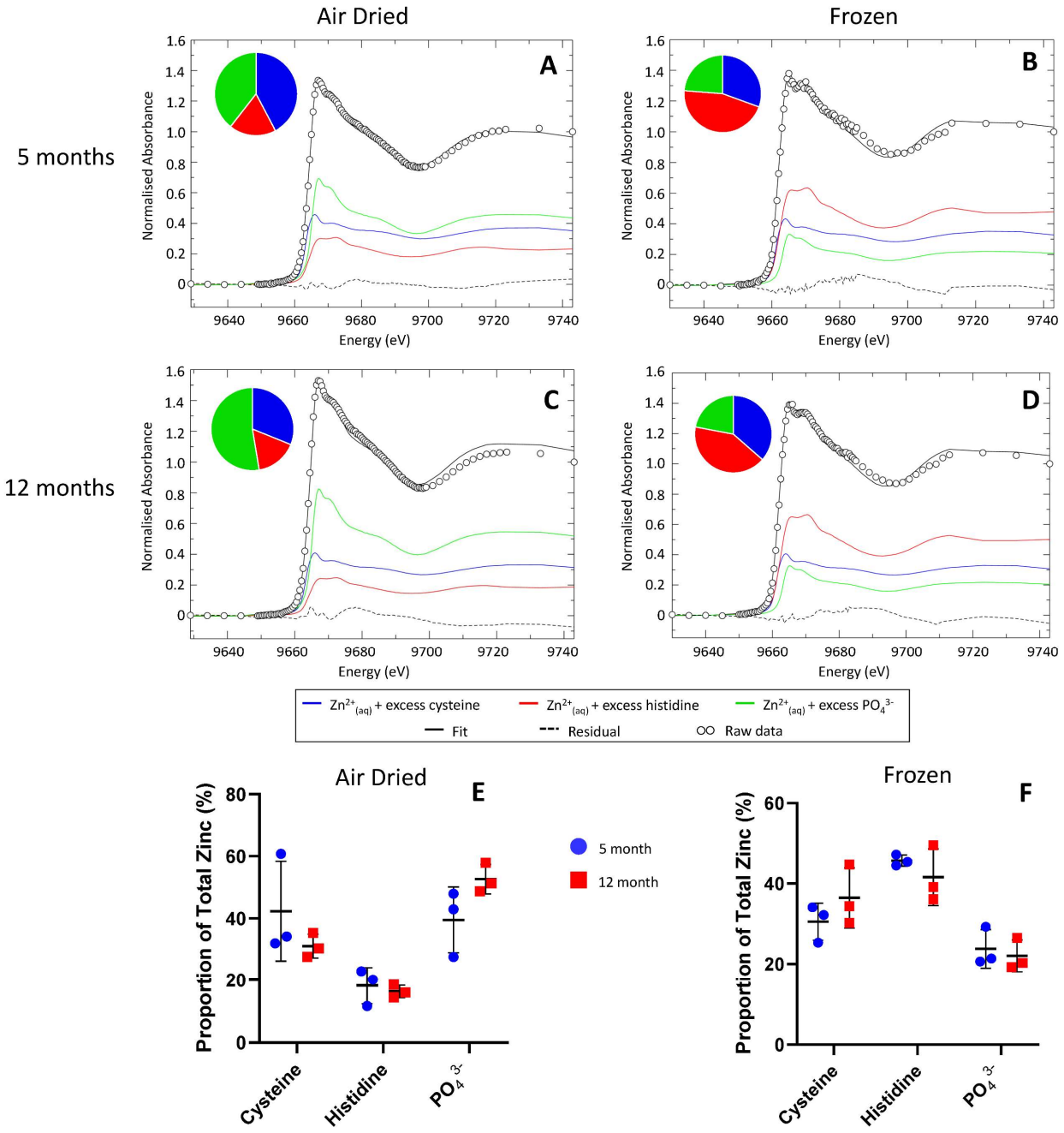

Figure 3.6: *Results of fitting Zn K-edge XANES spectra collected from the mossy fibres of 5m (A, B) and 12m mice (C, D) (air dried (A, C) and frozen (B, D) tissue sections), to a linear combination of standard solution spectra. Fitting results are depicted as a graph showing the percentage proportion of Zn chemical form in each brain region. p values were obtained using a two-way ANOVA with multiple comparison testing. No statistically significant differences were observed across time points in either air dried (E) or frozen (F) tissue.*

In addition to enabling spectra from specific regions to be extracted and compared as demonstrated above, another advantage of XANES imaging is the ability to generate

chemically specific maps to visually show the distribution of various chemical species. MANTiS software enables spectra to be fitted to XANES image stacks using inbuilt single value decomposition and the standard solution spectra, allowing the distribution of each chemical species to be viewed. Unfortunately, the signal-to-noise ratio per pixel in the frozen tissue images was not sufficient to enable accurate representation of the spectral fitting results (likely due to differences in experimental set up and the detector used for those measurements), therefore, only an example of the air dried tissue XANES images is provided as proof of concept (Figure 3.7). The total Zn maps and the multi-element composite images help to highlight key regions in and around the hippocampus including the corpus callosum, mossy fibres, and pyramidal cells. It is evident based on visual inspection of the fitted XANES images (Cys, His, PO_4^{3-}) that Zn coordination does vary across hippocampal sub-regions. For example, the spectrum of the standard solution of Zn^{2+} with excess PO_4^{3-} shows the biggest contribution in the mossy fibres which is visible in both the XANES image and the spectral fit. Additionally, while the solution of Zn^{2+} with excess histidine does not make the largest contribution to the spectral fit in the corpus callosum compared to other standard solution spectra, this region does contain the highest level of Zn^{2+} with excess histidine compared to any other sub-region, which is evident in the image. Finally, the standard solution of Zn^{2+} with excess cysteine makes the largest contribution to all sub-regions except for the mossy fibres, and its predominance in the cell bodies compared to other regions is particularly emphasised in the XANES image. Overall, while these images and spectral fits are not likely reflecting the *in vivo* Zn coordination environment, they are a valuable proof of concept for this imaging protocol and highlight the information that can be obtained when adequate signal-to-noise ratios are achieved. Future experiments should be completed for frozen tissue and the experimental set up optimised to ensure the signal-to-noise ratio will enable generation of XANES images that accurately reflect the Zn coordination environment.

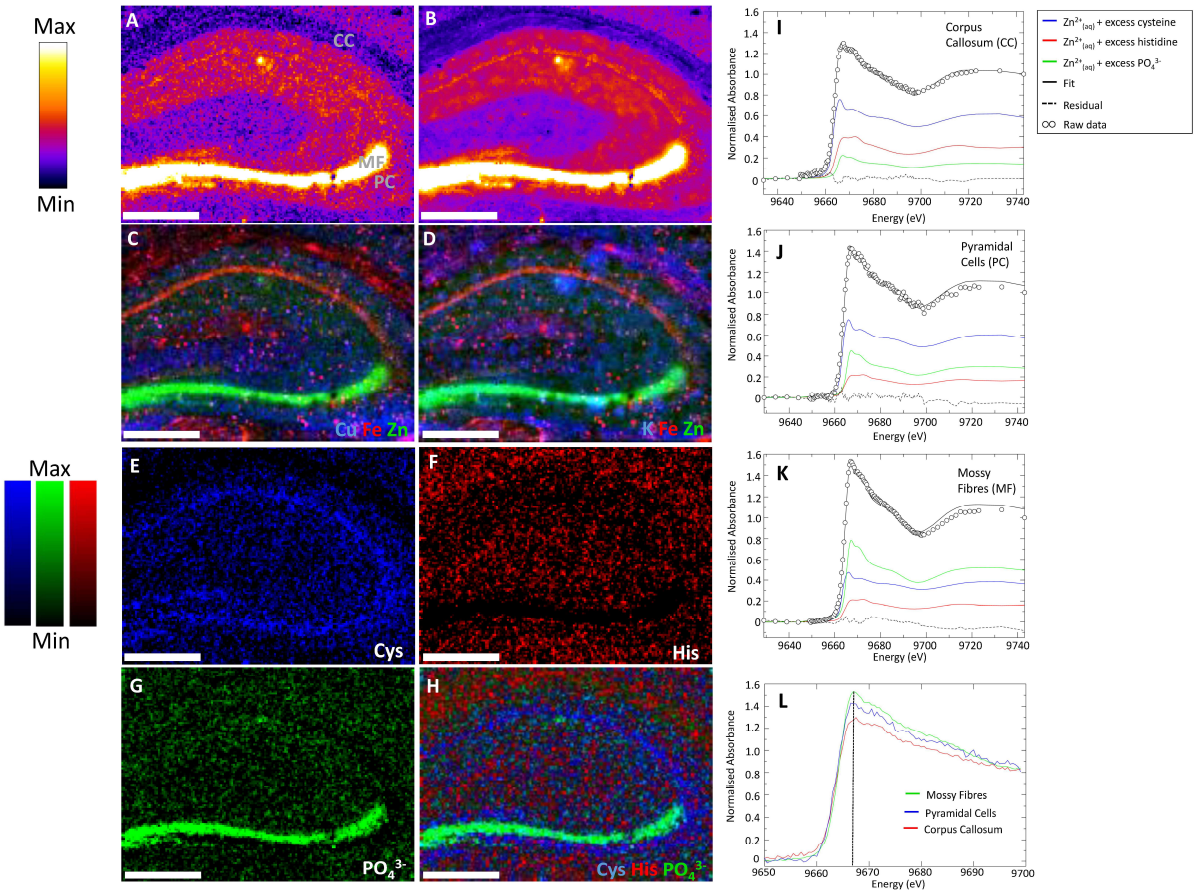

Figure 3.7: *False colour images showing the distribution of Zn, Cu, Fe and K in the hippocampus of an air dried tissue section. The total Zn images were generated from the Zn map collected at the highest incident energy (9803 eV) (A) or from the sum of images representing different Zn coordination environments ($Zn^{2+}_{(aq)}$ with excess cysteine, $Zn^{2+}_{(aq)}$ with excess histidine, $Zn^{2+}_{(aq)}$ with excess PO_4^{3-}) (B). The composite elemental maps (C, D) were collected at the highest incident energy (9803 eV) and highlight the elemental distribution in different hippocampal sub-regions. The Cys, His, and PO_4^{3-} images show the distribution of Zn in different coordination environments ($Zn^{2+}_{(aq)}$ with excess cysteine (E), $Zn^{2+}_{(aq)}$ with excess histidine (F), $Zn^{2+}_{(aq)}$ with excess PO_4^{3-} (G)) and are normalised to total Zn (B). Panel H shows a composite of each Zn coordination environment. The results of fitting Zn K-edge XANES spectra collected from three hippocampal sub-regions to a linear combination of the standard solution spectra are shown on the right, along with spectra from each region highlighting the subtle spectral differences in the white line feature. Fitting results are depicted as a graph showing the percentage proportion of Zn chemical form in each brain region. All images have 4x4 pixel binning applied. Scale bars = 500 µm.*

3.3 CONCLUSION

In this study, common counter ions in biological systems and reagents (e.g., Cl^-), common glassing agents used to prepare samples (e.g., glycerol), and common sample preparation for biological tissues (sectioning and air drying) have been shown to dramatically alter the chemical form of Zn^{2+}. Such findings emphasise the importance of careful experimental planning, consideration, and investigation of the effects of sample preparation for *ex vivo in situ* spectroscopic analysis. With the knowledge of these experimental limitations, a XANES spectral library developed from standard solutions was applied to reveal differences in Zn^{2+} speciation between the cerebellum and hippocampus. The results indicate that the hippocampus contains increased abundance of Zn^{2+} in a chemical form that resembles an octahedral coordination complex. This finding could not be confirmed through micro-XANES analysis however, due to the use of air dried and partially frozen sections that appear to alter the chemical form of Zn^{2+} from that observed *in vivo*. Differences in Zn speciation were however, observed between hippocampal sub-regions that contain primarily either neurons or mossy fibres, and the differences support the existence of a labile Zn pool in the mossy fibres. Future experiments should focus on expanding and further characterising the spectral library of standard solutions. Additionally, *in situ* XANES imaging of flash frozen tissue that remains completely frozen for the duration of the experiment to study Zn^{2+} speciation within tissue that has not been sectioned or air dried, should be carried out.

Chapter 4: Age-Related Changes to the Subventricular Zone of Senescence Accelerated Mouse Prone 8 (SAMP8) Mice

ABSTRACT

Cu is a vital cofactor and structural component for a number of enzymes, and its redox activity is essential for multiple biological processes. While an essential micro-nutrient, unregulated levels of Cu have the potential to catalyse the generation of ROS, causing subsequent oxidative stress and damage. Oxidative stress has been implicated in the ageing process and elevated markers of oxidative stress have been detected in AD brains. Consequently, altered homeostasis or accumulation of metals such as Fe and Cu that can induce oxidative stress have gained attention in age-related studies of brain health. Several studies report increases to these metals during ageing, and one such example is the age-dependent accumulation of Cu in the subventricular zone of rodent models. While it is well established that the redox active metal accumulates in this region, there is limited knowledge on whether its presence actually induces significant levels of oxidative stress. Therefore, this study investigated whether the increased Cu content in old SAMP8 mice was accompanied by an elevation in key spectroscopic markers of oxidative stress. Specifically, XANES spectroscopy was used to investigate whether disulfide concentration increased as a result of thiol oxidation, and FTIR microscopy was used to measure whether lipid peroxidation products or protein aggregates were elevated in old (12m) compared to adult (5m) mice. Surprisingly, elevated spectroscopic markers of oxidative stress were not detected in 12m SAMP8 tissue sections, however, they were detected in follow up *in vitro* "test tube" experiments that involved addition of Cu to brain homogenates (at a concentration equivalent to the magnitude of the Cu increase observed across 5m to 12m old mice). While the results of this study can not conclusively rule out increased levels of oxidative stress in 12m SAMP8 tissue, they do suggest that there are protective mechanisms in place to supress Cu mediated generation of ROS and minimise subsequent oxidative damage. This chapter will further discuss the results, their potential implications to brain biochemistry during ageing, and finally, provide suggestions for further work.

4.1 INTRODUCTION

Mild cognitive decline is associated with natural ageing, however, severe loss of cognitive function and memory is associated with neurodegenerative diseases such as AD. As described previously, AD is the most common form of dementia and ageing is the biggest risk factor for its onset [2, 6]. With an ageing population and the significant social and economic burdens associated with the disease, it is vital that mechanisms contributing to natural brain ageing and the switch to AD are elucidated so that preventative or treatment options can be established.

A chemical pathway likely to be involved in the transition from healthy brain ageing to neurodegeneration and AD, is oxidative stress [23, 24, 194]. Markers of oxidative stress are observed to increase in the brain during ageing and senescence, with significantly elevated levels of oxidative stress observed during AD [24, 194, 195]. Whether this role is cause or consequence is yet to be confirmed, highlighting the need for further research. A variety of factors can trigger oxidative stress, including redox active metals such as Cu and Fe [23-26]. Specifically, they have the capacity to catalyse the production of ROS through Fenton and Fenton-like chemical pathways (see section 1.2), which can subsequently trigger lipid peroxidation processes, and oxidative damage to nucleic acids and proteins if they are not adequately regulated [27-29].

Fe and Cu levels are established to increase in the ageing brain [17, 65, 196-198], and during neurodegenerative disease which has given rise to the “metal hypothesis of ageing”, which essentially attributes heightened levels of oxidative stress that are observed during ageing to the elevated levels of redox active metals commonly observed when comparing aged brains to non-aged brains. In the specific case of Cu (the focus of this chapter), Cu has been reported to increase in several brain regions during ageing, particularly in the SVZ [65, 197]. The SVZ and the ventricles it surrounds hold important roles for the production and transport of CSF (which acts to cushion and provide nutrients to the brain) [199, 200]. Brain ventricles, cells within the ventricles (choroid plexus), and the SVZ (region along the outside wall of the ventricle) have also been proposed to have critical roles in helping maintain brain-metal homeostasis [9, 70, 115]. Interestingly, multiple authors have observed highly enriched Cu deposits within the SVZ, across multiple animal models [65, 197, 200, 201]. Pushkar et al (the first to make this observation) has studied the cell location of the Cu in detail, revealing localised, punctate

increases of Cu within glial fibral acidic protein (GFAP) positive cells (astrocytes) in Sprague Dawley rats [65]. Interestingly, astrocytes have been proposed as the cell type with the largest influence on Cu [9, 65]. The abundance of the Cu deposits was observed to increase during ageing in rats, as well as in wildtype mice [65, 197, 200, 201]. Given the propensity for Cu ions to catalyse free radical production, an association between age-related SVZ Cu increases and heightened oxidative stress seems likely. This is further supported by results from Pushkar et al that reveal that the Cu accumulated in the SVZ is predominantly in its reduced form (Cu^{+}) [65].

The primary aim of this chapter has been to determine if there is an association between age-related Cu accumulation in the SVZ and markers of oxidative stress. To avoid the possibility for confounding interpretation that can occur when using indirect markers, this study utilised direct spectroscopic analysis. Specifically, X-ray fluorescence microscopy was used to evaluate Cu levels, X-ray absorption spectroscopy was used to evaluate disulfide levels (as a marker of oxidative stress), and Fourier transform infrared spectroscopy was used to evaluate levels of unsaturated lipids, aldehyde functional groups, and aggregated β-sheet proteins (also as markers of oxidative stress). The analysis has been undertaken in adult (5m) and aged (12m) senescence accelerated mouse prone 8 (SAMP8) mice. As outlined in section 1.8, the SAMP8 mouse strain is a widely accepted model for studying accelerated brain ageing and age-related cognitive decline and has been shown to suffer heightened levels of oxidative stress [202, 203]. Given that the existence of Cu enriched deposits within the SVZ has been previously established, the aim of this study was to determine whether an age-related increase in Cu occurs within the SVZ of SAMP8 mice, and if so, whether it is associated with elevated markers of oxidative stress.

4.2 RESULTS AND DISCUSSION

4.2.1 Copper Accumulates Within the Subventricular Zone in SAMP8 Mice During Ageing

As described in section 1.6, and demonstrated in chapters 3, XFM is capable of mapping the concentration and distribution of a wide variety of elements with sub-micron spatial resolution [102]. This is particularly useful for biological samples as it enables elemental analysis at a cellular level, and of relevance to this particular study, was used by Pushkar et al to observe the age-dependent Cu increase in astrocytes of the SVZ [65]. XFM elemental mapping analysis of SAMP8 lateral ventricles, and specifically assessment of Cu maps from the lateral ventricles of ≈1, 5, 9, and 12 month old SAMP8 mice highlighted an age-dependent accumulation of Cu in the SVZ, which was confirmed by statistical analysis (Figure 4.1).

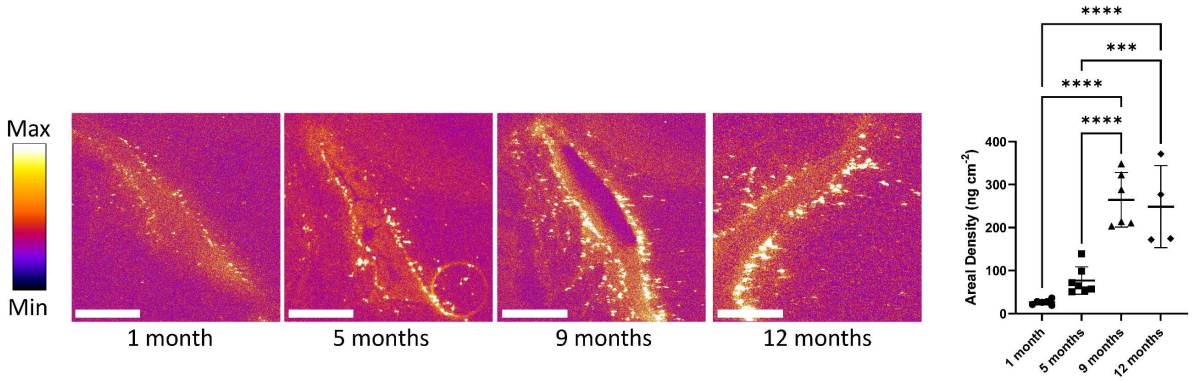

Figure 4.1: *XFM elemental maps of Cu in the SVZ of representative 1 month, 5 month, 9 month, and 12 month samples. False colour images were generated on the same scale to depict the increase in Cu over time from 1 month to 9 months, with a plateau at 12 months. This trend is also depicted in the plot on the right which indicates the statistically significant differences between regions of interest along the medial wall of the ventricle based on a one-way ANOVA (*** indicates p<0.001 and **** indicates p<0.0001). Scale bar = 200 µm.*

Interestingly, the increases in Cu content appeared to plateau during senescence and although Cu levels were significantly elevated in 12m mice relative to 1 and 5m mice, no difference in mean Cu content was observed between 9 and 12m time-points. There is a possibility that this increase in Cu from 1-9 months is developmental and the plateau with senescence is contributing to cognitive decline, however, considering its redox activity and the implication of oxidative stress in the ageing process, this study focussed on first investigating whether the excessive accumulation of Cu between 5m and 12m in this region is inducing oxidative stress.

4.2.2 XANES Analysis at the Sulfur K-edge Does Not Show Age-Related Elevation in Disulfide Levels Within the Subventricular Zone

Analysis of disulfide levels is a common approach for assessing oxidative stress in biological tissues. Thiol groups can be oxidised to disulfides via equation 4.1, so the abundance of thiol containing molecules and proteins within cells mean disulfide levels are expected to increase during oxidative stress.

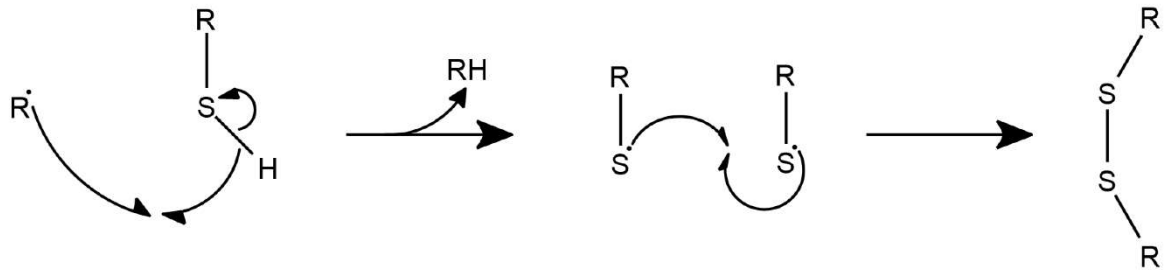

Equation 4.1: *Simplified mechanism for the free radical mediated oxidation of thiols to disulfides. Two thiol radicals generated from the first step can form a disulfide bond.* $R^{\cdot}$ *formation is promoted by metal ions through Fenton chemistry. It should be noted that stereochemistry is not accurately depicted.*

Cells typically contain high levels of glutathione as part of their antioxidant defence system [9], with the thiol group in the cysteine residue of glutathione reversibly oxidising to a disulfide during conditions of oxidative stress [204]. Additionally, the thiol group of cysteine residues in proteins is prone to oxidise and form disulfide bridges, often irreversibly during oxidative stress. XANES spectroscopy at the S K-edge is well suited to studying disulfide levels given its sensitivity to oxidation state, speciation, and geometry of S molecules [205]. This approach has previously been demonstrated for semi-quantitative determination of disulfide levels in animal tissues and cells (e.g., analysis of increased disulfide levels in the hippocampus after ischemic stroke), and a reference library of XANES spectra from biologically relevant S compounds has been developed by Hackett et al [103, 117, 127].

Micro-XANES spectra acquired from single points along the SVZ of 5m and 12m SAMP8 mice were fitted (least squares fitting) to the reference library of S model compounds, which revealed that for both age groups, S was predominantly in the form of thiols which is consistent with the abundance of cysteine residues and glutathione in the brain. This was followed by sulfonic acid in the form of taurine, then disulfides, and to a lesser extent, O-linked sulfate esters and sulfoxides. Interestingly, there was little to no contribution of thioethers to the fit suggesting that proteins in this region have a limited number of methionine residues. Further analysis using a one-way ANOVA surprisingly revealed no statistically significant differences in disulfide concentration between time points (figure 4.2).

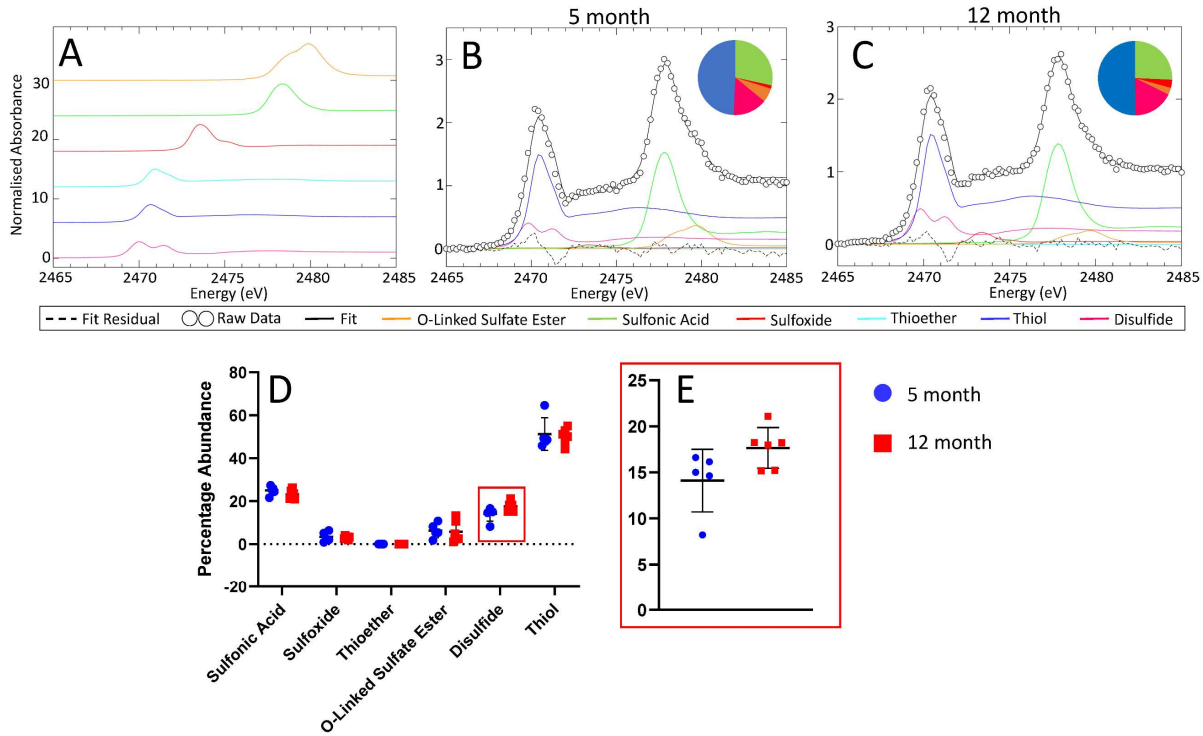

Figure 4.2: *Panel A shows S K-edge XANES spectra from model compounds that were collected previously by Hackett et al [103, 117, 127]. Spectra are staggered in the y axis for ease of viewing. Panels B and C show spectral fitting results of representative 5m (B) and 12m (C) spectra extracted from the medial wall of the lateral ventricles. Fitting was completed using EXAFSPAK software which uses least squares fitting. Panel D shows two-way ANOVA results comparing the percentage abundance of each model compound between the two time points based on the least squares fitting results. No statistically significant differences ($p<0.05$) between time points were observed for any of the compounds. Panel E depicts the relative abundance of disulfides (the key marker of oxidative stress) for the two time points.*

The use of μXAS is useful for obtaining full XAS spectra from specified sample regions, however, as outlined in table 1.3 of section 1.6.5, the time constraints associated with full spectrum collection per point, mean only a small region of the total sample is analysed. Specifically, if the length of the wall of the SVZ is approximately 900 μm (based on length measurement of a ventricle image), with a width of approximately one cell (20 μm), then collection of 5 μXAS spectra per animal, with a beam-spot size of 10 x 10 μm, equates to analysis of only 0.3 % of the tissue region of interest. Therefore, chemically specific XFM was used to image the relative abundance of disulfides across a larger sample region. This approach involved collecting a single image at the white line feature of specific S species (e.g., thiols, disulfides.etc), to show their distribution and abundance across a larger area of the ventricle. While collecting images from only single energy points can increase potential error associated with background interference and fluctuations in beamline energy calibration, the results from analysis of the fluorescence intensity agreed well with μXAS analysis and demonstrated no statistically significant differences in disulfides between time points (Figure 4.3).

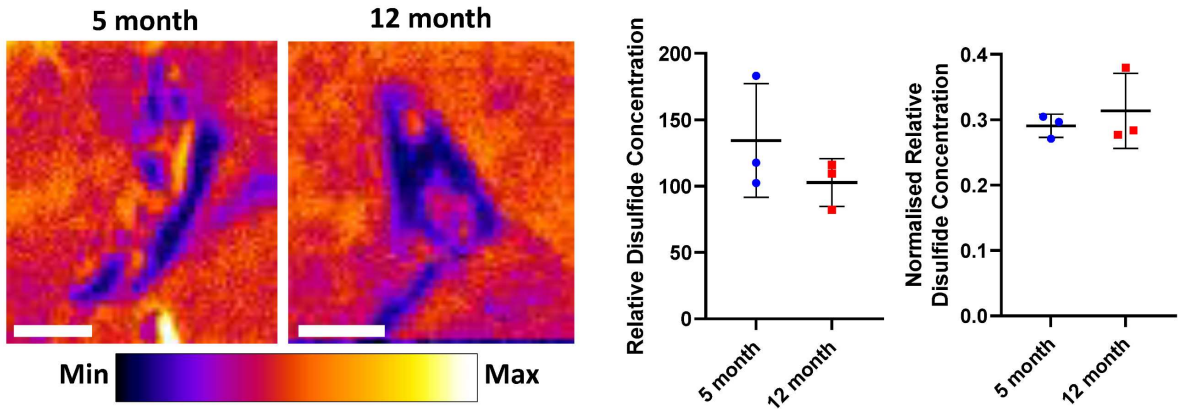

***Figure 4.3**: S XANES maps of the lateral ventricles showing the distribution of disulfides in representative 5m and 12m samples. False colour images were generated on the same colour scale for direct visual comparison of disulfide concentration. The similarity in images does not indicate any significant differences which was supported by the statistical analysis depicted on the right. For the left plot, the fluorescence intensity was extracted from a region of interest along the wall of the ventricle in the disulfide image and compared using a Student's t-test to confirm there was no statistically significant difference ($p<0.05$) between the two age groups. The normalised values were obtained by dividing the disulfide XANES image by the total S XANES image, then extracting the fluorescence intensity from regions of interest as described*

above. The normalised data also displayed no statistically significant differences between age groups based on a Student's t-test. Scale bar = 200 μm.

The lack of increase in disulfides was surprising when considering the substantial increase of Cu in this region during ageing. While there does appear to be a subtle (but not significant) increase in mean disulfide content at 12m based on both the μXAS, and normalised chemically specific XFM data, the results are not consistent with the level of Cu induced oxidative stress expected with respect to the magnitude of Cu increase observed across the 5m – 12m mice. To specifically quantify the expected increase in disulfide content, the equivalent concentration of Cu (equivalent to the magnitude of Cu increase observed across 5m to 12m old mice) was added to brain homogenates and the disulfides measured using a glutathione detection assay. The magnitude of the Cu increase across mice aged 5m – 12m was determined using the average Cu areal density calculated for the SVZ, tissue section thickness, and assuming a density similar to that of water (in frozen tissue). Using these criteria, the magnitude of the Cu increase from mice aged 5m to 12m in the SVZ was calculated to be ≈3 mM. If the region of interest was restricted to specific cellular Cu accumulations (Cu "hot spots"), the magnitude of the Cu increased was determined to be ≈17 mM. When these levels of Cu (3 mM or 17 mM) were added to brain homogenates, there was a drastic disulfide increase, which supports the known propensity for Cu ions to catalyse free radical production and drive molecular oxidation. Interestingly, a significant difference in disulfide levels was not observed between addition of 3mM or 17 mM Cu (Figure 4.4), possibly indicating rapid depletion of oxidative substrate (e.g., thiols) occurs with a 3 mM increase in Cu. On average, the addition of 3 mM Cu resulted in a ≈33% average increase in disulfides in brain homogenates, which is in stark difference to the lack of significant change in disulfide levels observed when Cu increases to a similar magnitude in brain tissue.

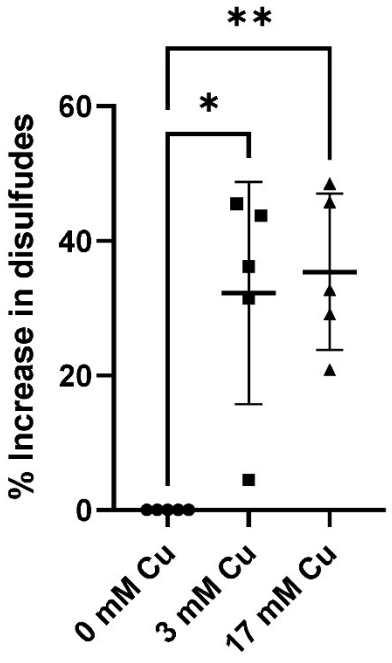

Figure 4.4: Results from a one-way ANOVA comparing the *percentage increase in disulfides relative to the control (0 mM) based on a glutathione detection assay (* indicates p<0.05, ** indicates p<0.01). The decrease in glutathione relative to the control was attributed to the formation of disulfides.*

4.2.3 FTIR Analysis of Lipid Unsaturation, Aldehydes, and Protein Aggregates Does Not Support an Association Between Age-Related Subventricular Copper Increase and Oxidative Stress

As described in section 1.7.1, Fourier transform infrared microscopy is advantageous for the analysis of biological tissues given the wide variety of functional groups it can detect. Of interest to this study is its ability to measure markers of oxidative stress. Oxidative stress can induce lipid peroxidation resulting in reduced unsaturation of lipids and the formation of short chain aldehydes [27, 206]. This can be monitored in an FTIR spectrum using the olefinic CH stretching peak (3012 cm^{-1}), and the carbonyl stretching of aldehydes (1715cm^{-1}). Protein aggregation and formation of aggregated β-sheets can also occur during oxidative stress [207, 208] when amino acid side chains are oxidised. Relative abundance of protein secondary structures can be inferred through inspection of the amide I band (1600-1700cm^{-1}), specifically examining the amide-carbonyl stretch of α-helices and aggregated β-sheets at ≈1656 cm^{-1} and ≈1627 cm^{-1}, respectively. Given the surprising failure of XAS at the S K-edge to detect an increase in markers of oxidative stress (e.g., disulfides) in association with

substantial brain Cu increases, FTIR microscopy was used to test for the presences of additional markers of oxidative stress (lipid oxidation products and protein aggregates).

Synchrotron FTIR mapping was undertaken across a cross-section of the lateral ventricles from SAMP8 mice aged 5m and 12m. Spectra were extracted from the SVZ of the medial and lateral side of the ventricles and a comparison of the IAUC for the three peaks of interest were compared across time points. Results are summarised in figure 4.5, and interestingly, show no significant elevation in any markers of oxidative stress. The olefinic CH stretching peak was in fact observed to increase in the 12m mice, and although there was an increase in the overall area of the carbonyl band (integrated band area from 1710 – 1755 cm^{-1}) in 12m mice, the increase was shown to be the result of increased abundance of lipid esters (carbonyl band centred at 1735 cm^{-1}), and not the aldehyde carbonyl functional group (centred at 1715 cm^{-1}).

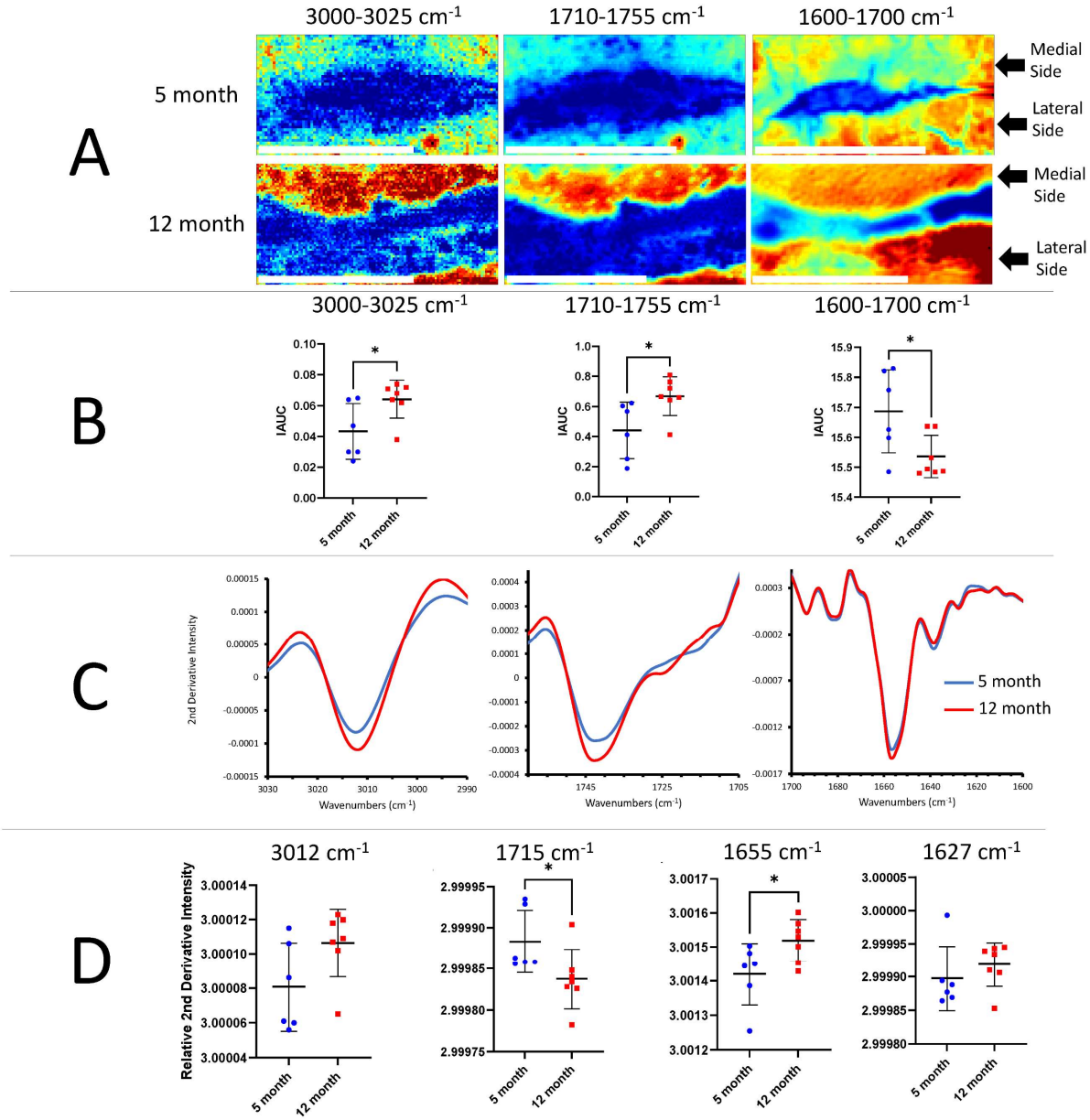

***Figure 4.5**: Panel A depicts representative FTIR images showing the IAUC for 3 markers of oxidative stress. 5m and 12m comparisons are set to the same colour scale. Panel B shows results of unpaired Student's t-tests comparing the IAUC for spectra from the medial wall of the lateral ventricles between time points (* indicates 0.01<p<0.05). Panel C displays normalised (1600-1700 cm^{-1}), second derivative spectra of key regions of interest, and panel D outlines the results of unpaired Student's t-tests comparing second derivative intensities for key peaks of interest (* indicates 0.01<p<0.05). Given that lower values in second derivative spectra indicate a higher concentration, the intensity values have been inverted (multiplied by -1 then added 3) for ease of viewing.*

While these results could suggest altered lipid metabolism from 5m to 12m, they do not support elevated levels of lipid peroxidation. Interrogation of the amide I band showed increased intensity at 12m for α-helix protein structure, and no significant difference in the abundance of protein β-sheet aggregates between time points. Therefore, while there does appear to be an altered biochemical profile between the 5m and 12m SAMP8 mice, the results are not consistent with elevated levels of oxidative stress in the SVZ.

Similar to the strategy used to study disulfides, in addition to FTIR analysis of tissue sections, bulk ATR-FTIR analysis was undertaken for brain homogenates with and without the addition of Cu that matched the Cu concentration increase in brain tissue (average increase of 3 mM in SVZ, and 17 mM in hotspots). Consistent with what was observed when the same experiment was completed for disulfide analysis, the FTIR results demonstrated the propensity for this level of Cu to catalyse free radical production, resulting in lipid peroxidation (increased aldehydes), and protein aggregation (increased protein β-sheet aggregates). In contrast to the disulfide analysis, the magnitude of increase in oxidative stress markers appeared to reflect the magnitude of increase in Cu, with the 17 mM addition causing significantly elevated levels of aldehydes and aggregated proteins compared to both the control (0 mM Cu) and 3 mM Cu additions (Figure 4.6). Interestingly, the amide I band revealed that with a 3 mM Cu addition the α-helix protein structures (1656 cm^{-1}) appear to be converted to unordered protein structures (1631 cm^{-1}), but with a 17 mM addition, the α-helix protein structures appear undisrupted. The absence of a significant signal from unordered protein structures in the spectrum following addition of 17 mM Cu suggests that it is likely these structures that are converted to protein aggregates (1627 cm^{-1}) in the presence of higher Cu concentrations rather than the α-helix structures. These results could also suggest that during oxidative stress, unordered proteins may increase prior to complete aggregation. In addition to the aldehydes and protein aggregates, the unsaturated lipids also appeared to increase significantly with additional Cu, and while oxidative stress typically reduces lipid unsaturation, it is possible that unsaturated short chain aldehyde products of lipid peroxidation can be attributed to the increase. Overall, it was evident that the presence of Cu in equivalent concentrations to the increase observed in the SVZ of tissue sections during ageing, was sufficient to increase markers of oxidative stress in brain homogenates.

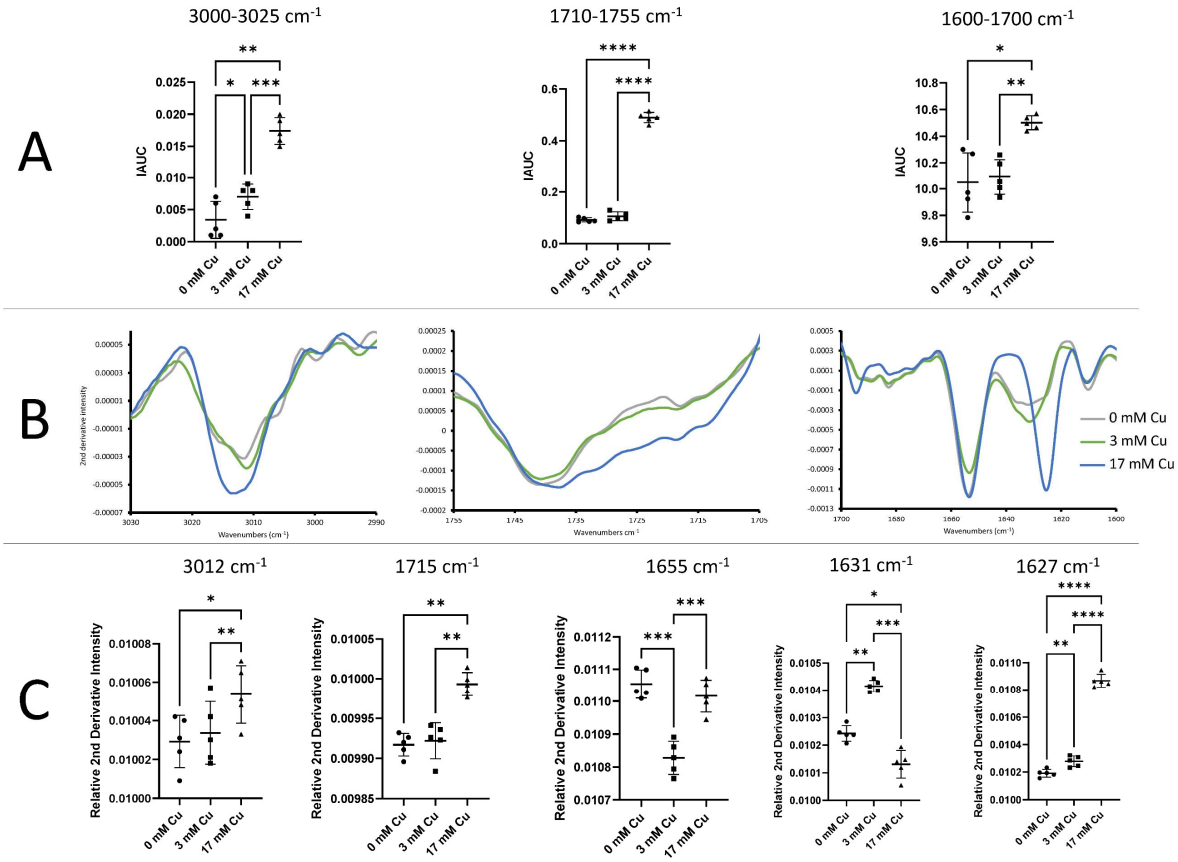

Figure 4.6: *Panel A shows results of unpaired Student's t-tests comparing the IAUC from ATR-FTIR spectra from brain homogenates with varying concentrations of Cu. Panel B displays normalised (1600-1700 cm^{-1}), second derivative ATR-FTIR spectra from brain homogenate samples, and panel C outlines the results of unpaired Student's t-tests comparing the second derivative intensities for key peaks of interest. Given that lower values in second derivative spectra indicate a higher concentration, the intensity values have been inverted (multiplied by -1 then added 0.01) for ease of viewing.*

4.2.4 Age-Related Brain Copper Increase Does Not Associate with Increased Markers of Oxidative Stress in SAMP8 Mice

This study has unexpectedly shown that the significant age-related accumulation of Cu in the SVZ of SAMP8 mice does not occur concomitantly with elevation in spectroscopic markers of oxidative stress (increased total disulfides, lipid oxidation products, or β-sheet aggregates). The possibility that oxidative stress was present *in vivo* however, can not be ruled out. It is possible that elevated markers of oxidative stress were present in 12m samples but were below the detection limits of the chosen techniques (on the order of μM to hundreds of μM for FTIR and XANES). The potential impact of sample preparation on results should also be considered, such as the possibility for air dried sections to have increased markers of oxidative stress. Although the detection limits and sample preparation are important factors to consider, FTIR and XANES spectroscopy have been used previously on air dried tissue sections for successful detection of markers of oxidative stress associated with ischemic stroke, haemorrhagic stroke, AD, and brain ageing in white matter [81, 113, 171, 209]. Furthermore, when Cu at a concentration equivalent to the increase observed from 5m to 12m was added to brain homogenates, significant elevation in disulfides, aldehydes, and β-sheet aggregates was observed. Therefore, although this study can not conclusively conclude that the age-related Cu increase has not resulted in heightened oxidative stress, it can conclude that a significant proportion of the accumulated Cu is not actively driving oxidative stress in the SVZ.

The lack of oxidative stress observed in this study could be attributed to antioxidant defences present within tissue, including enzymes and proteins such as catalase, glutathione peroxidase, SOD, and metallothionein, that can scavenge oxidants and minimise production of the measured oxidative stress markers [30, 210-212]. Alternatively, the findings may also suggest that the Cu is in a chemical form that does not readily induce oxidative stress. Pushkar et al completed XANES analysis and identified that the Cu is likely in a Cu(I) oxidation state bound to cysteine in an environment similar to that modelled by Cu-metallothionein (a Cu(I)-thiolate multimetallic cluster) [65]. Metallothioneins are capable of reversibly binding up to 7 divalent metals, or up to 12 monovalent metals via cysteine residues, and are secreted by astrocytes [9]. Interestingly, metallothionein expression increases with increasing Cu concentration [9] and it is possible that this is a protective mechanism to prevent Cu mediated oxidative stress or non-specific protein binding. Specifically, while the binding is generally reversible, the Cu may

become less exchangeable as its concentration increases, thereby preventing redox reactions that produce ROS and trigger oxidative stress. Metallothioneins have been proposed to play an important role in controlling Cu homeostasis [9], which agrees with the lack of evidence to support Cu induced oxidative stress demonstrated in this study, taken with the Cu-metallothionein complexation identified by Pushkar et al [65].

Although the work by Pushkar et al suggested that the speciation of Cu within Cu accumulations of the SVZ is likely from Cu complexed to metallothionein, this was based on the resemblance of the Cu K-edge XANES spectra to Cu(I)-thiolate multimetallic complexes. Although consistent with metallothionein, multimetallic thiolate complexes could also be indicative of other metalloproteins, such as the Cu chaperone Cox17 to provide one example [65]. The effect of sample preparation should also be considered when taking into account Cu K-edge XANES that are reported in the literature. As stated previously, Pushkar et al [65] suggests Cu coordinated to thiolates, which is highly plausible, but it is also possible that the air drying process has resulted in altered coordination environments. Change in metal ion speciation during air drying was observed for Zn, when comparing Zn K-edge XANES spectra between air dried and flash frozen tissue analysed with a cryostream, and a similar effect can not be ruled out for Cu [169].

To further investigate the possibilities, it would be worth repeating the Cu XANES studies not only to confirm that the coordination in the SAMP8 model is consistent with what was observed by Pushkar et al in the Sprague Dawley rats, but to follow from their work and further characterise the proposed Cu binding environment. Comparison of SAMP8 Cu XANES spectra to an extensive library including Cu bound to S in other proteins or complexes would be useful to identify the percentage contribution of each of these biologically relevant Cu complexes. Additional studies should also include subcellular elemental mapping to identify the exact subcellular location of the Cu accumulations within the SVZ. There is strong evidence in the literature supporting mitochondria in a role for maintaining Cu homeostasis, specifically through Cytochrome c oxidase and SOD1 [213]. Within the mitochondria these enzymes are localised to the intermembrane space, so given that the majority of Cu in the mitochondria is stored within the matrix, transporters are required to deliver it to the intermembrane space and subsequently to the enzymes [213]. Interestingly, given the lack of Cu-proteins localised to the matrix based on previous studies, it is proposed that the matrix stored Cu is exchangeable

and bound to currently unidentified low molecular weight ligands, that also deliver the Cu to the intermembrane space [213, 214]. Importantly, the matrix Cu pool has been shown to increase with higher Cu concentrations in cultured cells [215]. It is therefore worth considering that the Cu accumulation around the lateral ventricles may be occurring within the mitochondrial matrix, with an elevated load of Cu coordinated to thiol-containing ligands. If this is the case, the lack of oxidative stress markers observed in this study, could be explained by increased expression of mitochondria metalloproteins and low molecular weight Cu complexes in sufficient abundance to ensure the Cu remains bound and unable to react to form ROS. Future elemental mapping and XANES studies at subcellular resolution, in flash frozen tissues are now needed to explore this area further.

Another important observation in this study was that the Cu concentration did not increase between 9 and 12m, indicating that the difference observed between adult (5m) and old (12m) mice may be from Cu accumulation during brain development (1-5 months) and adulthood (5-9 months). This highlights the importance of time course studies that consider multiple senescence points for gaining an overall understanding of the processes occurring during ageing. Specifically, they can help to ensure that biochemical and metallic alterations are more accurately attributed to either natural ageing and development, or disease. For example, when considering only the 5m and 12m time points, one could conclude that the accumulation of Cu seen in 12m samples is contributing to cognitive decline. However, when one considers the full time course, it becomes evident that Cu actually increases at earlier time points, and it is entirely possible that the plateau effect and a deficiency of Cu (relative to the increasing trend) at 12m is what is contributing to age-related cognitive deficits. Future studies should therefore consider the role that Cu has in brain development, and ideally, multiple time points should be used for thorough analysis.

4.3 CONCLUSION

In summary, this chapter has confirmed that the age-dependent accumulation of Cu in the SVZ that has been observed in other rodent strains is also evident in SAMP8 mice. Specifically, the accumulation occurs during brain development and adulthood, and interestingly, plateaus from 9 to 12m. Surprisingly, the significantly elevated levels of Cu at 12m do not appear to elevate spectroscopic markers of oxidative stress in the SVZ, as there was no apparent increase in thiol oxidation products (XANES analysis), lipid peroxidation products, or protein aggregates (FTIR analysis). While these findings do not conclusively rule out the possibility of Cu causing increased oxidative stress in the SVZ, they do suggest that there are mechanisms in place to minimise or prevent Cu mediated generation of ROS and subsequent oxidative damage. When considering that elevations in redox active metals are often linked with heightened oxidative stress, this finding is significant and should be considered when interpreting elevations in both Cu and Fe. Evidently, increases in redox active metals may not always lead to oxidative damage which is important in the context of ageing and neurodegenerative disease. Further studies are required to identify the exact subcellular location, and specific chemical forms of Cu in this region, and additional mechanistic studies to identify whether the Cu accumulation is natural, protective, or has pathological consequences should be considered. Further understanding the cause and consequences of altered Cu homeostasis during ageing, may help to reveal mechanisms contributing to cognitive decline, and in turn reveal pathways for improving brain health during ageing.

Chapter 5: Development of a Multi-Modal Microscopy Approach for the Analysis of Neurons and Glia

ABSTRACT

An understanding of brain biochemistry at a cellular level is vital for determining mechanisms that may contribute to brain disease and neurodegeneration. This requires suitable methods capable of revealing a wide range of chemical information. Multi-modal imaging approaches are promising, because techniques that are typically suited for detecting specific markers can be used in combination with others to expand the information obtained from a single sample. A challenge in developing such approaches often lies in the different sample preparation requirements for each technique. For example, immunohistochemistry, an invaluable technique for detecting antigens and proteins within tissue structures, requires chemical fixation techniques that are known to alter the distribution and chemical state of some species in tissue, and increase propensity for tissue fluorescence. Fortunately, spectroscopic methods enable direct detection of a range of chemical species (depending on the incident wavelength) with minimal sample preparation requirements. Raman microscopy using UV or visible lasers is particularly useful for cellular and subcellular analysis because it enables imaging with sub-micron diffraction limited spatial resolution. Unfortunately, fluorescence signals can interfere with Raman spectra, so the natural autofluorescence of tissue has limited widespread adoption of this technique for *in situ* analysis. This chapter will describe an investigation into the effect of sample preparation protocols on tissue autofluorescence and describe a method for minimising autofluorescence in Raman spectra allowing for analysis of subcellular organelles. Additionally, it will describe a method that enables spectroscopic and immunohistochemical analysis of the same tissue section using immersion fixation, which is demonstrated for tissue imaged by Raman microscopy, and X-ray fluorescence microscopy. In summary, this chapter describes a unique multi-modal workflow that enables visualisation of endogenous tissue autofluorescence, Raman or XFM biochemical/metal images, and specific immunofluorescence markers of cell type.

5.1 INTRODUCTION

The study of brain biochemistry is important not only for understanding the processes associated with healthy brain function, but also alterations that occur during brain disease and neurodegeneration. Better understanding of the processes that occur at a cellular level in healthy and diseased brain states could pave the way for development of targeted therapeutics and preventative measures for various brain disorders. While there are several useful methods available for studying cell biochemistry, they are typically suited for detecting specific markers. Ideally, multi-modal approaches that enable a wider scope of information to be obtained should be developed. A challenge with developing such approaches is the variation in sample preparation protocols required for each technique.

Immunohistochemistry, as described in section 1.7.2, is a technique that can identify specific cell types or subcellular organelles based on antigen and antibody binding [142, 157]. Successful immunofluorescence staining requires chemical fixation to ensure proteins (antigens) are immobilised and that the integrity and morphology of tissue structures (i.e., cells) is maintained [157]. Unfortunately, chemical fixation steps are known to alter the natural chemical environment, meaning techniques that analyse specific biochemical markers may provide misleading results when applied to fixed tissue. For example, chemical fixation of brain tissue is known to redistribute labile pools of Zn and perturb Zn speciation, impacting techniques such as XFM and XAS [169, 170, 172, 216]. This makes coupling immunohistochemical methods with direct techniques challenging and indicates the importance of analysing unfixed tissue when trying to probe cellular biochemistry.

Spectroscopic imaging techniques are advantageous as they enable direct, typically non-destructive analysis of biological tissue with minimal sample preparation requirements (i.e., analysis of unfixed tissue is possible). Raman microscopy is particularly suited to studying subcellular biochemistry because the use of UV and visible lasers offers direct biochemical detection with sub-micron diffraction limited spatial resolution. These capabilities have been utilised by numerous research groups to study the biochemical composition of subcellular organelles such as the nucleus [217], nucleolus [218], and mitochondria [219], including applications to cultured brain cells [220, 221]. Unfortunately, while it is a powerful technique, there are much fewer reported applications of Raman microscopy to study brain cells *in situ* within brain tissue sections.

One possible reason for this is the autofluorescence from endogenous fluorophores in tissues that have been considered to prevent or hinder the collection of Raman data using shorter wavelength lasers. Longer wavelength lasers in the red or near-infrared have been used to combat tissue autofluorescence, however these provide weaker Raman scattering signal and poorer diffraction limited spatial resolution [222-224]. Despite the limitations associated with tissue autofluorescence, endogenous fluorophores can be chemically and anatomically informative. Several studies have used differences in tissue autofluorescence for preliminary differentiation of healthy tissue from cancerous tissue, which then enabled specific regions of interest to be defined for subsequent Raman analyses [225, 226]. In addition, the strong autofluorescence of amyloid-β plaques has been previously used to define plaque location in AD brain tissue prior to Raman analyses [81, 146].

Some common sources of endogenous fluorophores in brain tissue include NADH, flavins, heme-moieties, phospholipids, and collagen [227-229]. In addition, lipofuscin, a cellular waste product that has been implicated in disease and neurodegeneration processes, displays strong autofluorescence across a broad range of wavelengths [227, 230, 231]. Unsurprisingly, sample preparation steps such as chemical fixation can also hinder Raman measurements by increasing propensity for fluorescence [227, 229, 231]. Interestingly, the extent to which sample preparation may influence tissue autofluorescence signals in Raman spectra collected with green light excitation from brain tissue has not been extensively studied. Additionally, there has been limited investigation into whether suitable sample preparation may enable both endogenous autofluorescence and Raman signals to be measured simultaneously.

This chapter identifies that tissue autofluorescence increases as a function of time post tissue sectioning and describes an optimised protocol to minimise autofluorescence for Raman analysis and enable complementary fluorescence microscopy of the same cell. This protocol was subsequently combined with post-fixation to allow immunohistochemical analysis, leading to a workflow that includes Raman analysis, fluorescence microscopy, and immunohistochemistry of the same tissue section. The transferability of this protocol was then confirmed after successful application to tissue that had been imaged using XFM. In summary, this chapter describes a unique multi-modal workflow that enables visualisation of endogenous tissue autofluorescence, Raman or XFM biochemical/metal images, and specific immunofluorescence markers of cell type.

5.2 RESULTS AND DISCUSSION

5.2.1 Raman Microscopy and Fluorescence Microscopy Demonstrate Tissue Autofluorescence Increases as a Function of Time After Tissue Sectioning

5.2.1.1 Fluorescence Microscopy

Fluorescence microscopy was used to monitor tissue autofluorescence in the granular layer, molecular layer, and white matter of rat cerebellum tissue, following excitation with UV, blue, and green light. These experiments were prompted by previous time-dependent observations of tissue autofluorescence observed from green light excitation of brain tissue [81]. Fluorescence images were collected across three excitation/emission ranges, UV/blue, blue/green, green/red, as shown in Figure 5.1.

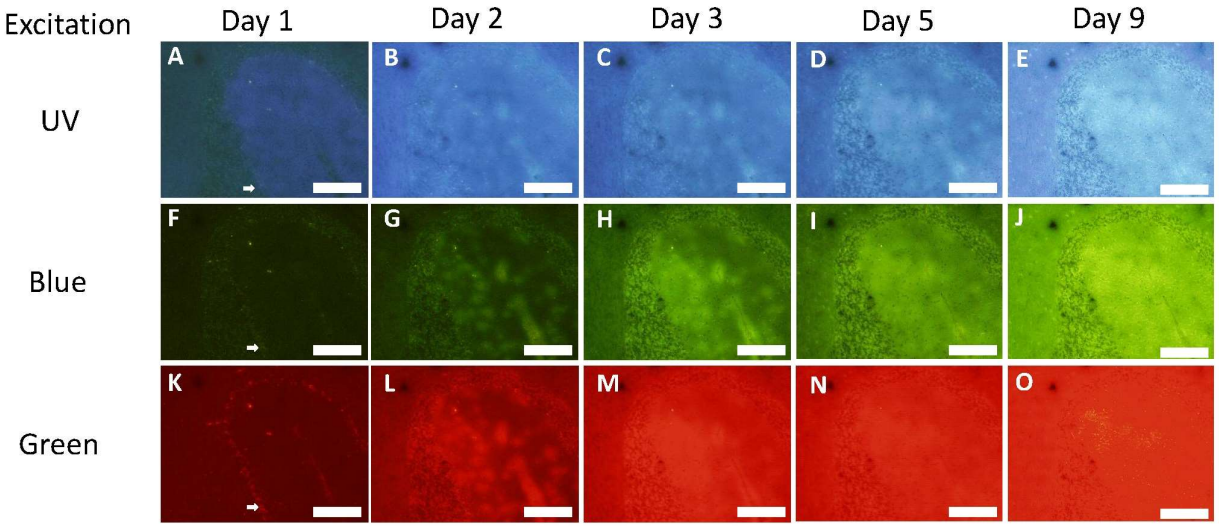

Figure 5.1*: Fluorescence microscopy images of endogenous tissue autofluorescence captured from the same 10-µm thick cerebellum tissue over a 9 day time course post tissue sectioning. Images were captured with 10x magnification with 3 different excitation energies and emission filter pairings: UV λ_{ex}=375/28 nm (LP λ_{em}=435 nm), blue λ_{ex}=465/15 nm (LP λ_{em}=515 nm), green λ_{ex}=530/40 nm (LP λ_{em}=590 nm). All images along a row have been thresholded to the same min and max fluorescence intensity value, to highlight the quantitative increase in fluorescence that occurs as a function of time post tissue sectioning. Scale bars represent 200 µm.*

It would be expected that the fluorescence images collected with green excitation and red emission, would mirror the data obtained via Raman microscopy with excitation using green lasers at 514 nm or 532 nm (discussed in next section). As can be seen in the fluorescence images (Figure 5.1) and statistical analysis (Figure 5.2, p-values in appendix tables 1, 2, and 3)

a strong time-dependent increase in tissue autofluorescence was observed across all excitation / emission pairings, and for all three tissue regions (granular layer, molecular layer, and white matter).

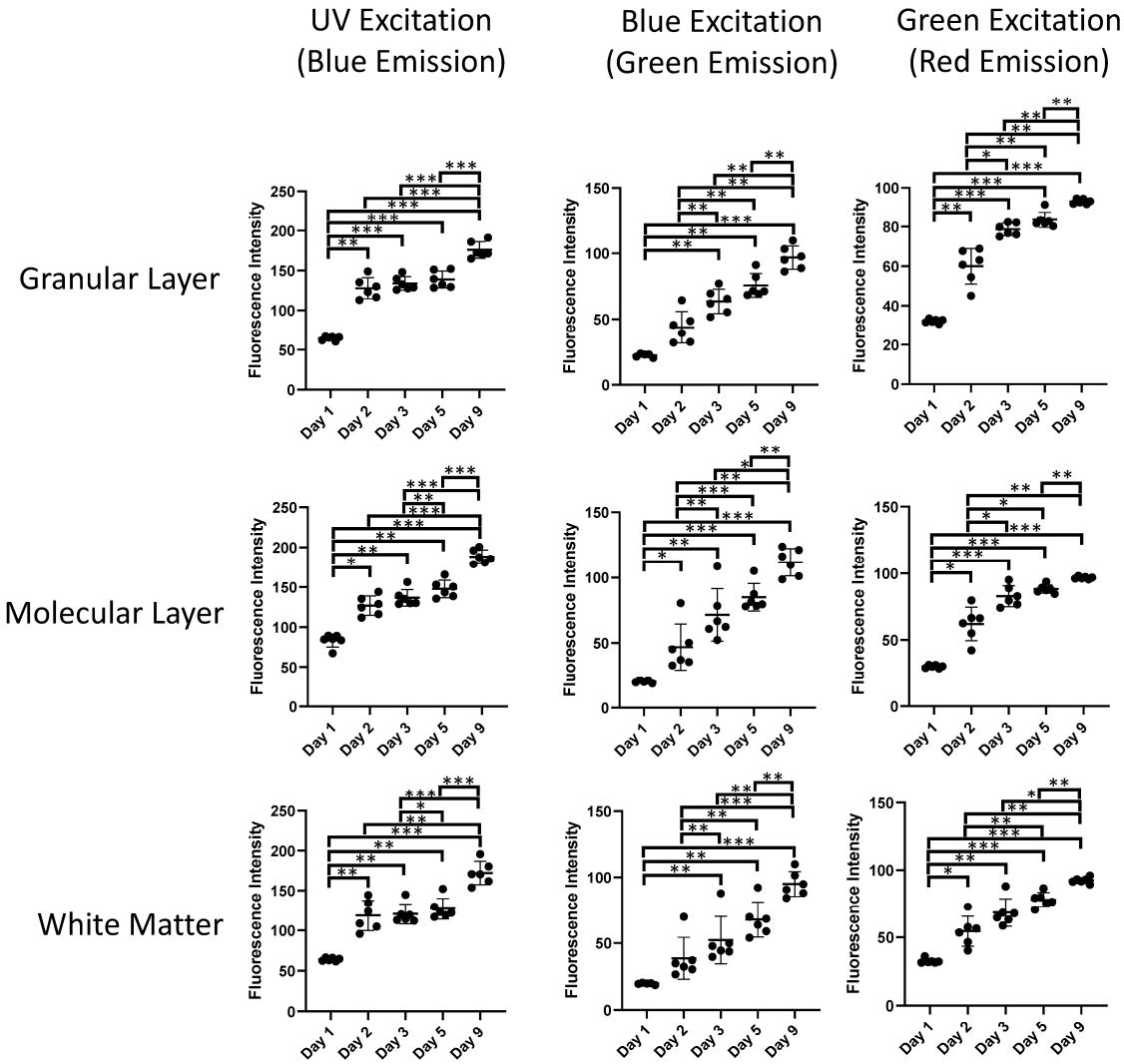

Figure 5.2*: Quantitative analysis of the increase in fluorescence intensity that occurs as a function of time post tissue sectioning, in specific regions of interest (white matter, granular layer and molecular layer). Statistically significant differences based on repeated measures one-way ANOVAs, with multiple comparison testing are indicated with asterisks (*p≤0.05, **p≤0.01, ***p≤0.001).*

Interestingly, the relative distribution of tissue autofluorescence differs as a function of time after tissue sectioning. Specifically, in freshly cut tissue sections (i.e. day 1 samples) numerous small subcellular deposits that show strong autofluorescence can be observed in the Purkinje neurons of the cerebellum (Figure 5.1 A, F, K, white arrows). These subcellular

autofluorescent deposits are attributed to lipofuscin based on their broad-band emission [232, 233]. Further, the Purkinje neurons of the cerebellum are excitatory neurons that are post-mitotic (i.e. do not undergo cell division) and known to readily accumulate lipofuscin [233-239]. The lipofuscin deposits become increasingly difficult to observe in tissues imaged at subsequent times post-tissue sectioning (e.g., Day 2 to Day 9) due to the pronounced overall increase in autofluorescence across all tissue regions.

5.2.1.2 Raman Microscopy

Raman spectroscopic analysis of biological tissue often utilises visible lasers to enhance spatial resolution and increase signal to noise, but often this is at the expense of increased autofluorescence compared to data collected at longer excitation wavelengths (e.g., red, near-infrared) [222]. This study examined the autofluorescence signal that is obtained from three different regions of brain tissue (white matter, granular layer, molecular layer)[21], and determined how the autofluorescence signal changes as a function of time after tissue sectioning. Two sets of measurements were completed, using a confocal Raman microscope with excitation at 532 nm, and a dispersive Raman microscope with excitation at 514 nm. As can be seen from Figure 5.3, there is a dramatic time-dependent increase in tissue autofluorescence that occurs in all tissue regions as a function of time after tissue sectioning (p-values in appendix tables 4 and 5). The magnitude of the time-dependent increase in autofluorescence was less severe in tissues collected with excitation at 532 nm (confocal Raman microscope, Figure 5.3A-F) when compared to excitation at 514 nm (dispersive Raman microscope, Figure 5.3G-L).

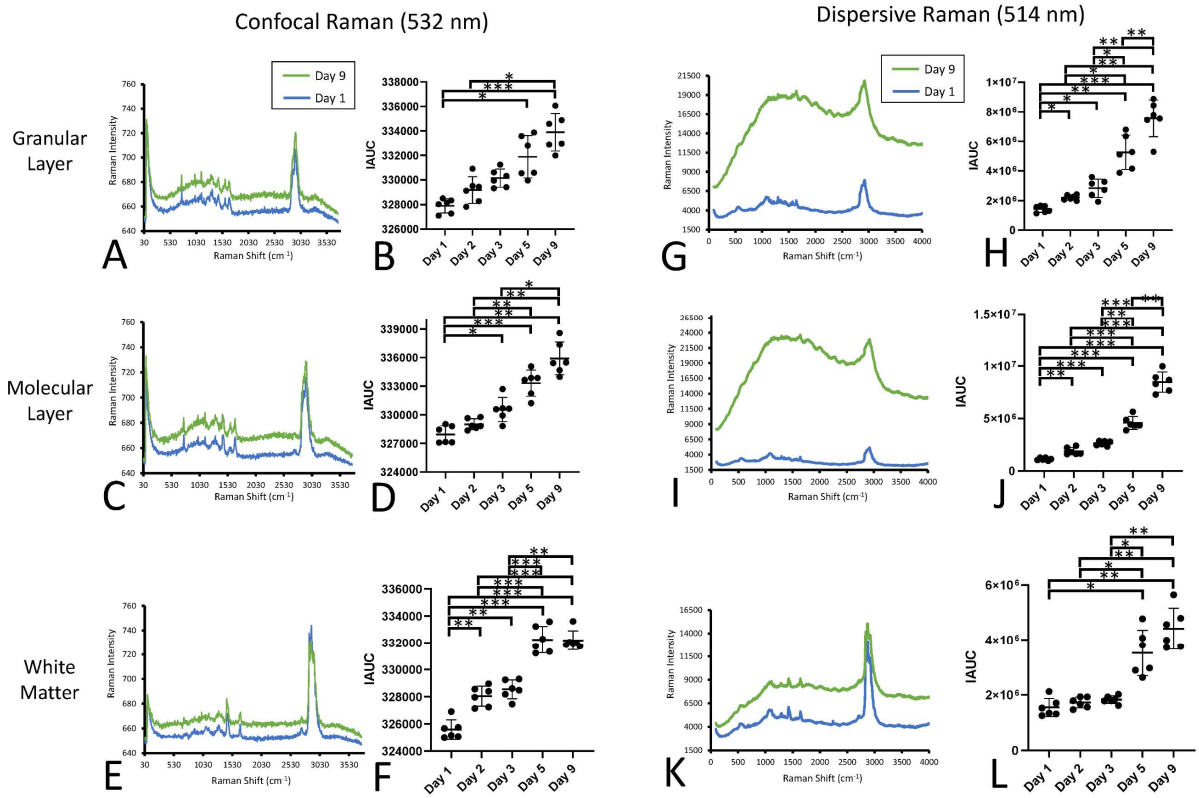

***Figure 5.3**: Quantitative analysis of the increase in autofluorescence intensity measured with confocal Raman microscopy (532 nm excitation, A-F) or dispersive Raman microscopy (514 nm excitation, G-L) that occurs as a function of time post tissue sectioning, for specific regions of interest within cerebellum tissue: granular layer (A,B,G,H), molecular layer (C,D,I,J), and white matter (E,F,K,L). Representative Raman spectra showing the time dependent increase in fluorescence intensity are shown for tissues on day 1 and day 9 post tissue sectioning (A,C,E,G,I,K). The relative autofluorescence was measured by integrating the autofluorescence baseline (2000-2500 cm^{-1}), which corresponds to a fluorescence emission of 595.3-613.6 nm (for 532 nm excitation) and 572.9-589.8 nm (for 514 nm excitation). Statistically significant differences (B,D,F,H,J,L) between the IAUCs based on repeated measures one-way ANOVAs with multiple comparison testing are indicated with asterisks (*p<0.05, **p< 0.01 >, ***p< 0.001).*

These differences could be explained by the different excitation wavelengths used, which possibly excite different fluorophores, however, it is most likely the result of the difference in laser power between the two instruments and the presence of photo-bleaching occurring on the confocal Raman microscope, which used high photon flux. Further, although the fluorescence signal is retained on the dispersive Raman microscope, the fluorescence signal

is rapidly photobleached (within seconds) on the confocal Raman microscope as shown in Figure 5.4).

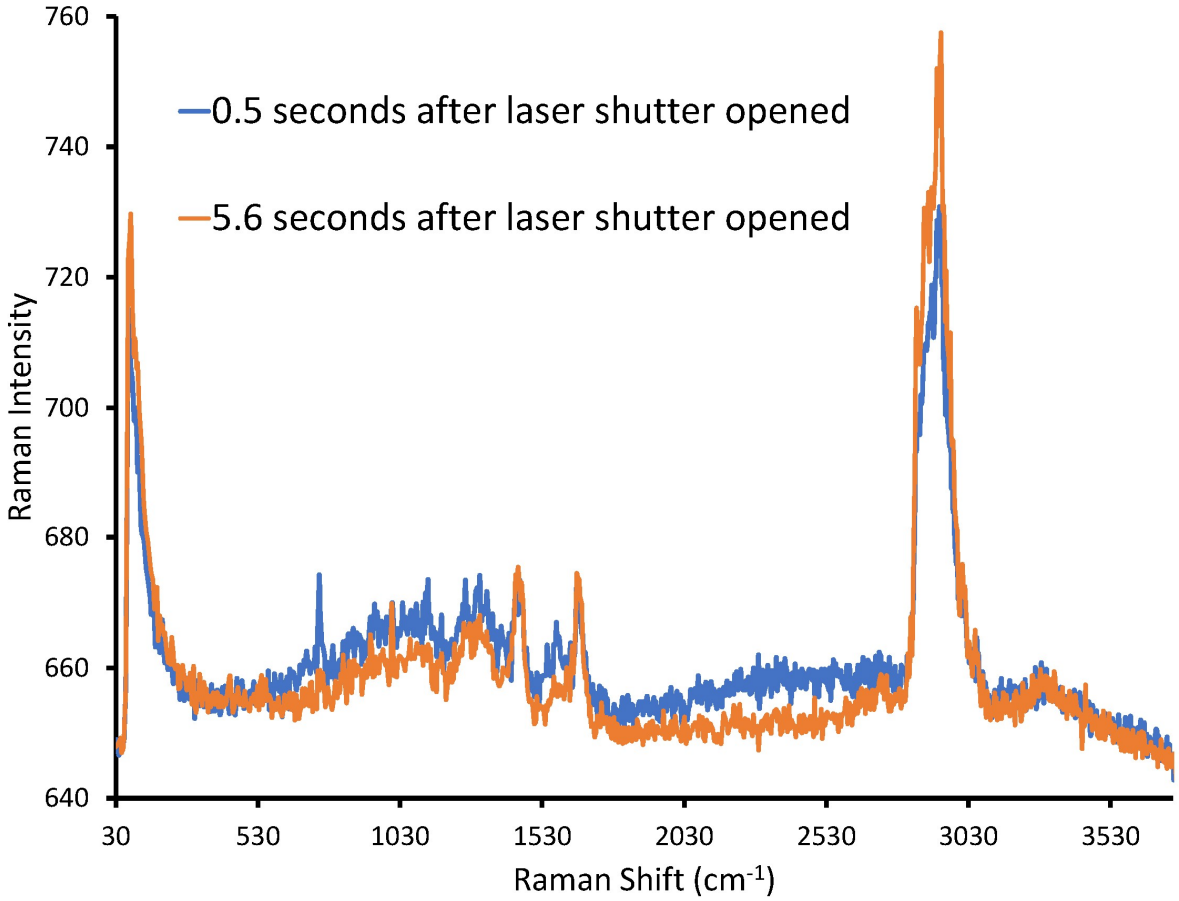

***Figure 5.4**: Representative spectra collected from cerebellum tissue using a confocal Raman microscope showing the difference in fluorescence signal before and after photobleaching. The fluorescence signal is reduced within 6 seconds of the laser shutter opening.*

For both data sets (excitation at 532 nm and 514 nm), the most pronounced differences were observed in the granular and molecular layers, relative to the white matter layer. As a consequence of the large autofluorescence increase in the granular and molecular layers, Raman scattering peaks in the fingerprint region are almost completely masked in spectra from these regions 9 days after sectioning when using 514nm excitation. The difference in response between the granular and molecular layers relative to the white matter could be attributed to the inherently different biochemical composition of these layers. The granular layer of the cerebellum is rich in cell bodies (soma), and the dendrites of the neurons project into the molecular layer [240]. Therefore, both the granular layer and molecular layer contain a substantial amount of molecules involved in neuronal activity, some of which may be

endogenous fluorophores. In contrast, the white matter is less chemically complex, containing mainly myelinated axons [240].

Taken together, the results of fluorescence microscopy and Raman microscopy clearly indicate that a strong time-dependent increase in tissue autofluorescence occurs after tissue sectioning. Indeed, the increased autofluorescence in Raman microscopy data collected with 514 nm excitation occurs to such an extent that Raman scattering is completely masked. Somewhat surprisingly though, relatively minimal autofluorescence is observed in freshly cut tissue sections, permitting straight forward observation of Raman scattering bands. Further, although the autofluorescence signal is not completely absent in freshly cut tissues, its presence appears to offer the capability to localise lipofuscin deposits, which are often used as a marker of cell ageing or oxidative damage. At this stage, the exact identity of the endogenous fluorophore(s) responsible for autofluorescence is(are) not known, and this would be exceedingly difficult, if not impossible, to determine from fluorescence microscopy alone. It is likely that common fluorophores such as NADH, flavins, collagen, elastin, lipofuscin deposits, and aromatic amino acids are all contributing, at least in part to the fluorescence signal. Although only speculation, it is possible that tissue oxidation occurs as a function of time since tissue sectioning, and this increases the fluorescent propensity of the brain tissue (e.g., increasing conjugation through oxidation of hydroxyl moieties to aldehydes or ketones is one possible pathway). There is evidence in the literature to support time-dependent tissue oxidation following tissue sectioning, which may account for the time dependent increase in autofluorescence [117].

5.2.2 Endogenous Tissue Autofluorescence Combined with Raman Microscopy Analysis of Fresh (< 24 hours) Flash Frozen Brain Tissue Sections Provide Subcellular Neuron Biochemical Insight

Following the Raman and fluorescence microscopy experiments, a series of Raman analyses of a specific cell type, Purkinje neurons from rat cerebellum, were carried out. To minimise autofluorescence, flash-frozen, unfixed tissue samples were analysed with confocal Raman microscopy on the day of sectioning, and fluorescence microscopy data was collected within 24 hours of sectioning. Immediately following fluorescence microscopy analysis of the unstained tissues, the tissue sections were immersion fixed for routine histology (H&E) staining. Representative bright field optical microscopy images of a Purkinje neuron in unstained tissue, a confocal Raman microscopy image of the same neuron in unstained tissue, a fluorescence microscopy image of the same neuron in unstained tissue, and the optical microscopy image of the same neuron following fixation and H&E staining are presented in Figure 5.5. Although the general location of the neuron can be seen in the optical image of the unstained tissue (Figure 5.5B), the H&E image from the stained tissue (Figure 5.5A, C) is required for identification of neuron cytoplasm and nucleus. Comparison of the Raman microscopy image (Figure 5.5D), with the H&E stained images (Figures 5.5A, C) enables features such as the cell body, nucleus, and cytoplasm to be identified in the Raman image. The autofluorescence signal in the Raman data (Figure 5.5D) and the fluorescence microscopy images (green emission in Figure 5.5E, red emission in Figure 5.5F) provide visualisation of lipofuscin deposits.

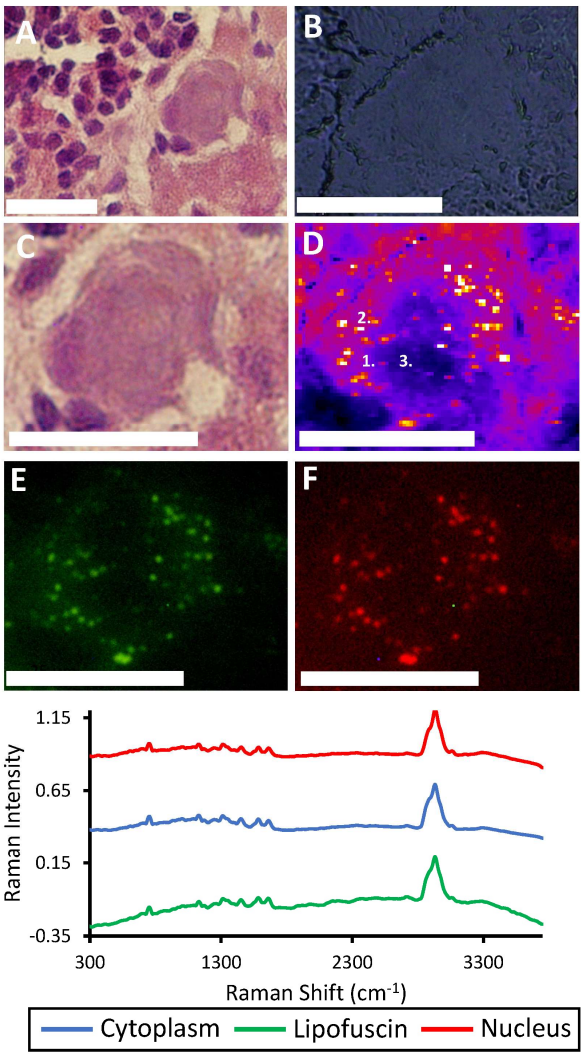

***Figure 5.5**: Multimodal Raman microscopy, fluorescence microscopy, and H&E histology on the same brain cell (cerebellum Purkinje neuron). Overview H&E histology of the analysed neuron and surrounding tissue structures (A), bright field image of the unstained tissue prior to Raman analysis (B), H&E histology of the exact tissue region analysed with Raman microscopy (C), Raman signal across 2800-3030 cm^{-1} without background subtraction, which is largely dominated by autofluorescence (D), and fluorescence microscopy measurements with blue excitation (λ_{ex}=465/15 nm) / (LP λ_{em}=515 nm) (E) and green excitation (λ_{ex}=530/40 nm) / (LP λ_{em}=590 nm) (F). Representative Raman spectra from different subcellular compartments: cytoplasm (1 in panel D), fluorescent lipofuscin deposits (2 in panel D), nucleus (3 in panel D) are also shown. Order of analysis was Raman microscopy of unstained and non-fixed tissue, autofluorescence analysis of unstained and non-fixed tissue, and lastly H&E staining of formalin-fixed tissue. Scale bars represent 25 µm.*

The multi-modal combination of Raman microscopy, fluorescence microscopy, and histology, performed on the same tissue section enabled comparison of Raman spectra extracted from different subcellular regions of Purkinje neurons (nucleus, cytoplasm, and lipofuscin), as shown in Figure 5.5. The ability of Raman spectroscopy to study subcellular biochemistry is already well established in the field [218, 241-248]. Despite the subcellular imaging capability being well established, examples of Raman spectroscopy applied to neurons, *in situ* in brain tissue are scarce (although applications to other brain structures, such as white matter tracts [242-244], and amyloid-β plaques can be found) [249, 250]. This is likely due to past difficulties in overcoming

tissue autofluorescence, which can now be overcome by minimising the time between tissue sectioning and Raman analyses. Not unexpectedly, significant differences were observed in spectra extracted from different subcellular compartments of neurons. Although an exhaustive multi-variate analysis has not been undertaken in this study, the Raman spectra clearly reveal a) low total lipid content in the nucleus as demonstrated by reduced Raman scattering in the methylene C-H stretching region (2830-2900 cm^{-1}) [81, 223, 251] (Figure 5.6C); b) a relative increase in methyl groups (2900 – 3000 cm^{-1}) and N-H stretching vibrations (3035-3090 cm^{-1}) in the nucleus (Figure 5.6C), similar to previous reports [252]; c) elevated signal from the pyrimidine ring breathing region of DNA and RNA bases [218] (750 cm^{-1}) in the nucleus and cytoplasm compared to lipofuscin (Figure 5.6A), and of note, d) a relative increase in scattering across 1633 – 1692 cm^{-1} in spectra extracted from lipofuscin (Figure 5.6B). Raman scattering across 1633 – 1692 cm^{-1} could be attributed to the amide I band of proteins [251, 253] (a relatively weak Raman scatterer), or C=C stretching in unsaturated lipids [251, 253, 254]. Due to the absence of an increase in other typical protein bands in the lipofuscin spectra (e.g., phenylalanine or tyrosine modes), the increased scattering could be attributed to unsaturated lipids or lipid-oxidation products in the lipofuscin aggregates [254].

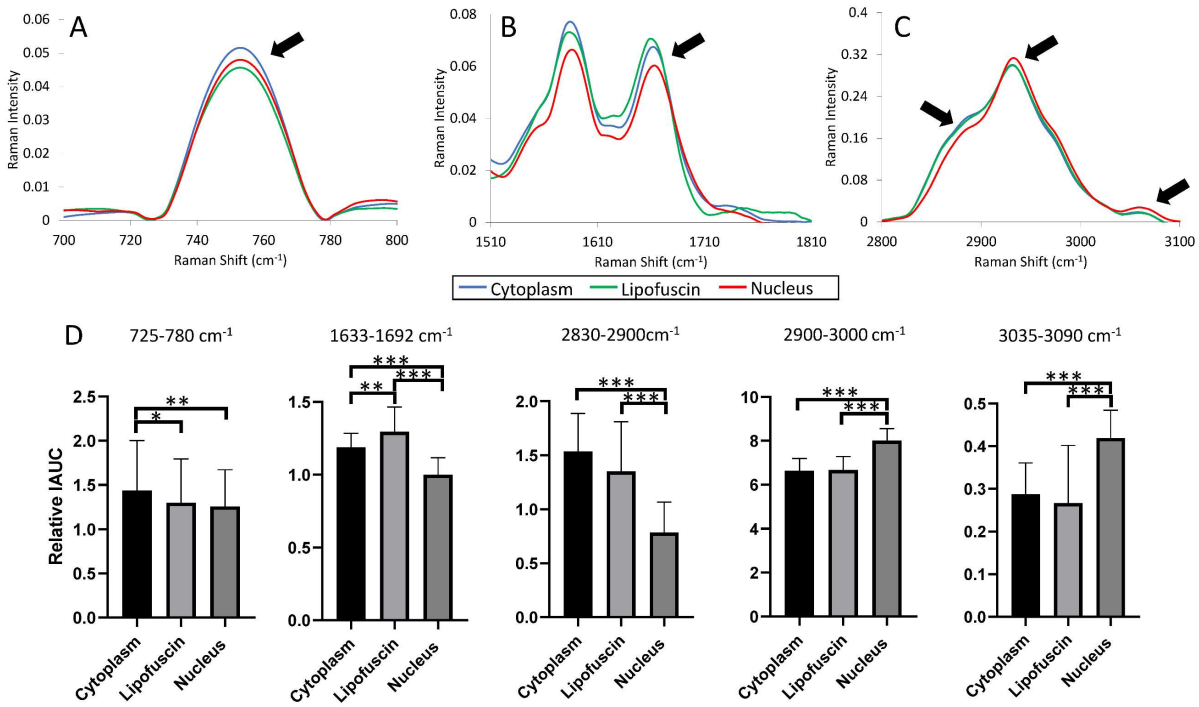

Figure 5.6*: Confocal Raman spectroscopic analysis of chemical differences between different subcellular compartments in Purkinje neurons (cytoplasm, autofluorescent lipofuscin deposits, nucleus). Representative Raman spectra are shown for 3 specific spectral regions: 700 – 800 cm^{-1} (A), 1510 – 1810 cm^{-1} (B), and 2800 – 3100 cm^{-1} (C). Spectra have been vector normalised to the ν(C-H) region (2800 – 3100 cm^{-1}) and baseline corrected. Due to the relatively low signal to noise, a 17 point smoothing function has been applied to the raw spectra. Statistically significant differences between the relative IAUCs for Raman scattering peaks shown in panels A-C, were evaluated using a repeated measures one-way ANOVA with multiple comparison testing (D). Significant differences are indicated with asterisks (*p<0.05, **p< 0.01 >, ***p< 0.001).*

5.2.3 Multi-Modal Raman Microscopy and Immunofluorescence Microscopy Analyses on the Same Tissue Section Associates Subcellular Biochemical Imaging with Cell Type Specificity

H&E histology is a useful method to confirm the location of cell bodies and major organelles (e.g., nucleus) however, to determine more cell- or organelle-specific information requires the use of immunohistochemistry or immunofluorescence microscopy. Therefore, this study investigated the capability of immunofluorescence microscopy to be performed on the same tissue sections analysed with Raman microscopy, and fluorescence microscopy of unstained tissues. Unfortunately, the recommended sample preparation for immunofluorescence, tissue fixation, is now known to produce numerous chemical and elemental artefacts in

subsequent spectroscopic analyses [117, 172, 222, 255, 256]. In order to prevent such chemical artefacts, Raman microscopy and endogenous fluorescence microscopy analyses were performed on unfixed tissue sections. Following spectroscopic and endogenous fluorescence analysis, tissue sections were immersion fixed in formalin and underwent immunofluorescence analysis for the presence of a neuronal protein marker (MAP2) and a glial cell marker (GFAP). As can be seen in Figure 5.7, unfixed, flash frozen tissue sections are compatible with a multi-modal microscopy workflow incorporating Raman microscopy analysis (Figure 5.7A), endogenous autofluorescence microscopy analysis (Figure 5.7B green emission, Figure 5.7C red emission), and immunofluorescence (Figure 5.7D, E).

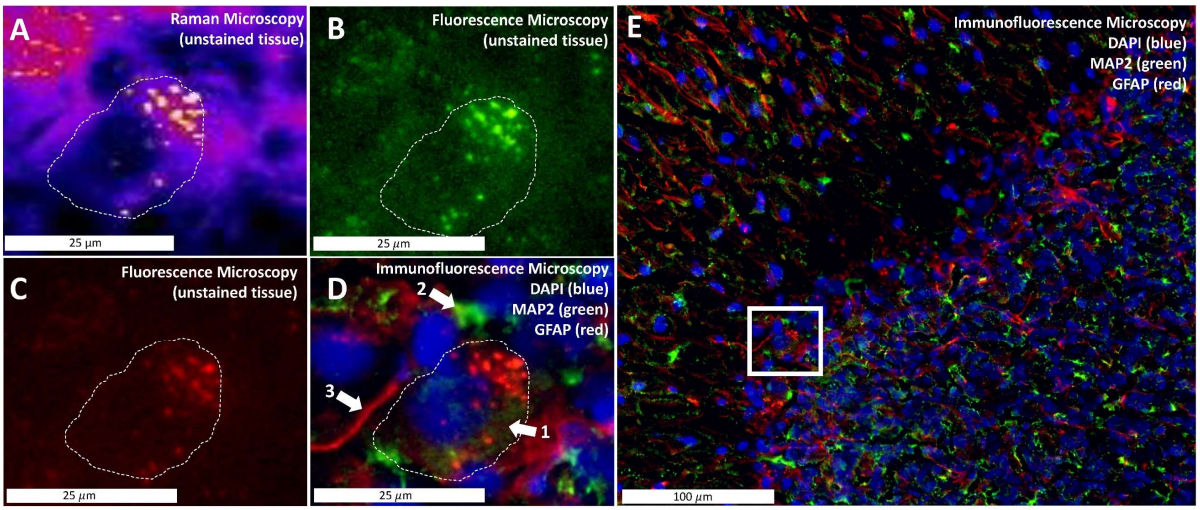

***Figure 5.7**: Multimodal Raman microscopy, endogenous fluorescence microscopy, and immunofluorescence microscopy performed on the same tissue section. Raman microscopy autofluorescence image generated from intensity across 2800-3030 cm^{-1} showing lipofuscin deposits (A) and fluorescence microscopy imaging of lipofuscin deposits recorded with blue excitation (λ_{ex}=465/15 nm) / (LP λ_{em}=515 nm) (B) and green excitation (λ_{ex}=530/40 nm) / (LP λ_{em}=590 nm) (C). The same tissue was stained for immunofluorescence to localise cell nuclei (DAPI, blue), proteins in neuron cytoplasm (MAP2, green), and glial cells (GFAP, red) (D). An expanded view of the immunofluorescence image is also shown (E). Order of analysis was confocal Raman microscopy (unstained, non-fixed tissue), fluorescence microscopy of unstained and unfixed tissue, immunofluorescence microscopy following formalin-fixation of the tissue section.*

This workflow enables specific confirmation that the cell imaged by Raman microscopy is in fact a neuron (presence of positive MAP2 antigenicity within cytoplasm, Figure 5.7D-arrows 1 and 2). The multi-modal Raman and immunofluorescence imaging also allows the proximity

of other cell types to be viewed in relation to the neuron e.g., an astrocyte process running parallel to the neuron (as shown in Figure 5.7D-arrow 3). Due to the growing recognition of the important physical and chemical connections between neurons and glia, the application of a multi-model workflow such as reported here, may enable greater insight into the chemical interactions (revealed by Raman microscopy) between different cell types (revealed by immunofluorescence). Although multi-modal Raman microscopy and immunofluorescence (or immunohistochemistry) has previously been reported multiple times in the literature, such studies used either serial tissue sections [113], or chemically fixed tissues for both spectroscopic and immunofluorescence measures [250]. The protocol reported here offers a significant advantage as it makes possible association of biochemical data collected free of the chemical-fixation artefacts, while still offering the benefits of subsequent immunofluorescence microscopy. Further examples of successful immunofluorescence staining of tissue that was immersion fixed post-sectioning are provided in Figure 5.8.

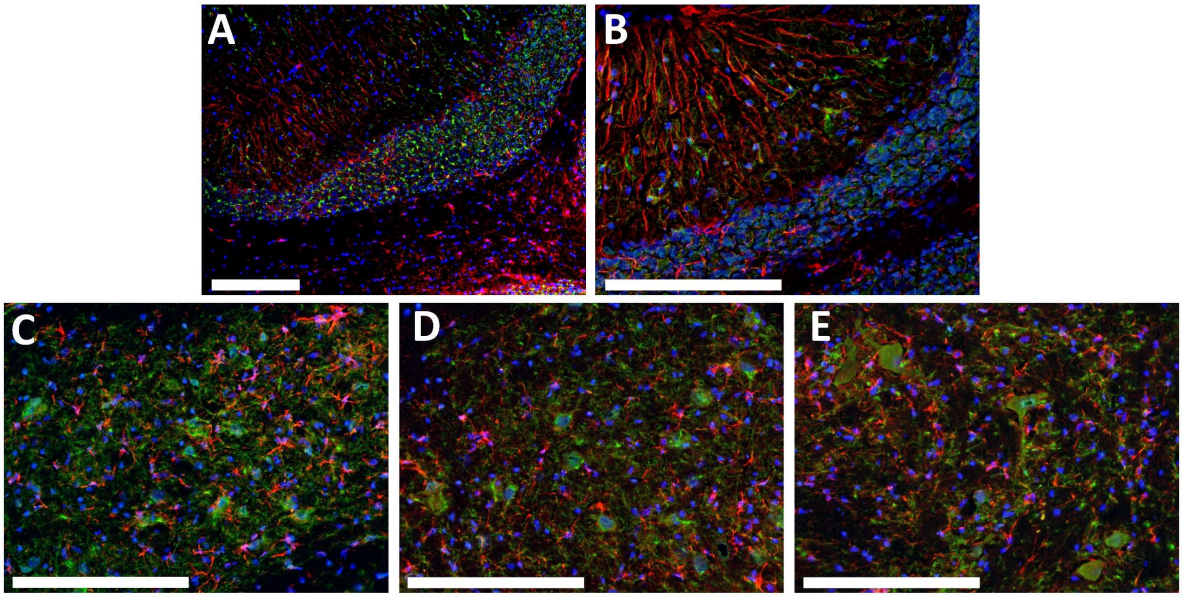

***Figure 5.8**: Immunofluorescence images of the granular layer, molecular layer, white matter (A, B), and dentate nucleus (C, D, E) of the cerebellum in air dried tissue sections. Cell nuclei (DAPI, blue), proteins in neuron cytoplasm (MAP2, green), and glial cells (GFAP, red) are all fluorescently stained. Images were captured with 10x or 20x magnification with 3 different excitation energies and emission filter pairings: UV λ_{ex}=375/28 nm (LP λ_{em}=435 nm), blue λ_{ex}=465/15 nm (LP λ_{em}=515 nm), green λ_{ex}=530/40 nm (LP λ_{em}=590 nm). Scale bars represent 200 μm.*

5.2.4 Flash-Frozen Unfixed Tissue Sections can be Analysed with XFM, and then Immersion-Fixed for Successful Immunofluorescence

To demonstrate the transferability of the tissue preparation principles observed in the work with Raman microscopy, similar techniques were used to develop a multi-modal imaging strategy using XFM followed by immunofluorescence. Rapidly frozen, unfixed tissues were sectioned with a cryo-microtome and maintained at cryogenic temperatures until XFM analysis (storage in $-80°C$ freezer, and transport to synchrotron facility on dry ice). XFM analysis was undertaken at cryogenic temperature, using a liquid nitrogen cryostream, which kept the sample surface at $-40°C$. Following XFM elemental mapping, the tissue sections were air dried, immersion-fixed, and then subjected to routine immunofluorescence analysis. To demonstrate the wide-spread applicability of this protocol, experiments were undertaken on brain tissue performing immunofluorescence detection of GFAP.

GFAP antibodies localised to the astrocytes and a DAPI counterstain was used to identify cell nuclei. Astrocytes are the most abundant cell type in the central nervous system, and there are high levels of Cu containing astrocytes in the SVZ [65, 197] near the hippocampus. This meant using GFAP antibodies was useful for the method development process since there would be strong positive staining expected to correlate with XFM imaged regions. Figure 5.9 shows the XFM elemental maps, and the immunofluorescence stained tissue with indications of where the XFM and XANES maps were collected from. It is evident based on changes to tissue fluorescence in the immunofluorescence image, that the X-rays caused photodamage, indicated by the increased fluorescence for the XFM imaged region, and reduced fluorescence in the XANES imaged region. The reason for this difference in photodamage for the two regions is a result of X-ray exposure time with the XANES imaged region exposed to X-rays for significantly longer than the XFM region (~ 50x longer, e.g., 98 images collected with 0.2 ms dwell for XANES rather than just 1 image collected at 0.4 ms for XFM), resulting in more severe tissue damage, rather than just increased fluorescence. Analysis of the fluorescence intensity from the non-irradiated, XFM imaged, and XANES imaged regions from 4 tissue sections demonstrated that for most samples, there was increased fluorescence for the XFM imaged region, and reduced fluorescence for the XANES imaged region, relative to the non-irradiated region as indicated in the figure. For one sample however, the XANES imaged region was significantly photobleached with very high fluorescence signals relative to the non-irradiated

region. This could be further indication that prolonged exposure to X-rays will cause fluorescence to increase, but continued exposure will result in complete damage as was observed for one sample in which the tissue was burnt through and there was almost no fluorescence signal from the XANES region. The wide range of fluorescence signals from the XANES imaged regions can therefore be attributed to different phases of photodamage. While there were no statistically significant differences between the XANES imaged and the non-irradiated regions due to the variability in data, it was evident, based on visual inspection, that immunofluorescence staining post XANES imaging is not possible at this stage. While there is increased fluorescence in the XFM imaged region relative to the non-irradiated region, it was not statistically significant, and though clearly visible in some images, it did not appear to hinder the efficiency of immunofluorescence staining. This enabled generation of an overlay image (figure 5.9, panel G) showing the co-localisation of Cu and astrocytes, which demonstrated the validity of this multi-modal imaging strategy and its potential application in future studies.

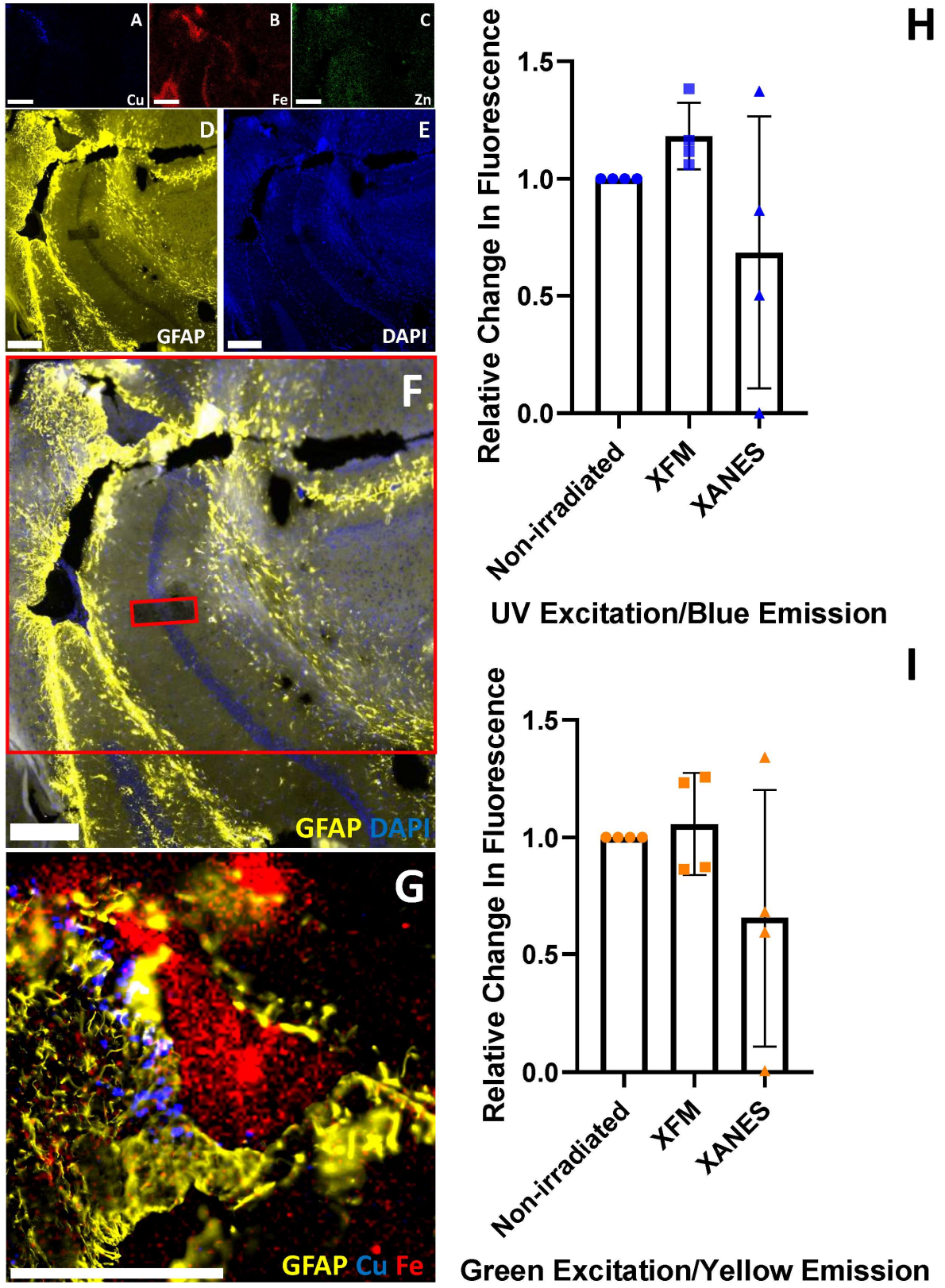

Figure 5.9: *Multimodal XFM and immunofluorescence microscopy of brain tissue. Frozen, 10 µm SAMP8 mouse sections mounted on 1 µm thick silicon nitride windows were used to collect XFM maps of Cu (A), Fe (B) and Zn (C) under a cryostream. Maps were generated simultaneously in one pass at 9803 eV, 4 µm step size and 0.4 ms dwell time. XANES data was*

then collected from a sub-region in 98 passes using energies between 9630 and 9803 eV, with a 2 µm step size and a 0.2 ms dwell time. The same tissue section was subsequently air dried, fixed and stained with GFAP (yellow, D) antibodies to identify astrocytes, and DAPI (blue, E) was used as a counterstain to indicate cell nuclei. An overlay of the GFAP and DAPI stains is shown in panel F along with indications of the XFM (large rectangle) and XANES (small rectangle) imaged regions. Fluorescence increased with exposure to X-rays at each wavelength observed, however, prolonged exposure to X-rays during XANES image collection caused tissue damage and reduced fluorescence in most cases (H, I). The wide spread of fluorescence values across samples resulted in no statistically significant differences between irradiated regions, however, visual inspection demonstrates that immunofluorescence following XANES imaging is not practical due to the extent of beam damage, but, immunofluorescence following XFM imaging is achievable. An Fe (red), Cu (blue), and GFAP (yellow) overlay image of the ventricle has been included as a proof of concept (G). One representative image is shown in panels A-G. n=4. All scale bars represent 250 µm.

5.3 CONCLUSION

This chapter has outlined a multi-modal protocol that minimises sample preparation-induced autofluorescence while preserving (at least in part) endogenous tissue autofluorescence. This enables subsequent direct label-free subcellular biochemical Raman imaging, measurement of endogenous tissue autofluorescence, and the ability to stain the exact same tissue sections with routine histological stains, or immunofluorescence. The major advantage of this protocol over previous reports in the field, is that it demonstrates the collection of spectroscopy data on flash frozen un-fixed tissues, prior to subsequent immersion fixation for immunohistochemical analysis. There are numerous examples in the literature highlighting the benefit of multi-modal spectroscopic and immunofluorescence imaging, however the conventional approach is to use chemically fixed samples for both spectroscopic and immunofluorescence measures, thereby most likely introducing chemical artefacts into the spectroscopic data – such issues can now be avoided using the protocol highlighted in this study. Furthermore, this principle is transferrable, and evidently, unfixed tissue can also be exposed to X-ray fluorescence microscopy followed by fixation and immunofluorescence, thereby multiplying the value of information extracted from each sample. This multi-modal approach can hopefully be applied in future studies of brain disease and neurodegeneration to assist in understanding the various cellular mechanisms that may be involved.

Chapter 6: Conclusions and Suggestions for Further Work

This thesis has described the development and application of multiple spectroscopic techniques to study metals and altered brain biochemistry during ageing. The development of a Zn XANES spectral library not only enabled identification of the most abundant chemical forms of Zn in the hippocampus and cerebellum, but also highlighted the effect that factors such as common counter ions (e.g., Cl^-) and changes in pH have on Zn speciation in solution. Additionally, it highlighted some of the limitations associated with certain sample preparation protocols and confirmed that glycerol, a common glassing agent, alters the Zn coordination environment so careful consideration should be made when using glassing agents and interpreting results.

The development of a Zn XANES imaging protocol has further emphasised the importance of careful sample preparation considerations, revealing that the tissue sectioning and air drying processes disturb the *in vivo* Zn coordination environment. Although the *in vivo* Zn environment was not accurately reflected by the results presented in this thesis, the data provides a proof of concept for the protocol which should be applied in future studies of flash frozen tissue. Additionally, the method that was developed for Zn should be transferable to other transition metals such as Fe and Cu, so the development of spectral libraries and XANES imaging of frozen biological tissues to investigate Fe and Cu speciation during ageing and disease should be considered.

The application of spectroscopic techniques to study the potential consequences of altered metal homeostasis during ageing was also demonstrated. Specifically, a combination of XANES and FTIR imaging revealed that the age-related accumulation of Cu in the SVZ does not likely cause an elevation in markers of oxidative stress, suggesting that either the Cu is not a chemical form that readily drives oxidative stress, or that there are sufficient antioxidant defences in place to buffer Cu mediated production of ROS. In addition to expanding knowledge of the biochemical processes that may be occurring during ageing, this investigation has revealed the need for further studies to identify the exact subcellular location, and specific chemical forms of Cu in this region. Additional mechanistic studies to identify whether the Cu accumulation is natural, protective, or has pathological consequences are also recommended.

Finally, the development of a protocol that can couple spectroscopic imaging with immunohistochemistry on the same tissue sections is promising for future studies not only relating to brain ageing, but hopefully to many studies involving biological tissue sections. The ability to correlate biochemical changes with particular cell types or subcellular regions could be invaluable to expanding knowledge of the various cellular mechanisms that may be involved in health and disease.

In summary, this thesis has emphasised the importance of careful sample preparation considerations when using direct spectroscopic imaging techniques, and suggested protocols for XANES imaging of brain tissue, in addition to correlative spectroscopic imaging and immunohistochemistry. Furthermore, it has demonstrated the application of spectroscopic techniques to investigate the potential consequences of altered metal homeostasis during ageing. The insights provided in this thesis will hopefully assist in future studies relating to altered metal homeostasis and brain biochemistry during ageing, potentially enabling the mechanisms contributing to cognitive decline to be further understood. Greater understanding of the pathways or mechanisms contributing to memory loss and the onset of neurodegenerative disease are vital for the identification of targets for therapeutic or preventative intervention.

APPENDIX

Table 1: *p-values from repeated measures one-way ANOVAs comparing the fluorescence intensity over time in three cerebellar sub-regions. Measurements were taken using fluorescence microscopy with blue excitation.*

Fluorescence Microscopy (blue excitation) **Granular Layer**					
	Day 1	Day 2	Day 3	Day 5	Day 9
Day 1		0.0570	0.0022	0.0026	0.0007
Day 2			0.0072	0.0079	0.0012
Day 3				0.3024	0.0057
Day 5					0.0011
Day 9					
Molecular Layer					
Day 1		0.0449	0.0063	0.0002	0.0004
Day 2			0.0037	0.0010	0.0020
Day 3				0.3831	0.0383
Day 5					0.0079
Day 9					
White Matter					
Day 1		0.0584	0.0092	0.0019	0.0002
Day 2			0.0092	0.0012	0.0005
Day 3				0.0853	0.0055
Day 5					0.0029
Day 9					

Table 2: *p-values from repeated measures one-way ANOVAs comparing the fluorescence intensity over time in three cerebellar sub-regions. Measurements were taken using fluorescence microscopy with green excitation*.

Fluorescence Microscopy (green excitation) **Granular Layer**					
	Day 1	Day 2	Day 3	Day 5	Day 9
Day 1		0.0047	<0.0001	<0.0001	<0.0001
Day 2			0.0342	0.0058	0.0023
Day 3				>0.9999	0.0019
Day 5					0.0086
Day 9					
Molecular Layer					
Day 1		0.0127	0.0001	<0.0001	<0.0001
Day 2			0.0297	0.0127	0.0097
Day 3				0.8455	0.0817
Day 5					0.0055
Day 9					
White Matter					
Day 1		0.0254	0.0014	<0.0001	<0.0001
Day 2			0.0581	0.0050	0.0022
Day 3				0.2427	0.0112
Day 5					0.0014
Day 9					

Table 3: *p-values from repeated measures one-way ANOVAs comparing the fluorescence intensity over time in three cerebellar sub-regions. Measurements were taken using fluorescence microscopy with UV excitation.*

Fluorescence Microscopy (UV excitation) **Granular Layer**					
	Day 1	Day 2	Day 3	Day 5	Day 9
Day 1		0.0013	0.0002	0.0003	<0.0001
Day 2			>0.9999	>0.9999	0.0010
Day 3				0.3608	<0.0001
Day 5					0.0004
Day 9					
Molecular Layer					
Day 1		0.0213	0.0086	0.0037	0.0001
Day 2			0.7480	0.1235	0.0003
Day 3				0.0094	<0.0001
Day 5					0.0008
Day 9					
White Matter					
Day 1		0.0083	0.0016	0.0012	0.0001
Day 2			>0.9999	>0.9999	0.0028
Day 3				0.0453	<0.0001
Day 5					0.0002
Day 9					

Table 4: *p-values from repeated measures one-way ANOVAs comparing the fluorescence signal over time in three cerebellar sub-regions. Measurements were taken using a dispersive Raman microscope with green excitation.*

Dispersive Raman Microscopy **Granular Layer**					
	Day 1	Day 2	Day 3	Day 5	Day 9
Day 1		0.0158	0.0174	0.0028	0.0004
Day 2			0.3504	0.0132	0.0017
Day 3				0.0124	0.0024
Day 5					0.0037
Day 9					
Molecular Layer					
Day 1		0.0051	0.0002	0.0001	<0.0001
Day 2			0.0601	0.0001	<0.0001
Day 3				0.0036	0.0003
Day 5					0.0044
Day 9					
White Matter					
Day 1		>0.9999	0.6781	0.0156	0.0073
Day 2			0.5961	0.0209	0.0034
Day 3				0.0355	0.0043
Day 5					>0.9999
Day 9					

Table 5: *p-values from repeated measures one-way ANOVAs comparing the fluorescence signal over time in three cerebellar sub-regions. Measurements were taken using a confocal Raman microscope with green excitation.*

***Confocal Raman Microscopy* Granular Layer**					
	Day 1	Day 2	Day 3	Day 5	Day 9
Day 1		0.2683	0.0508	0.0394	0.0008
Day 2			>0.9999	0.0591	0.0136
Day 3				0.9813	0.0532
Day 5					>0.9999
Day 9					
Molecular Layer					
Day 1		0.3779	0.0416	0.0003	0.0011
Day 2			0.2944	0.0090	0.0012
Day 3				0.0646	0.0211
Day 5					0.0812
Day 9					
White Matter					
Day 1		0.0018	0.0052	<0.0001	<0.0001
Day 2			0.4782	<0.0001	0.0001
Day 3				0.0007	0.0022
Day 5					>0.9999
Day 9					

REFERENCES

1. World_Health_Organization. Dementia 2021 [cited 2022. Available from: https://www.who.int/news-room/fact-sheets/detail/dementia#:~:text=Rates%20of%20dementia,and%20139%20million%20in%202050.

2. Lu LC. Alzheimer's disease / Linda C. Lu and Juergen H. Bludau. Bludau J, editor. Santa Barbara, Calif.: Santa Barbara, Calif. : Greenwood; 2011.

3. International AsD. World Alzheimer Report 2016 United Kingdom2016 [cited 2018 May 19]. Available from: https://www.alz.co.uk/research/worldalzheimerreport2016sheet.pdf

4. Orrenius S, Packer L, Cadenas E. Mitochondrial Signaling in Health and Disease. 1 ed2012.

5. Moreira PI, Carvalho C, Zhu X, Smith MA, Perry G. Mitochondrial dysfunction is a trigger of Alzheimer's disease pathophysiology. Biochimica et Biophysica Acta (BBA) - Molecular Basis of Disease. 2010;1802(1):2-10. 10.1016/j.bbadis.2009.10.006.

6. Hou Y, Dan X, Babbar M, Wei Y, Hasselbalch SG, Croteau DL, et al. Ageing as a risk factor for neurodegenerative disease. Nat Rev Neurol. 2019;15(10):565-81. 10.1038/s41582-019-0244-7.

7. Poddar J, Pradhan M, Ganguly G, Chakrabarti S. Biochemical deficits and cognitive decline in brain aging: Intervention by dietary supplements. J Chem Neuroanat. 2019;95:70-80. 10.1016/j.jchemneu.2018.04.002.

8. Yin F, Sancheti H, Patil I, Cadenas E. Energy metabolism and inflammation in brain aging and Alzheimer's disease. Free Radic Biol Med. 2016;100:108-22. 10.1016/j.freeradbiomed.2016.04.200.

9. Scheiber IF, Mercer JFB, Dringen R. Metabolism and functions of copper in brain. Progress in Neurobiology. 2014;116:33-57. 10.1016/j.pneurobio.2014.01.002.

10. Nakashima AS, Dyck RH. Zinc and cortical plasticity. Brain Research Reviews. 2009;59(2):347-73. 10.1016/j.brainresrev.2008.10.003.

11. Portbury SD, Adlard PA. Zinc Signal in Brain Diseases. Int J Mol Sci. 2017;18(12). 10.3390/ijms18122506.

12. Luigi Z, Moussa BHY, Peter R, James RC, Robert RC. Iron, brain ageing and neurodegenerative disorders. Nature Reviews Neuroscience. 2004;5(11):863. 10.1038/nrn1537.

13. Hancock SM, Finkelstein DI, Adlard PA. Glia and zinc in ageing and Alzheimer's disease: a mechanism for cognitive decline? Front Aging Neurosci. 2014;6. 10.3389/fnagi.2014.00137.

14. Rathnasamy G, Ling E-A, Kaur C. Consequences of Iron Accumulation in Microglia and its Implications in Neuropathological Conditions. CNS & Neurological Disorders-Drug Targets. 2013;12(6):785-98.

15. Scheiber IF, Dringen R. Astrocyte functions in the copper homeostasis of the brain. Neurochemistry International. 2013;62(5):556-65. 10.1016/j.neuint.2012.08.017.

16. James S, Volitakis I, Adlard P, Duce J, Masters C, Cherny R, et al. Elevated labile Cu is associated with oxidative pathology in Alzheimer disease. Free Radical Biology and Medicine. 2012;52(2):298-302. 10.1016/j.freeradbiomed.2011.10.446.

17. Zecca L, Zucca FA, Toscani M, Adorni F, Giaveri G, Rizzio E, et al. Iron, copper and their proteins in substantia nigra of human brain during aging. Journal of Radioanalytical and Nuclear Chemistry. 2005;263(3):733-7. 10.1007/s10967-005-0650-8.

18. Ramos P, Santos A, Pinto NR, Mendes R, Magalhães T, Almeida A. Anatomical Region Differences and Age-Related Changes in Copper, Zinc, and Manganese Levels in the Human Brain. Biological Trace Element Research. 2014;161(2):190-201. 10.1007/s12011-014-0093-6.

19. Xu J, Church SJ, Patassini S, Begley P, Waldvogel HJ, Curtis MA, et al. Evidence for widespread, severe brain copper deficiency in Alzheimer's dementia. Metallomics. 2017;9(8):1106-19. 10.1039/C7MT00074J.

20. Fimognari N, Hollings A, Lam V, Tidy R, Kewish CM, Albrecht MA, et al. Biospectroscopic Imaging Provides Evidence of Hippocampal Zn Deficiency and Decreased Lipid Unsaturation in an Accelerated Aging Mouse Model. ACS Chem Neurosci. 2018;9(11):2774-85. 10.1021/acschemneuro.8b00193.

21. Watson C. The brain : an introduction to functional neuroanatomy / Charles Watson, Matthew Kirkcaldie, George Paxinos. Kirkcaldie M, Paxinos G, editors. Amsterdam: Amsterdam : Elsevier; 2010.

22. Frederickson RE, Frederickson CJ, Danscher G. In situ binding of bouton zinc reversibly disrupts performance on a spatial memory task. Behavioural Brain Research. 1990;38(1):25-33. 10.1016/0166-4328(90)90021-6.

23. Smith DG, Cappai R, Barnham KJ. The redox chemistry of the Alzheimer's disease amyloid β peptide. Biochimica et biophysica acta Biomembranes. 2007;1768(8):1976-90. 10.1016/j.bbamem.2007.02.002.

24. Butterfield DA, Kanski J. Brain protein oxidation in age-related neurodegenerative disorders that are associated with aggregated proteins. Mechanisms of Ageing and Development. 2001;122(9):945-62. 10.1016/S0047-6374(01)00249-4.

25. Gelpi RJe, Boveris Ae, Poderoso JJe. Biochemistry of Oxidative Stress : Physiopathology and Clinical Aspects / edited by Ricardo Jorge Gelpi, Alberto Boveris, Juan José Poderoso. 1st ed. 2016.. ed: Cham : Springer International Publishing : Imprint: Springer; 2016.

26. Stadtman ER, Berlett BS. Reactive Oxygen-Mediated Protein Oxidation in Aging and Disease. Chem Res Toxicol. 1997;10(5):485-94. 10.1021/tx960133r.

27. Girotti AW. Mechanisms of lipid peroxidation. Journal of Free Radicals in Biology & Medicine. 1985;1(2):87-95. 10.1016/0748-5514(85)90011-X.

28. Pizzino G, Irrera N, Cucinotta M, Pallio G, Mannino F, Arcoraci V, et al. Oxidative Stress: Harms and Benefits for Human Health. Oxid Med Cell Longev. 2017;2017:1-13. 10.1155/2017/8416763.

29. Lee SR. Critical Role of Zinc as Either an Antioxidant or a Prooxidant in Cellular Systems. Oxid Med Cell Longev. 2018;2018:9156285-11. 10.1155/2018/9156285.

30. Eide DJ. The oxidative stress of zinc deficiency. Metallomics. 2011;3(11):1124-9. 10.1039/c1mt00064k.

31. Marreiro DdN, Cruz KJC, Morais JBS, Beserra JB, Severo JS, Soares de Oliveira AR. Zinc and oxidative stress: Current mechanisms. Antioxidants (Basel). 2017;6(2):24. 10.3390/antiox6020024.

32. Oteiza PI. Zinc and the modulation of redox homeostasis. Free radical biology & medicine. 2012;53(9):1748-59. 10.1016/j.freeradbiomed.2012.08.568.

33. Zago MP, Oteiza PI. The antioxidant properties of zinc: interactions with iron and antioxidants. Free Radical Biology and Medicine. 2001;31(2):266-74. https://doi.org/10.1016/S0891-5849(01)00583-4.

34. Frazzini V, Rockabrand E, Mocchegiani E, Sensi SL. Oxidative stress and brain aging: is zinc the link? Biogerontology. 2006;7(5):307-14. 10.1007/s10522-006-9045-7.

35. Soto C, Estrada LD. Protein Misfolding and Neurodegeneration. Archives of Neurology. 2008;65(2):184-9. 10.1001/archneurol.2007.56.

36. Yusuf Tutar AÖr, Lütfi Tutar. Role of Protein Aggregation in Neurodegenerative Diseases London: IntechOpen; 2013 [updated 2013; cited 2022 08/04]. Available from: https://www.intechopen.com/chapters/44540.

37. Kim AC, Lim S, Kim YK. Metal Ion Effects on Aβ and Tau Aggregation. Int J Mol Sci. 2018;19(1):128. 10.3390/ijms19010128.

38. Tidy R, Lam V, Fimognari N, Mamo J, Hackett M. FTIR studies of the similarities between pathology induced protein aggregation in vivo and chemically induced protein aggregation ex vivo. 2016.

39. McCall KA, Huang C, Fierke CA. Function and mechanism of zinc metalloenzymes. The Journal of nutrition. 2000;130:1437S-46S. 10.1093/jn/130.5.1437S.

40. Takeda A. Zinc homeostasis and functions of zinc in the brain. J Neurochem. 2003;87:53-.

41. Crichton RR. Biological inorganic chemistry : a new introduction to molecular structure and function London : Academic Press; 2019.

42. Mocchegiani E, Bertoni-Freddari C, Marcellini F, Malavolta M. Brain, aging and neurodegeneration: role of zinc ion availability. Progress in neurobiology. 2005;75(6):367-90. 10.1016/j.pneurobio.2005.04.005.

43. Frederickson CJ, Klitenick MA, Manton WI, Kirkpatrick JB. Cytoarchitectonic distribution of zinc in the hippocampus of man and the rat. Brain Res. 1983;273(2):335-9. 10.1016/0006-8993(83)90858-2.

44. Qiu M, Shentu Y-P, Zeng J, Wang X-C, Yan X, Zhou X-W, et al. Zinc mediates the neuronal activity-dependent anti-apoptotic effect. PloS one. 2017;12(8):e0182150-e. 10.1371/journal.pone.0182150.

45. Frederickson C, Suh S, Silva D, Thompson R. Importance of Zinc in the Central Nervous System: The Zinc-Containing Neuron. Journal of Nutrition. 2000;130(5):1471S-83S. 10.1093/jn/130.5.1471S.

46. Takeda A. Movement of zinc and its functional significance in the brain. 2000. p. 137-48.

47. Laity JH, Lee BM, Wright PE. Zinc finger proteins: new insights into structural and functional diversity. Current Opinion in Structural Biology. 2001;11(1):39-46. 10.1016/S0959-440X(00)00167-6.

48. Baran C, Smith GST, Bamm VV, Harauz G, Lee JS. Divalent cations induce a compaction of intrinsically disordered myelin basic protein. Biochemical and Biophysical Research Communications. 2010;391(1):224-9. 10.1016/j.bbrc.2009.11.036.

49. Nuzzo S, Meneghini C, Mobilioo S, Haas H, Riccio P, Fasano A, et al. An X-Ray Absorption Spectroscopy Study of the Zinc Environment in Langmuir-Blodgett Phospholipid Multilayers. Biophysical Journal. 2002;83(6):3507-12. 10.1016/S0006-3495(02)75350-2.

50. Lindskog S. Structure and mechanism of carbonic anhydrase. Pharmacol Ther. 1997;74(1):1-20. 10.1016/S0163-7258(96)00198-2.

51. Weller MTa. Inorganic chemistry. Sixth edition / Mark Weller, Tina Overton, Jonathan Rourke, Fraser Armstrong.. ed. Overton Ta, Rourke Ja, Armstrong FAa, editors: Oxford Oxford University Press ©2014; 2014.

52. Song H, Wilson DL, Farquhar ER, Lewis EA, Emerson JP. Revisiting Zinc Coordination in Human Carbonic Anhydrase II. Inorg Chem. 2012;51(20):11098-105. 10.1021/ic301645j.

53. Frederickson C, Bush A. Synaptically released zinc: Physiological functions and pathological effects. Biometals. 2001;14(3-4):353-66. 10.1023/A:1012934207456.

54. Mott DD, Dingledine R. Unraveling the role of zinc in memory. Proceedings of the National Academy of Sciences of the United States of America. 2011;108(8):3103-4. 10.1073/pnas.1100323108.

55. Sato S, Frazier J, Goldberg A. The distribution and binding of zinc in the hippocampus. Journal of Neuroscience. 1984;4(6):1662-70.

56. Kay AR. Imaging synaptic zinc: promises and perils. Trends in Neurosciences. 2006;29(4):200-6. 10.1016/j.tins.2006.02.004.

57. Crawford IL, Connor JD. Localization and release of glutamic acid in relation to the hippocampal mossy fibre pathway. Nature. 1973;244(5416):442-3.

58. Blindauer CA, Harvey I, Bunyan KE, Stewart AJ, Sleep D, Harrison DJ, et al. Structure, properties, and engineering of the major zinc binding site on human albumin. The Journal of biological chemistry. 2009;284(34):23116-24. 10.1074/jbc.M109.003459.

59. Barnett JP, Blindauer CA, Kassaar O, Khazaipoul S, Martin EM, Sadler PJ, et al. Allosteric modulation of zinc speciation by fatty acids. Biochimica et Biophysica Acta - General Subjects. 2013;1830(12). 10.1016/j.bbagen.2013.05.028.

60. Smith QR, Rabin O, Chikhale EG. Delivery of Metals to Brain and the Role of the Blood Brain Barrier. Metals and Oxidative Damage in Neurological Disorders. Boston, MA: Springer; 1997. p. 113-30.

61. Malva JO. Interaction Between Neurons and Glia in Aging and Disease / edited by João O. Malva, Ana Cristina Rego, Rodrigo A. Cunha, Catarina R. Oliveira. Rego AC, Cunha RA, Oliveira CR, SpringerLink, editors. Boston, MA: Boston, MA : Springer US; 2007.

62. Auld DS. Zinc-Binding Sites in Proteins. In: Kretsinger RH, Uversky VN, Permyakov EA, editors. Encyclopedia of Metalloproteins. New York, NY: Springer New York; 2013. p. 2554-9.

63. Holm RH, Kennepohl P, Solomon EI. Structural and Functional Aspects of Metal Sites in Biology. Chem Rev. 1996;96(7):2239-314. 10.1021/cr9500390.

64. Pal A, Prasad R. Regional Distribution of Copper, Zinc and Iron in Brain of Wistar Rat Model for Non-Wilsonian Brain Copper Toxicosis. Indian J Clin Biochem. 2015;31(1):93-8. 10.1007/s12291-015-0503-3.

65. Pushkar Y, Robison G, Sullivan B, Fu SX, Kohne M, Jiang W, et al. Aging results in copper accumulations in glial fibrillary acidic protein-positive cells in the subventricular zone. Aging Cell. 2013:<xocs:firstpage xmlns:xocs=""/>. 10.1111/acel.12112.

66. Rihel J. Copper on the brain. Nat Chem Biol. 2018;14(7):638-9. 10.1038/s41589-018-0089-1.

67. Gromadzka G, Tarnacka B, Flaga A, Adamczyk A. Copper dyshomeostasis in neurodegenerative diseases—therapeutic implications. Int J Mol Sci. 2020;21(23):1-35. 10.3390/ijms21239259.

68. Rubino JT, Franz KJ. Coordination chemistry of copper proteins: How nature handles a toxic cargo for essential function. J Inorg Biochem. 2012;107(1):129-43. 10.1016/j.jinorgbio.2011.11.024.

69. Inesi G. Molecular features of copper binding proteins involved in copper homeostasis. IUBMB Life. 2017;69(4):211-7. 10.1002/iub.1590.

70. Zheng W, Monnot AD. Regulation of brain iron and copper homeostasis by brain barrier systems: implication in neurodegenerative diseases. Pharmacol Ther. 2012;133(2):177-88. 10.1016/j.pharmthera.2011.10.006.

71. Robinson NJ, Winge DR. Copper metallochaperones. Annu Rev Biochem. 2010;79(1):537-62. 10.1146/annurev-biochem-030409-143539.

72. Bertini I, Palumaa P, Banci L, Ciofi-Baffoni S, Kozyreva T, Zovo K. Affinity gradients drive copper to cellular destinations. Nature. 2010;465(7298):645-8. 10.1038/nature09018.

73. Hu KH, Friede RL. TOPOGRAPHIC DETERMINATION OF ZINC IN HUMAN BRAIN BY ATOMIC ABSORPTION SPECTROPHOTOMETRY. J Neurochem. 1968;15(7):677-85. 10.1111/j.1471-4159.1968.tb08967.x.

74. Bjorklund NL, Sadagoparamanujam VM, Taglialatela G. Selective, quantitative measurement of releasable synaptic zinc in human autopsy hippocampal brain tissue from Alzheimer's disease patients. J Neurosci Methods. 2012;203(1):146-51. 10.1016/j.jneumeth.2011.09.008.

75. Feng L, Wang J, Li H, Luo X, Li J. A novel absolute quantitative imaging strategy of iron, copper and zinc in brain tissues by Isotope Dilution Laser Ablation ICP-MS. Anal Chim Acta. 2017;984:66-75. 10.1016/j.aca.2017.07.003.

76. Becker JS, Zoriy MV, Pickhardt C, Palomero-Gallagher N, Zilles K. Imaging of Copper, Zinc, and Other Elements in Thin Section of Human Brain Samples (Hippocampus) by Laser Ablation Inductively Coupled Plasma Mass Spectrometry. Anal Chem. 2005;77(10):3208-16. 10.1021/ac040184q.

77. Paul B, Hare DJ, Bishop DP, Paton C, Nguyen VT, Cole N, et al. Visualising mouse neuroanatomy and function by metal distribution using laser ablation-inductively coupled plasma-mass spectrometry imaging. Chem Sci. 2015;6(10):5383-93. 10.1039/C5SC02231B.

78. Urgast DS, Hill S, Kwun I-S, Beattie JH, Goenaga-Infante H, Feldmann J. Zinc isotope ratio imaging of rat brain thin sections from stable isotope tracer studies by LA-MC-ICP-MS. Metallomics. 2012;4(10):1057-63. 10.1039/C2MT20119D.

79. Dowlatshahi Pour M, Ren L, Jennische E, Lange S, Ewing AG, Malmberg P. Mass spectrometry imaging as a novel approach to measure hippocampal zinc. Journal of analytical atomic spectrometry. 2019;34(8):1581-7. 10.1039/c9ja00199a.

80. Linkous DH, Flinn JM, Koh JY, Lanzirotti A, Bertsch PM, Jones BF, et al. Evidence That the ZNT3 Protein Controls the Total Amount of Elemental Zinc in Synaptic Vesicles. J Histochem Cytochem. 2008;56(1):3-6. 10.1369/jhc.6A7035.2007.

81. Summers KL, Fimognari N, Hollings A, Kiernan M, Lam V, Tidy RJ, et al. A Multimodal Spectroscopic Imaging Method To Characterize the Metal and Macromolecular Content of Proteinaceous Aggregates ("Amyloid Plaques"). Biochemistry. 2017;56(32):4107. 10.1021/acs.biochem.7b00262.

82. Ciccotosto GD, James SA, Altissimo M, Paterson D, Vogt S, Lai B, et al. Quantitation and localization of intracellular redox active metals by X-ray fluorescence microscopy in cortical neurons derived from APP and APLP2 knockout tissue. Metallomics. 2014;6(10):1894-904. 10.1039/C4MT00176A.

83. Frederickson CJ, Kasarskis E, Ringo D, Frederickson R. A quinoline fluorescence method for visualizing and assaying the histochemically reactive zinc (bouton zinc) in the brain. Journal of neuroscience methods. 1987;20(2):91-103.

84. Hyman LM, Franz KJ. Probing oxidative stress: Small molecule fluorescent sensors of metal ions, reactive oxygen species, and thiols. Coordination chemistry reviews. 2012;256(19):2333-56.

85. Nydegger I, Rumschik SM, Zhao J, Kay AR. Evidence for an extracellular zinc-veneer in rodent brains from experiments with Zn-ionophores and ZnT3 knockouts. ACS chemical neuroscience. 2012;3(10):761-6.

86. Thompson R, Peterson D, Mahoney W, Cramer M, Maliwal BP, Suh SW, et al. Fluorescent zinc indicators for neurobiology. Journal of neuroscience methods. 2002;118(1):63-75.

87. Nowakowski AB, Petering DH. Reactions of the fluorescent sensor, zinquin, with the zinc-proteome: Adduct formation and ligand substitution. Inorganic chemistry. 2011;50(20):10124-33.

88. Danscher G. Histochemical demonstration of heavy metals: A revised version of the sulphide silver method suitable for both light and electronmicroscopy. Histochemistry. 1981;71(1):1-16. 10.1007/BF00592566.

89. Frederickson CJ, Rampy BA, Reamy-Rampy S, Howell GA. Distribution of histochemically reactive zinc in the forebrain of the rat. J Chem Neuroanat. 1992;5(6):521-30. 10.1016/0891-0618(92)90007-D.

90. Danscher G, Zimmer J. An improved timm sulphide silver method for light and electron microscopic localization of heavy metals in biological tissues. Histochemistry. 1978;55(1):27-40. 10.1007/BF00496691.

91. DeGrado TR, Kemp BJ, Pandey MK, Jiang H, Gunderson TM, Linscheid LR, et al. First PET Imaging Studies With 63Zn-Zinc Citrate in Healthy Human Participants and Patients With Alzheimer Disease. Mol Imaging. 2016;15:1-10. 10.1177/1536012116673793.

92. Bartnicka JJ, Blower PJ. Insights into trace metal metabolism in health and disease from PET: "pET metallomics". J Nucl Med. 2018;59(9):1355-9. 10.2967/jnumed.118.212803.

93. Skoog DA. Principles of instrumental analysis / Douglas A. Skoog, F. James Holler, Stanley R. Crouch. 6th ed.. ed. Holler FJ, Crouch SR, editors. Belmont, CA: Belmont, CA : Thomson, Brooks/Cole; 2007.

94. Skoog DAa. Fundamentals of analytical chemistry / Douglas A. Skoog, Donald M. West, F. James Holler. 9th edition.. ed. West DMa, Holler FJa, editors: Belmont, California : Brooks/Cole; 2013.

95. Higson SA. Analytical chemistry. Higson SA, editor: [Place of publication not identified] Oxford University Press; 2003.

96. Calvin S. XAFS for Everyone: CRC Press; 2013.

97. Pushie MJ, Pickering IJ, Korbas M, Hackett MJ, George GN. Elemental and Chemically Specific X-ray Fluorescence Imaging of Biological Systems. Chem Rev. 2014;114(17):8499-541. 10.1021/cr4007297.

98. Penner-Hahn JE. X-ray absorption spectroscopy in coordination chemistry. Coordination chemistry reviews. 1999;190:1101-23. 10.1016/S0010-8545(99)00160-5.

99. Baker ML, Mara MW, Yan JJ, Hodgson KO, Hedman B, Solomon EI. K- and L-edge X-ray absorption spectroscopy (XAS) and resonant inelastic X-ray scattering (RIXS) determination of differential orbital covalency (DOC) of transition metal sites. Coord Chem Rev. 2017;345(C):182-208. 10.1016/j.ccr.2017.02.004.

100. Penner-Hahn JE. Characterization of “spectroscopically quiet” metals in biology. Coordination Chemistry Reviews. 2005;249(1):161-77. 10.1016/j.ccr.2004.03.011.

101. Willmott P. An Introduction to Synchrotron Radiation: Techniques and Applications. 1. Aufl. ed. New York: New York: Wiley; 2011.

102. Howard DL, de Jonge MD, Afshar N, Ryan CG, Kirkham R, Reinhardt J, et al. The XFM beamline at the Australian Synchrotron. Journal of synchrotron radiation. 2020;27(5):1447-58. 10.1107/S1600577520010152.

103. Hackett M, Paterson P, Pickering I, George G. Imaging Taurine in the Central Nervous System Using Chemically Specific X-ray Fluorescence Imaging at the Sulfur K-Edge. Analytical Chemistry 2016;18(22):10916-24. 10.1021/acs.analchem.6b02298.

104. Kopittke PM, Jonge MD, Wang P, McKenna BA, Lombi E, Paterson DJ, et al. Laterally resolved speciation of arsenic in roots of wheat and rice using fluorescence-XANES imaging. New Phytol. 2014;201(4):1251-62. 10.1111/nph.12595.

105. Wang P, Menzies NW, Lombi E, McKenna BA, James S, Tang C, et al. Synchrotron-based X-ray absorption near-edge spectroscopy imaging for laterally resolved speciation of selenium

in fresh roots and leaves of wheat and rice. J Exp Bot. 2015;66(15):4795-806. 10.1093/jxb/erv254.

106. Hare DJ, New EJ, de Jonge MD, McColl G. Imaging metals in biology: balancing sensitivity, selectivity and spatial resolution. Chem Soc Rev. 2015;44(17):5941-58. 10.1039/c5cs00055f.

107. Joppe K, Nicolas J-D, Grünewald TA, Eckermann M, Salditt T, Lingor P. Elemental quantification and analysis of structural abnormalities in neurons from Parkinson's-diseased brains by X-ray fluorescence microscopy and diffraction. Biomedical optics express. 2020;11(7):3423-43. 10.1364/BOE.389408.

108. Wang H-J, Wang M, Wang B, Meng X-Y, Wang Y, Li M, et al. Quantitative imaging of element spatial distribution in the brain section of a mouse model of Alzheimer's disease using synchrotron radiation X-ray fluorescence analysis. Journal of analytical atomic spectrometry. 2010;25(3):328-33. 10.1039/b921201a.

109. Leskovjan AC, Kretlow A, Lanzirotti A, Barrea R, Vogt S, Miller LM. Increased brain iron coincides with early plaque formation in a mouse model of Alzheimer's disease. Neuroimage. 2011;55(1):32-8. 10.1016/j.neuroimage.2010.11.073.

110. Caine S, Hackett M, Hou H, Kumar S, Maley J, Ivanishvili Z, et al. A novel multi-modal platform to image molecular and elemental alterations in ischemic stroke. 2016.

111. Hackett MJ, Desouza M, Caine S, Bewer B, Nichol H, Paterson PG, et al. A new method to image heme-Fe, total Fe, and aggregated protein levels after intracerebral hemorrhage. ACS Chem Neurosci. 2015;6(5):761-70. 10.1021/acschemneuro.5b00037.

112. Pushie MJ, Sylvain NJ, Hou H, Caine S, Hackett MJ, Kelly ME. Tracking elemental changes in an ischemic stroke model with X-ray fluorescence imaging. Sci Rep. 2020;10(1):17868-. 10.1038/s41598-020-74698-2.

113. Hackett M, Aitken J, El-Assaad F, McQuillan J, Carter E, Ball H, et al. Mechanisms of murine cerebral malaria: Multimodal imaging of altered cerebral metabolism and protein oxidation at hemorrhage sites. 2015.

114. Chwiej J, Winiarski W, Ciarach M, Janeczko K, Lankosz M, Rickers K, et al. The role of trace elements in the pathogenesis and progress of pilocarpine-induced epileptic seizures. J Biol Inorg Chem. 2008;13(8):1267-74. 10.1007/s00775-008-0411-6.

115. Lins B, Pushie J, Jones M, Howard D, Howland J, Hackett M. Mapping alterations to the endogenous elemental distribution within the lateral ventricles and choroid plexus in brain disorders using X-ray fluorescence imaging. 2016.

116. Mikhaylova A, Davidson M, Toastmann H, Channell JET, Guyodo Y, Batich C, et al. Detection, identification and mapping of iron anomalies in brain tissue using X-ray absorption spectroscopy. J R Soc Interface. 2005;2(2):33-7. 10.1098/rsif.2004.0011.

117. Hackett MJ, Smith SE, Paterson PG, Nichol H, Pickering IJ, George GN. X-ray Absorption Spectroscopy at the Sulfur K-Edge: A New Tool to Investigate the Biochemical Mechanisms of Neurodegeneration. ACS Chemical Neuroscience. 2012;3(3):178-85.

118. James SA, Roberts BR, Hare DJ, de Jonge MD, Birchall IE, Jenkins NL, et al. Direct in vivo imaging of ferrous iron dyshomeostasis in ageing Caenorhabditis elegans. Chemical Science. 2015;6(5):2952-62. 10.1039/C5SC00233H.

119. James SA, Hare DJ, Jenkins NL, de Jonge MD, Bush AI, McColl G. ϕXANES: In vivo imaging of metal-protein coordination environments. Scientific Reports. 2016;6:20350. 10.1038/srep20350.

120. Wilson SA, Green E, Mathews II, Benfatto M, Hodgson KO, Hedman B, et al. X-ray absorption spectroscopic investigation of the electronic structure differences in solution and crystalline oxyhemoglobin. Proceedings of the National Academy of Sciences of the United States of America. 2013;110(41):16333-8. 10.1073/pnas.1315734110.

121. Everett J, Collingwood JF, Tjendana-Tjhin V, Brooks J, Lermyte F, Plascencia-Villa G, et al. Nanoscale synchrotron X-ray speciation of iron and calcium compounds in amyloid plaque cores from Alzheimer's disease subjects. Nanoscale. 2018;10(25):11782-96. 10.1039/C7NR06794A.

122. Wang H, Wang M, Wang B, Li M, Chen H, Yu X, et al. The distribution profile and oxidation states of biometals in APP transgenic mouse brain: dyshomeostasis with age and as a function of the development of Alzheimer's disease. Metallomics. 2012;4(3):289-96. 10.1039/C2MT00104G.

123. Gunter KK, Miller LM, Aschner M, Eliseev R, Depuis D, Gavin CE, et al. XANES Spectroscopy: A Promising Tool for Toxicology:: A Tutorial. NeuroToxicology. 2002;23(2):127-46. 10.1016/S0161-813X(02)00034-7.

124. Ceko MJ, Aitken JB, Harris HH. Speciation of copper in a range of food types by X-ray absorption spectroscopy. Food Chemistry. 2014;164:50-4. 10.1016/j.foodchem.2014.05.018.

125. Sullivan B, Robison G, Osborn J, Kay M, Thompson P, Davis K, et al. On the nature of the Cu-rich aggregates in brain astrocytes. Redox Biology. 2017;11:231-9. 10.1016/j.redox.2016.12.007.

126. James SA, Burke R, Howard DL, Spiers KM, Paterson DJ, Murphy S, et al. Visualising coordination chemistry: fluorescence X-ray absorption near edge structure tomography. Chem Commun. 2016;52(79):11834-7. 10.1039/c6cc06747f.

127. Hackett MJ, Smith SE, Caine S, Nichol H, George GN, Pickering IJ, et al. Novel bio-spectroscopic imaging reveals disturbed protein homeostasis and thiol redox with protein aggregation prior to hippocampal CA1 pyramidal neuron death induced by global brain ischemia in the rat. Free Radic Biol Med. 2015;89(C):806-18. 10.1016/j.freeradbiomed.2015.08.029.

128. Smith PG, Koch I, Gordon RA, Mandoli DF, Chapman BD, Reimer KJ. X-ray absorption near-edge structure analysis of arsenic species for application to biological environmental simples. Environmental Science and Technology. 2005;39(1):248-54. 10.1021/es049358b.

129. Weekley CM, Shanu A, Aitken JB, Vogt S, Witting PK, Harris HH. XAS and XFM studies of selenium and copper speciation and distribution in the kidneys of selenite-supplemented rats. Metallomics. 2014;6(9):1602-15. 10.1039/c4mt00088a.

130. Weekley C, Aitken J, Finney L, Vogt S, Witting P, Harris H. Selenium Metabolism in Cancer Cells: The Combined Application of XAS and XFM Techniques to the Problem of Selenium Speciation in Biological Systems. Nutrients. 2013;5(5):1734-56. 10.3390/nu5051734.

131. Pickering IJ, Wright C, Bubner B, Ellis D, Persans MW, Eileen YY, et al. Chemical form and distribution of selenium and sulfur in the selenium hyperaccumulator Astragalus bisulcatus. Plant physiology. 2003;131(3):1460-7.

132. Thavarajah D, Vandenberg A, George GN, Pickering IJ. Chemical form of selenium in naturally selenium-rich lentils (Lens culinaris L.) from Saskatchewan. Journal of agricultural and food chemistry. 2007;55(18):7337-41.

133. Telling ND, Everett J, Collingwood JF, Dobson J, van der Laan G, Gallagher JJ, et al. Iron Biochemistry is Correlated with Amyloid Plaque Morphology in an Established Mouse Model of Alzheimer's Disease. Cell Chemical Biology. 2017;24(10):1205-15.e3. 10.1016/j.chembiol.2017.07.014.

134. Thomas SA, Mishra B, Myneni SCB. High Energy Resolution-X-ray Absorption Near Edge Structure Spectroscopy Reveals Zn Ligation in Whole Cell Bacteria. Journal of Physical Chemistry Letters. 2019;10(10):2585-92. 10.1021/acs.jpclett.9b01186.

135. Wandzilak A, Czyzycki M, Wrobel P, Szczerbowska-Boruchowska M, Radwanska E, Adamek D, et al. The oxidation states and chemical environments of iron and zinc as potential indicators of brain tumour malignancy grade - preliminary results. Metallomics. 2013;5(11):1547-53. 10.1039/c3mt00158j.

136. Kopittke PM, Menzies NW, de Jonge MD, McKenna BA, Donner E, Webb RI, et al. In situ distribution and speciation of toxic copper, nickel, and zinc in hydrated roots of cowpea. Plant Physiology. 2011;156(2):663-73.

137. Wang P, Menzies NW, Lombi E, McKenna BA, Johannessen B, Glover CJ, et al. Fate of ZnO nanoparticles in soils and cowpea (Vigna unguiculata). Environmental Science & Technology. 2013;47(23):13822-30.

138. Salt DE, Prince RC, Baker AJM, Raskin I, Pickering IJ. Zinc Ligands in the Metal Hyperaccumulator Thlaspi caerulescens As Determined Using X-ray Absorption Spectroscopy. Environmental Science & Technology. 1999;33(5):713-7. 10.1021/es980825x.

139. Abbehausen C, de Paiva REF, Bjornsson R, Gomes SQ, Du Z, Corbi PP, et al. X-ray Absorption Spectroscopy Combined with Time-Dependent Density Functional Theory

Elucidates Differential Substitution Pathways of Au(I) and Au(III) with Zinc Fingers. Inorganic Chemistry. 2018;57(1):218-30. 10.1021/acs.inorgchem.7b02406.

140. de Arruda EGR, Rocha BA, Barrionuevo MVF, Aðalsteinsson HM, Galdino FE, Loh W, et al. The influence of ZnII coordination sphere and chemical structure over the reactivity of metallo-β-lactamase model compounds. Dalton Transactions. 2019;48(9):2900-16. 10.1039/C8DT03905D.

141. McCubbin Stepanic O, Ward J, Penner-Hahn JE, Deb A, Bergmann U, DeBeer S. Probing a Silent Metal: A Combined X-ray Absorption and Emission Spectroscopic Study of Biologically Relevant Zinc Complexes. Inorganic Chemistry. 2020;59(18):13551-60. 10.1021/acs.inorgchem.0c01931.

142. Bishop DP, Cole N, Zhang T, Doble PA, Hare DJ. A guide to integrating immunohistochemistry and chemical imaging. Chem Soc Rev. 2018;47(11):3770-87. 10.1039/c7cs00610a.

143. Bumbrah GS, Sharma RM. Raman spectroscopy – Basic principle, instrumentation and selected applications for the characterization of drugs of abuse. Egyptian journal of forensic sciences. 2016;6(3):209-15. 10.1016/j.ejfs.2015.06.001.

144. Surmacki JM, Ansel-Bollepalli L, Pischiutta F, Zanier ER, Ercole A, Bohndiek SE. Label-free monitoring of tissue biochemistry following traumatic brain injury using Raman spectroscopy. Analyst. 2016;142(1):132-9. 10.1039/c6an02238c.

145. Khalenkow D, Donche S, Braeckman K, Vanhove C, Skirtach AG. Added Value of Microscale Raman Chemical Analysis in Mild Traumatic Brain Injury (TBI): A Comparison with Macroscale MRI. ACS Omega. 2018;3(12):16806-11. 10.1021/acsomega.8b02404.

146. Lochocki B, Boon BDC, Verheul SR, Zada L, Hoozemans JJM, Ariese F, et al. Multimodal, label-free fluorescence and Raman imaging of amyloid deposits in snap-frozen Alzheimer's disease human brain tissue. Commun Biol. 2021;4(1):474-. 10.1038/s42003-021-01981-x.

147. Kiskis J, Fink H, Nyberg L, Thyr J, Li J-Y, Enejder A. Plaque-associated lipids in Alzheimer's diseased brain tissue visualized by nonlinear microscopy. Sci Rep. 2015;5(1):13489-. 10.1038/srep13489.

148. Dong J, Atwood CS, Anderson VE, Siedlak SL, Smith MA, Perry G, et al. Metal Binding and Oxidation of Amyloid-β within Isolated Senile Plaque Cores: Raman Microscopic Evidence. Biochemistry. 2003;42(10):2768-73. 10.1021/bi0272151.

149. Ji M, Arbel M, Zhang L, Freudiger CW, Hou SS, Lin D, et al. Label-free imaging of amyloid plaques in Alzheimer's disease with stimulated raman scattering microscopy. Sci Adv. 2018;4(11):eaat7715-eaat. 10.1126/sciadv.aat7715.

150. Koljenović S, Choo-Smith L-Pi, Schut TCB, Kros JM, Van den Berge HJ, Puppels GJ. Discriminating Vital Tumor from Necrotic Tissue in Human Glioblastoma Tissue Samples by Raman Spectroscopy. Lab Invest. 2002;82(10):1265-77. 10.1097/01.LAB.0000032545.96931.B8.

151. Rakib F, Al-Saad K, Ahmed T, Ullah E, Barreto GE, Md Ashraf G, et al. Biomolecular alterations in acute traumatic brain injury (TBI) using Fourier transform infrared (FTIR) imaging spectroscopy. Spectrochimica acta Part A, Molecular and biomolecular spectroscopy. 2021;248. 10.1016/j.saa.2020.119189.

152. Ali MHM, Rakib F, Abdelalim EM, Limbeck A, Mall R, Ullah E, et al. Fourier-transform infrared imaging spectroscopy and laser ablation -ICPMS new vistas for biochemical analyses of ischemic stroke in rat brain. Front Neurosci. 2018;12:647-. 10.3389/fnins.2018.00647.

153. Dieing T. Confocal Raman Microscopy / edited by Thomas Dieing, Olaf Hollricher, Jan Toporski. Hollricher O, Toporski J, SpringerLink, editors. Berlin, Heidelberg: Berlin, Heidelberg : Springer Berlin Heidelberg; 2011.

154. Vongsvivut J, Pérez-Guaita D, Wood BR, Heraud P, Khambatta K, Hartnell D, et al. Synchrotron macro ATR-FTIR microspectroscopy for high-resolution chemical mapping of single cells. Analyst. 2019;144(1):3226-38. 10.1039/c8an01543k.

155. Hartnell D, Hollings A, Ranieri AM, Lamichhane HB, Becker T, Sylvain NJ, et al. Mapping sub-cellular protein aggregates and lipid inclusions using synchrotron ATR-FTIR microspectroscopy. Analyst. 2021;146(11):3516-25. 10.1039/d1an00136a.

156. Miller LM, Dumas P. Chemical imaging of biological tissue with synchrotron infrared light. BIOCHIMICA ET BIOPHYSICA ACTA-BIOMEMBRANES. 2006;1758(7):846-57. 10.1016/j.bbamem.2006.04.010.

157. Storch WBa. Immunofluorescence in Clinical Immunology : A Primer and Atlas / by Wulf B. Storch. SpringerLink, editor: Basel : BirkhÃ¤user Basel : Imprint: BirkhÃ¤user; 2000.

158. Papachristodoulou DKa. Biochemistry and molecular biology / Despo Papachristodoulou, Alison Snape, William H. Elliott, and Daphne C. Elliott. Sixth edition.. ed. Snape Aa, Elliott WHa, Elliott DCa, editors: Oxford : Oxford University Press; 2018.

159. Bryda EC. The Mighty Mouse: the impact of rodents on advances in biomedical research. Mo Med. 2013;110(3):207-11.

160. Elder GA, Gama Sosa MA, De Gasperi R. Transgenic Mouse Models of Alzheimer's Disease. The Mount Sinai journal of medicine. 2010;77(1):69-81. 10.1002/msj.20159.

161. Bilkei-Gorzo A. Genetic mouse models of brain ageing and Alzheimer's disease. Pharmacol Ther. 2014;142(2):244-57. 10.1016/j.pharmthera.2013.12.009.

162. Sturchler-Pierrat C, Staufenbiel M. Pathogenic Mechanisms of Alzheimer's Disease Analyzed in the APP23 Transgenic Mouse Model. Ann N Y Acad Sci. 2000;920(1):134-9. 10.1111/j.1749-6632.2000.tb06915.x.

163. Takeda T, Hosokawa M, Higuchi K. Senescence-accelerated mouse (SAM): A novel murine model of senescence. Experimental Gerontology. 1997;32(1):105-9. 10.1016/S0531-5565(96)00036-8.

164. Butterfield DA, Poon HF. The senescence-accelerated prone mouse (SAMP8): A model of age-related cognitive decline with relevance to alterations of the gene expression and protein abnormalities in Alzheimer's disease. Experimental Gerontology. 2005;40(10):774-83. 10.1016/j.exger.2005.05.007.

165. Flood JF, E. Morley J. Learning and memory in the SAMP8 mouse. Neuroscience and biobehavioral reviews. 1997;22(1):1-20. 10.1016/S0149-7634(96)00063-2.

166. Morley JE, Armbrecht HJ, Farr SA, Kumar VB. The senescence accelerated mouse (SAMP8) as a model for oxidative stress and Alzheimer's disease. BBA - Molecular Basis of Disease. 2012;1822(5):650-6. 10.1016/j.bbadis.2011.11.015.

167. Pelegrí C, Canudas AM, del Valle J, Casadesus G, Smith MA, Camins A, et al. Increased permeability of blood–brain barrier on the hippocampus of a murine model of senescence. Mech Ageing Dev. 2007;128(9):522-8. 10.1016/j.mad.2007.07.002.

168. Valle J, Duran-Vilaregut J, Manich G, Camins A, Pallàs M, Vilaplana J, et al. Time-course of blood–brain barrier disruption in senescence-accelerated mouse prone 8 (SAMP8) mice. Int J Dev Neurosci. 2009;27(1):47-52. 10.1016/j.ijdevneu.2008.10.002.

169. Hollings AL, Lam V, Takechi R, Mamo JCL, Reinhardt J, de Jonge MD, et al. Revealing differences in the chemical form of zinc in brain tissue using K-edge X-ray absorption near-edge structure spectroscopy. Metallomics. 2020;12(12):2134-44. 10.1039/d0mt00198h.

170. Pushie MJ, Hollings A, Reinhardt J, Webb SM, Lam V, Takechi R, et al. Sample preparation with sucrose cryoprotection dramatically alters Zn distribution in the rodent hippocampus, as revealed by elemental mapping. J Anal At Spectrom. 2020;35(11):2498-258. 10.1039/d0ja00323a.

171. Hackett MJ, Britz CJ, Nichol H, Paterson PG, Pickering IJ, George GN. In situ Bio-Spectroscopic Investigation of Rapid Ischemic and Post-mortem Induced Biochemical Alterations in the Rat Brain. ACS Chemical Neuroscience. 2015;6:226-38.

172. Hackett MJ, McQuillan JA, El-Assaad F, Aitken JB, Levina A, Cohen DD, et al. Chemical alterations to murine brain tissue induced by formalin fixation: Implications for biospectroscopic imaging and mapping studies of disease pathogenesis. Analyst. 2011;136(14):2941-52. 10.1039/c0an00269k.

173. Kappen P, Ruben G. A tool for pre-processing multi-element fluorescence data [Available from: https://www.ansto.gov.au/user-access/instruments/australian-synchrotron-beamlines/x-ray-absorption-spectroscopy/sakura.

174. George GN, Pickering IJ. EXAFSPAK: A suite of computer programs for analysis of X-ray absorption spectra. http://ssrlslacstanfordedu/exafspakhtml. 1995.

175. Paterson D, De Jonge M, Howard D, Lewis W, McKinlay J, Starritt A, et al. The X-ray Fluorescence Microscopy Beamline at the Australian Synchrotron. AIP Conference Proceedings. 2011;1365(1):219-22.

176. Hackett MJ, Hollings A, Caine S, Bewer BE, Alaverdashvili M, Takechi R, et al. Elemental characterisation of the pyramidal neuron layer within the rat and mouse hippocampus. Metallomics. 2019;11:151-65. 10.1039/C8MT00230D.

177. Hartnell D, Gillespie-Jones K, Ciornei C, Hollings A, Thomas A, Harrild E, et al. Characterization of Ionic and Lipid Gradients within Corpus Callosum White Matter after Diffuse Traumatic Brain Injury in the Rat. ACS Chemical Neuroscience. 2019;11(3):248-57.

178. Ryan CG, Siddons DP, Kirkham R, Li ZY, De Jonge MD, Paterson DJ, et al. Maia X-ray fluorescence imaging: Capturing detail in complex natural samples. Journal of Physics: Conference Series. 2014;499(1):12002-12. 10.1088/1742-6596/499/1/012002.

179. Adlard PA, Parncutt J, Lal V, James S, Hare D, Doble P, et al. Metal chaperones prevent zinc-mediated cognitive decline. Neurobiol Dis. 2014;81:196-202. 10.1016/j.nbd.2014.12.012.

180. Adlard PA, Parncutt JM, Finkelstein DI, Bush AI. Cognitive loss in zinc transporter-3 knock-out mice: a phenocopy for the synaptic and memory deficits of Alzheimer's disease? The Journal of neuroscience : the official journal of the Society for Neuroscience. 2010;30(5):1631. 10.1523/JNEUROSCI.5255-09.2010.

181. Takeda A, Takefuta S, Okada S, Oku N. Relationship between brain zinc and transient learning impairment of adult rats fed zinc-deficient diet. Brain Res. 2000;859(2):352-7. 10.1016/S0006-8993(00)02027-8.

182. Clark-Baldwin K, Tierney DL, Govindaswamy N, Gruff ES, Kim C, Berg J, et al. The limitations of X-ray absorption spectroscopy for determining the structure of zinc sites in proteins. When is a tetrathiolate not a tetrathiolate? Journal of the American Chemical Society. 1998;120(33):8401-9. 10.1021/ja980580o.

183. Yamamoto T. Assignment of pre-edge peaks in K-edge x-ray absorption spectra of 3d transition metal compounds: electric dipole or quadrupole? X-ray spectrometry. 2008;37(6):572-84. 10.1002/xrs.1103.

184. Krężel A, Maret W. The biological inorganic chemistry of zinc ions. Archives of Biochemistry and Biophysics. 2016;611:3-19. 10.1016/j.abb.2016.04.010.

185. Hallman PS, Perrin DD, Watt AE. The computed distribution of copper(II) and zinc(II) ions among seventeen amino acids present in human blood plasma. Biochemical Journal. 1971;121(3):549-55. 10.1042/bj1210549.

186. Dudev T, Lim C. Tetrahedral vs octahedral zinc complexes with ligands of biological interest: a DFT/CDM study. Journal of the American Chemical Society. 2000;122(45):11146-53.

187. Vallee BL, Auld DS. Zinc coordination, function, and structure of zinc enzymes and other proteins. Biochemistry. 1990;29(24):5647-59.

188. Toussaint L, Cuypers M, Bertrand L, Hue L, Romao C, Saraiva L, et al. Comparative Fe and Zn K-edge X-ray absorption spectroscopic study of the ferroxidase centres of human H-chain ferritin and bacterioferritin from Desulfovibrio desulfuricans. JBIC Journal of Biological Inorganic Chemistry. 2009;14(1):35-49.

189. Nienaber KH, Pushie MJ, Cotelesage JJH, Pickering IJ, George GN. Cryoprotectants Severely Exacerbate X-ray-Induced Photoreduction. J Phys Chem Lett. 2018;9(3):540-4. 10.1021/acs.jpclett.7b03111.

190. Pickering IJ, Prince RC, Divers T, George GN. Sulfur K-edge X-ray absorption spectroscopy for determining the chemical speciation of sulfur in biological systems. FEBS Lett. 1998;441(1):11-4. 10.1016/S0014-5793(98)01402-1.

191. Kassim R, Ramseyer C, Enescu M. Oxidation of zinc-thiolate complexes of biological interest by hydrogen peroxide: a theoretical study. Inorganic chemistry. 2011;50(12):5407. 10.1021/ic200267x.

192. Zhu G, Koszelak-Rosenblum M, Connelly SM, Dumont ME, Malkowski MG. The Crystal Structure of an Integral Membrane Fatty Acid α-Hydroxylase. J Biol Chem. 2015;290(50):29820-33. 10.1074/jbc.M115.680124.

193. Maret W, Li Y. Coordination dynamics of zinc in proteins. Chemical reviews. 2009;109(10):4682-707.

194. Kim GH, Kim JE, Rhie SJ, Yoon S. The Role of Oxidative Stress in Neurodegenerative Diseases. Exp Neurobiol. 2015;24(4):325-40. 10.5607/en.2015.24.4.325.

195. Markesbery WR. Oxidative Stress Hypothesis in Alzheimer's Disease. Free Radic Biol Med. 1997;23(1):134-47. 10.1016/S0891-5849(96)00629-6.

196. Belaidi AA, Bush AI. Iron neurochemistry in Alzheimer's disease and Parkinson's disease: targets for therapeutics. J Neurochem. 2016;139(S1):179-97. 10.1111/jnc.13425.

197. Fu S, Jiang W, Zheng W. Age-dependent increase of brain copper levels and expressions of copper regulatory proteins in the subventricular zone and choroid plexus. Front Mol Neurosci. 2015;8:22-. 10.3389/fnmol.2015.00022.

198. Maynard CJ, Cappai R, Volitakis I, Cherny RA, White AR, Beyreuther K, et al. Overexpression of Alzheimer's disease amyloid-β opposes the age-dependent elevations of brain copper and iron. J Biol Chem. 2002;277(47):44670-6. 10.1074/jbc.M204379200.

199. Nolte J. Essentials of the human brain / John Nolte. First Edition / Electronic version.. ed: Philadelphia Mosby/Elsevier; 2010.

200. Pushie MJ, Pickering IJ, Martin GR, Tsutsui S, Jirik FR, George GN. Prion protein expression level alters regional copper, iron and zinc content in the mouse brain. Metallomics. 2011;3(2):206-14. 10.1039/c0mt00037j.

201. Ashraf A, Michaelides C, Walker TA, Ekonomou A, Suessmilch M, Sriskanthanathan A, et al. Regional Distributions of Iron, Copper and Zinc and Their Relationships With Glia in a Normal Aging Mouse Model. Front Aging Neurosci. 2019;11:351-. 10.3389/fnagi.2019.00351.

202. Butterfield DA, Howard BJ, Yatin S, Allen KL, Carney JM. Free Radical Oxidation of Brain Proteins in Accelerated Senescence and its Modulation by N-tert-butyl-α -phenylnitrone. Proc Natl Acad Sci U S A. 1997;94(2):674-8. 10.1073/pnas.94.2.674.

203. Poon HF, Castegna A, Farr SA, Thongboonkerd V, Lynn BC, Banks WA, et al. Quantitative proteomics analysis of specific protein expression and oxidative modification in aged senescence-accelerated-prone 8 mice brain. Neuroscience. 2004;126(4):915-26. 10.1016/j.neuroscience.2004.04.046.

204. Baba SP, Bhatnagar A. Role of thiols in oxidative stress. Current opinion in toxicology. 2018;7:133-9. 10.1016/j.cotox.2018.03.005.

205. George GN, Pickering IJ, Cotelesage JJH, Vogt LI, Dolgova NV, Regnier N, et al. Visualizing sulfur with X-rays: From molecules to tissues. Phosphorus, sulfur, and silicon and the related elements. 2019;194(7):618-23. 10.1080/10426507.2019.1602618.

206. Barrera G, Pizzimenti S, Daga M, Dianzani C, Arcaro A, Cetrangolo GP, et al. Lipid peroxidation-derived aldehydes, 4-hydroxynonenal and malondialdehyde in aging-related disorders. Antioxidants (Basel). 2018;7(8):102. 10.3390/antiox7080102.

207. Squier TC. Oxidative stress and protein aggregation during biological aging. Exp Gerontol. 2001;36(9):1539-50. 10.1016/S0531-5565(01)00139-5.

208. Gafni A. Structural Modifications of Proteins During Aging. J Am Geriatr Soc. 1997;45(7):871-80. 10.1111/j.1532-5415.1997.tb01518.x.

209. Furber KL, Lacombe RJS, Caine S, Thangaraj MP, Read S, Rosendahl SM, et al. Biochemical Alterations in White Matter Tracts of the Aging Mouse Brain Revealed by FTIR Spectroscopy Imaging. Neurochem Res. 2021;47(3):795-810. 10.1007/s11064-021-03491-y.

210. Sato M, Bremner I. Oxygen free radicals and metallothionein. Free Radical Biology and Medicine. 1993;14(3):325-37. 10.1016/0891-5849(93)90029-T.

211. Hussain S, Slikker W, Ali SF. ROLE OF METALLOTHIONEIN AND OTHER ANTIOXIDANTS IN SCAVENGING SUPEROXIDE RADICALS AND THEIR POSSIBLE ROLE IN NEUROPROTECTION **This is one of original manuscripts on the subject of “antioxidants” related to a workshop organized by Dr Joe Marwah, which took place on Hollywood, Florida, U.S.A. on 12 November 1994. Dr J. Marwah (National Institutes of Health) and Dr M. Ebadi (University of Nebraska Medical School) acted as executive editors in the refereeing of these articles. Neurochemistry International. 1996;29(2):145-52. 10.1016/0197-0186(95)00114-X.

212. Shim S-Y, Kim H-S. Oxidative stress and the antioxidant enzyme system in the developing brain. Korean Journal of Pediatrics. 2013;56(3):107-11. 10.3345/kjp.2013.56.3.107.

213. Baker ZN, Cobine PA, Leary SC. The mitochondrion: a central architect of copper homeostasis. Metallomics. 2017;9(11):151-1512. 10.1039/c7mt00221a.

214. Cobine PA, Pierrel F, Winge DR. Copper trafficking to the mitochondrion and assembly of copper metalloenzymes. Biochimica et biophysica acta Molecular cell research. 2006;1763(7):759-72. 10.1016/j.bbamcr.2006.03.002.

215. Cobine PA, Ojeda LD, Rigby KM, Winge DR. Yeast Contain a Non-proteinaceous Pool of Copper in the Mitochondrial Matrix. J Biol Chem. 2004;279(14):14447-55. 10.1074/jbc.M312693200.

216. Chwiej J, Szczerbowska-Boruchowska M, Lankosz M, Wojcik S, Falkenberg G, Stegowski Z, et al. Preparation of tissue samples for X-ray fluorescence microscopy. Spectrochimica acta Part B: Atomic spectroscopy. 2005;60(12):1531-7. 10.1016/j.sab.2005.10.002.

217. Krafft C, Knetschke T, Funk RHW, Salzer R. Studies on Stress-Induced Changes at the Subcellular Level by Raman Microspectroscopic Mapping. Anal Chem. 2006;78(13):4424-9. 10.1021/ac060205b.

218. Schulze HG, Konorov SO, Piret JM, Blades MW, Turner RFB. Label-free imaging of mammalian cell nucleoli by Raman microspectroscopy. Analyst. 2013;138(12):3416-23. 10.1039/c3an00118k.

219. Adar F, Erecinska M, University of P. Resonance Raman spectra of whole mitochondria. Biochemistry. 1978;17(25):5484-8. 10.1021/bi00618a024.

220. Lei Z, Patrick S, Linda H, Changan XIE, Yong-Qing LI. STUDY OF BRAIN CELLS BY NEAR-INFRARED RAMAN SPECTROSCOPY. Journal of the North Carolina Academy of Science. 2005;121(1):41-4.

221. Hsu C-C, Xu J, Brinkhof B, Wang H, Cui Z, Huang WE, et al. A single-cell Raman-based platform to identify developmental stages of human pluripotent stem cell-derived neurons. Proceedings of the National Academy of Sciences - PNAS. 2020;117(31):18412-23. 10.1073/pnas.2001906117.

222. Butler HJ, Ashton L, Bird B, Cinque G, Curtis K, Dorney J, et al. Using Raman spectroscopy to characterize biological materials. Nature protocols. 2016;11(4):664-87.

223. Hamada K, Fujita K, Smith NI, Kobayashi M, Inouye Y, Kawata S. Raman microscopy for dynamic molecular imaging of living cells. J Biomed Opt. 2008;13(4):044027-4. 10.1117/1.2952192.

224. Kann B, Offerhaus HL, Windbergs M, Otto C. Raman microscopy for cellular investigations — From single cell imaging to drug carrier uptake visualization. Adv Drug Deliv Rev. 2015;89:71-90. 10.1016/j.addr.2015.02.006.

225. Chung YG, Schwartz JA, Gardner CM, Sawaya RE, Jacques SL. Diagnostic potential of laser-induced autofluorescence emission in brain tissue. J Korean Med Sci. 1997;12(2):135-42. 10.3346/jkms.1997.12.2.135.

226. Saraswathy A, Jayasree RS, Baiju KV, Gupta AK, Pillai VPM. Optimum wavelength for the differentiation of brain tumor tissue using autofluorescence spectroscopy. Photomed Laser Surg. 2009;27(3):425-33. 10.1089/pho.2008.2316.

227. Croce AC, Bottiroli G. Autofluorescence spectroscopy and imaging: A tool for biomedical research and diagnosis. Eur J Histochem. 2014;58(4):320-37. 10.4081/ejh.2014.2461.

228. Mycek M-A, Pogue BW. Handbook of Biomedical Fluorescence. 1 ed. New York: New York: CRC Press; 2003.

229. Davis AS, Richter A, Becker S, Moyer JE, Sandouk A, Skinner J, et al. Characterizing and Diminishing Autofluorescence in Formalin-fixed Paraffin-embedded Human Respiratory Tissue. J Histochem Cytochem. 2014;62(6):405-23. 10.1369/0022155414531549.

230. Moreno-García A, Kun A, Calero O, Medina M, Calero M. An Overview of the Role of Lipofuscin in Age-Related Neurodegeneration. Front Neurosci. 2018;12:464-. 10.3389/fnins.2018.00464.

231. Sun Y, Chakrabartty A. Cost-effective elimination of lipofuscin fluorescence from formalin-fixed brain tissue by white phosphor light emitting diode array. Biochem Cell Biol. 2016;94(6):545-50. 10.1139/bcb-2016-0125.

232. Schnell SA, Staines WA, Wessendorf MW. Reduction of lipofuscin-like autofluorescence in fluorescently labeled tissue. Journal of Histochemistry & Cytochemistry. 1999;47(6):719-30.

233. Brunk UT, Terman A. Lipofuscin: mechanisms of age-related accumulation and influence on cell function121Guest Editor: Rajindar S. Sohal2This article is part of a series of reviews on “Oxidative Stress and Aging.” The full list of papers may be found on the homepage of the journal. Free Radical Biology and Medicine. 2002;33(5):611-9. 10.1016/S0891-5849(02)00959-0.

234. Grune T, Jung T, Merker K, Davies KJA. Decreased proteolysis caused by protein aggregates, inclusion bodies, plaques, lipofuscin, ceroid, and ‘aggresomes’ during oxidative stress, aging, and disease. The International Journal of Biochemistry & Cell Biology. 2004;36(12):2519-30. 10.1016/j.biocel.2004.04.020.

235. Jolly R, Douglas B, Davey P, Roiri J. Lipofuscin in bovine muscle and brain: a model for studying age pigment. Gerontology. 1995;41(Suppl. 2):283-96.

236. Keller JN, Dimayuga E, Chen Q, Thorpe J, Gee J, Ding Q. Autophagy, proteasomes, lipofuscin, and oxidative stress in the aging brain. The International Journal of Biochemistry & Cell Biology. 2004;36(12):2376-91. 10.1016/j.biocel.2004.05.003.

237. Zhao L, Spassieva SD, Jucius TJ, Shultz LD, Shick HE, Macklin WB, et al. A deficiency of ceramide biosynthesis causes cerebellar purkinje cell neurodegeneration and lipofuscin accumulation. PLoS genetics. 2011;7(5):e1002063.

238. Rogers J, Silver MA, Shoemaker WJ, Bloom FE. Senescent changes in a neurobiological model system: cerebellar Purkinje cell electrophysiology and correlative anatomy. Neurobiology of aging. 1980;1(1):3-11.

239. Takeda T. Senescence-accelerated mouse (SAM) with special references to neurodegeneration models, SAMP8 and SAMP10 mice. Neurochemical research. 2009;34(4):639-59.

240. Marzban H. Development of the Cerebellum from Molecular Aspects to Diseases. Cham: Cham: Springer International Publishing AG; 2017.

241. Farhane Z, Bonnier F, Casey A, Maguire A, O'Neill L, Byrne HJ. Cellular discrimination using in vitro Raman micro spectroscopy: the role of the nucleolus. Analyst. 2015;140(17):5908-19. 10.1039/c5an01157d.

242. Freudiger CW, Min W, Saar BG, Lu S, Holtom GR, He C, et al. Label-free biomedical imaging with high sensitivity by stimulated Raman scattering microscopy. Science. 2008;322(5909):1857-61.

243. Freudiger CW, Pfannl R, Orringer DA, Saar BG, Ji M, Zeng Q, et al. Multicolored stain-free histopathology with coherent Raman imaging. Laboratory investigation. 2012;92(10):1492-502.

244. Fu Y, Huff TB, Wang H-W, Cheng J-X, Wang H. Ex vivo and in vivo imaging of myelin fibers in mouse brain by coherent anti-Stokes Raman scattering microscopy. Optics express. 2008;16(24):19396-409.

245. Klein K, Gigler AM, Aschenbrenner T, Monetti R, Bunk W, Jamitzky F, et al. Label-free live-cell imaging with confocal Raman microscopy. Biophysical journal. 2012;102(2):360-8.

246. Matthaus C, Chernenko T, Newmark JA, Warner CM, Diem M. Label-free detection of mitochondrial distribution in cells by nonresonant Raman microspectroscopy. Biophysical Journal. 2007;93(2):668-73.

247. Palonpon AF, Sodeoka M, Fujita K. Molecular imaging of live cells by Raman microscopy. Current Opinion in Chemical Biology. 2013;17(4):708-15. 10.1016/j.cbpa.2013.05.021.

248. van Manen H-J, Kraan YM, Roos D, Otto C. Single-Cell Raman and Fluorescence Microscopy Reveal the Association of Lipid Bodies with Phagosomes in Leukocytes. Proc Natl Acad Sci U S A. 2005;102(29):10159-64. 10.1073/pnas.0502746102.

249. Lochocki B, Morrema TH, Ariese F, Hoozemans JJ, de Boer JF. The search for a unique Raman signature of amyloid-beta plaques in human brain tissue from Alzheimer's disease patients. Analyst. 2020;145(5):1724-36.

250. Palombo F, Tamagnini F, Jeynes JCG, Mattana S, Swift I, Nallala J, et al. Detection of Aβ plaque-associated astrogliosis in Alzheimer's disease brain by spectroscopic imaging and immunohistochemistry. Analyst. 2018;143(4):850-7. 10.1039/c7an01747b.

251. Schie IW, Huser T. Methods and Applications of Raman Microspectroscopy to Single-Cell Analysis. Appl Spectrosc. 2013;67(8):813-28. 10.1366/12-06971.

252. Hackett MJ, Borondics F, Brown D, Hirschmugl C, Smith SE, Paterson PG, et al. A Sub-Cellular Biochemical Investigation of Purkinje Neurons Using Synchrotron Radiation Fourier Transform Infrared Spectroscopic Imaging with a Focal Plane Array Detector. ACS Chemical Neuroscience 2013;4(7):1071-80.

253. Czamara K, Majzner K, Pacia MZ, Kochan K, Kaczor A, Baranska M. Raman spectroscopy of lipids: a review. J Raman Spectrosc. 1002;46(1):4-20. 10.1002/jrs.4607.

254. Muik B, Lendl B, Molina-Díaz A, Ayora-Cañada MJ. Direct monitoring of lipid oxidation in edible oils by Fourier transform Raman spectroscopy. Chem Phys Lipids. 2005;134(2):173-82. 10.1016/j.chemphyslip.2005.01.003.

255. Ali SM, Bonnier F, Tfayli A, Lambkin HA, Flynn K, McDonagh V, et al. Raman spectroscopic analysis of human skin tissue sections ex-vivo: evaluation of the effects of tissue processing and dewaxing. Journal of biomedical optics. 2012;18(6):061202.

256. Mariani MM, Lampen P, Popp J, Wood BR, Deckert V. Impact of fixation on in vitro cell culture lines monitored with Raman spectroscopy. Analyst. 2009;134(6):1154-61.